The GR3 Method for the Stress Analysis of Weldments

by

Aditya Chattopadhyay

A thesis

presented to the University of Waterloo

in fulfillment of the

thesis requirement for the degree of

Master of Applied Science

in

Mechanical Engineering

Waterloo, Ontario, Canada, 2009

I hereby declare that I am the sole author of this thesis. This is a true copy of the thesis, including any required final revisions, as accepted by my examiners.

I understand that my thesis may be made electronically available to the public.

Signature

Abstract

Determination of the fatigue life of a component requires knowledge of the local maximum fluctuation stress and the through-thickness stress distribution acting at the critical cross-section. This has traditionally been achieved through the use of stress concentration factors. More recently finite element methods have been used to determine the maximum stress acting on a weldment. Unfortunately, meshing large and complicated geometries properly requires the use of fine meshes and can be computationally intensive and time consuming. An alternative method for obtaining maximum stress values using coarse three-dimensional finite element meshes and the hot spot stress concept will be examined in this paper.

Coarse mesh stress distributions were found to coincide with fine mesh stress distributions over the inboard 50% of a cross-section. It was also found that the moment generated by stress distribution over the inboard half of the cross-section accounted for roughly 10% of the total moment acting in all of the cases studied. As a result of this, the total moment acting on a cross-section may be predicted using knowledge of the stress distribution over the inboard 50% of a structure.

Given the moment acting on a cross-section, the hot spot stress may be found. Using bending and membrane stress concentration factors, the maximum stress value may be found. Finally, given the maximum stress data, the fatigue life of a component may be determined using either the strain-life approach or fatigue crack growth methods.

Acknowledgements

I would not have been able to complete this project without the assistance and support of many individuals.

I would like to thank my supervisor Dr. Gregory Glinka, for the advice, guidance, support, and coffee he provided over the course of my degree. I truly appreciate the assistance he provided over the past years, and consider myself very lucky to have had him as a supervisor.

I would like to thank my sister, Bibi Roy, for always being there to talk to. I'd also like to acknowledge my distinguished colleagues, Elena Atroshchenko, Maria El-Zeghayar, and Dr. Sam Mikheevskiy for giving me feedback on my ideas. I couldn't have asked for a better team.

Finally, I'd like to acknowledge Full Throttle energy drinks, without which I would never have managed to stay on schedule.

Dedication

I would like to dedicate this thesis to my parents, Arun Chattopadhyay and Namita Chattopadhyay. I wouldn't be here today if it wasn't for them.

Contents

List of Figures viii
List of Tables xi
Nomenclature xii
1.0 Introduction 1
2.0 Fatigue Analysis 2
2.1 Literature Background 2
2.2 The Strain-Life Method 3
2.3 The Fracture Mechanics Method 5
2.3.1 The Paris Equation 7
2.3.2 Calculation of the Stress Intensity Factor 8
2.3.3 The Crack Shape Model 9
3.0 Stress Concentrations and Distributions in Welded Connections 11
3.1 The Hot Spot Stress Concept 11
3.2 Stress Concentration Factors near Fillet Welds 12
3.2.1 Stress Concentration Factors for a T-Joint Subjected to an Axial Load 15
3.2.2 Stress Concentration Factors for a T-Joint Subjected to a Bending Load 16
3.3 Stress Concentration Factors near Butt Welds 17
3.3.1 Stress Concentration Factors for a butt joint Subjected to an Axial Load 17
3.3.2 Stress Concentration Factors for a butt Joint Subjected to a Bending Load 18
3.4 Simulation of the Stress Distribution in the Weld Toe Cross-Section 19
3.4.1 Monahan's Equation 19
3.4.2 Glinka's Notch Tip Stress Distribution 21
4.0 Coarse Three-Dimensional Mesh Finite Element Model 22
4.1 Procedure for Generating the Coarse 3D Finite Element Mesh 24
4.2 Calculation of the Total Moment from the Finite Element Mesh Data 25
4.3 Calculation of the Total Load from the Finite Element Mesh Data 27
4.4 Validation of the Coarse 3D Finite Element Mesh 28
4.4.1 In-Plane Bending Welded T-Joint Analysis 28
4.4.2 Out-of-Plane Bending Welded T-Joint Analysis 37
4.4.3 Circular Tube on Plate Under Bending 47

4.4.4 Circular Tube on Plate Under Tension 57
5.0 Experimental Verification 69
5.1 Geometries of the two test specimens 69
5.1.1 Notch Geometry 70
5.1.2 Weld Geometry 72
5.2 Material Properties 73
5.3 Loading and Boundary Conditions 74
5.4 Notched Specimen Analysis 75
5.4.1 Notched Specimen GR3 Analysis 75
5.4.2 Notched Specimen Strain Life Analysis 79
5.4.3 Notched Specimen Fatigue Crack Growth Analysis 83
5.4.4 Notched Specimen Total Predicted Lives 88
5.4.5 Comparison of Total and Predicted Lives for the Notched Specimen 88
5.5 Welded Specimen Analysis 89
5.5.1 Welded Specimen GR3 Analysis 89
5.5.2 Welded Specimen Strain Life Analysis 93
5.5.3 Welded Specimen Fatigue Crack Growth Analysis 94
5.5.4 Welded Specimen Total Predicted Lives 99
5.5.5 Comparison of Total and Predicted Lives for the Welded Specimen 100
6.0 Conclusions 102
Bibliography 103

List of Figures

Figure 1. Illustration of how the Neuber stress and strain (B) are related to the elastic stress and strain (A). 4
Figure 2. Fracture Modes. 6
Figure 3. Three Regions of the Fatigue Crack Growth Curve 7
Figure 4. Locations at which stress intensity factors are calculated on a semi-elliptical crack. 9
Figure 5. Decomposition of hot spot stress into a hot spot bending and hotspot membrane stress. 12
Figure 6. Stresses acting near a fillet weld's toe 13
Figure 7. For a pure axial load the nominal stress equals the bending stress. 14
Figure 8. Stress distribution in the weld toe cross section of a T-Joint, with membrane and bending stresses shown. 14
Figure 9. T-Joint Subjected to axial load. 15
Figure 10. Fillet weld under bending load. 16
Figure 11. Butt Weld 17
Figure 12. Butt weld under bending load 18
Figure 13. Illustration of variable involved in Glinka's distribution for stresses near a notch tip 21
Figure 14. A coarse finite element mesh. 22
Figure 15. A finely-meshed weld toe. 22
Figure 16. Coarse (Blue) and Fine (Brown) Mesh Stress Distribution for a T-Joint 23
Figure 17. Stresses extracted from the coarse-mesh finite element model 25
Figure 18. Geometry of the T-Joint [24]. 29
Figure 19. Model of the complete T-Joint geometry. 30
Figure 20. Model of the T-Joint geometry cut along its axis of symmetry 30
Figure 21. Area subjected to x-symmetry boundary condition highlighted in red. 31
Figure 22. Points subjected to pinned boundary condition highlighted in red. 31
Figure 23. Point of application and direction of load marked by red arrow. 32
Figure 24. Types of meshing techniques used during the analysis. 33
Figure 25. Weld toe lines of interest. 33
Figure 26. Global overview of the mesh used for a T-Joint under In-Plane Bending. 34
Figure 27. Mesh in the weld area for a T-Joint under In-Plane Bending. 34
Figure 28. Mesh in the area of interest for a T-Joint under In-Plane Bending. 35
Figure 29. Coarse mesh stress distribution for a T-Joint under in-plane bending. 35
Figure 30. Fine mesh stress distribution for a T-Joint under in-plane bending [24]. 36
Figure 31. Overlay of coarse and fine mesh stress distributions for a T-Joint under in-plane bending. 37
Figure 32. Geometry of the T-Joint [24] 38
Figure 33. Model of the complete geometry of the T-Joint 39
Figure 34. Model of the T-Joint geometry cut along its axis of symmetry 39
Figure 35. Area subjected to y-symmetry boundary condition highlighted in red. 40
Figure 36. Points subjected to pinned boundary condition highlighted in red. 40
Figure 37. Point of application and direction of load marked by red arrow. 41

Figure 38. Types of meshing techniques used during the analysis. 42
Figure 39. Weld toe lines of interest. 42
Figure 40. Global overview of the mesh used for a T-joint in out-of-plane bending. 43
Figure 41. Mesh in the weld area for a T-joint in out-of-plane bending. 43
Figure 42. Mesh in the area of interest for a T-joint in out-of-plane bending. 44
Figure 43. T-Joint coarse mesh stress distribution. 45
Figure 44. T-Joint fine mesh stress distribution [24]. 46
Figure 45. Overlay of coarse and fine mesh stress distributions for the T-Joint. 46
Figure 46. Circular Tube on Plate [24]. 48
Figure 47. Circular Tube on Plate Full Model. 49
Figure 48. Model of the T-Joint geometry cut along its axis of symmetry 49
Figure 49. Area subjected to y-symmetry boundary condition highlighted in red. 50
Figure 50. Points subjected to pinned boundary condition highlighted in red. 50
Figure 51. Point of application and direction of load marked by red arrow. 51
Figure 52. Types of meshing techniques used during the analysis. 52
Figure 53. Weld toe line of interest. 52
Figure 54. Global overview of the mesh used for a circular tube on plate under bending. 53
Figure 55. Mesh in the weld area for a circular tube on plate under bending. 54
Figure 56. Mesh in the area of interest for a circular tube on plate under bending. 54
Figure 57. Coarse mesh stress distribution for a circular tube on plate under bending. 55
Figure 58. Fine mesh stress distribution for a circular tube on plate under bending [24]. 56
Figure 59. Overlay of coarse and fine mesh stress distributions for the circular tube on plate under bending. 56
Figure 60. Dimensions and load acting on circular tube on plate under tension [24]. 58
Figure 61. Circular Tube on Plate Full Model. 59
Figure 62. Model of the T-Joint geometry cut along both axes of symmetry 59
Figure 63. Area subjected to y-symmetry boundary condition highlighted in red. 60
Figure 64. Area subjected to x-symmetry boundary condition highlighted in red. 60
Figure 65. Point subjected to pinned boundary condition highlighted in red. 61
Figure 66. Point of application and direction of load marked by red arrow. 62
Figure 67. Types of meshing techniques used during the analysis. 63
Figure 68. Weld toe line of interest. 63
Figure 69. Global overview of the mesh used for a circular tube on plate under tension. 64
Figure 70. Mesh in the weld area for a circular tube on plate under tension. 64
Figure 71. Mesh in the area of interest for a circular tube on plate under tension. 65
Figure 72. Circular tube on plate bending coarse mesh stress distribution. 66
Figure 73. T-Joint fine mesh stress distribution [24]. 67
Figure 74. Overlay of coarse and fine mesh stress distributions for the T-Joint. 67
Figure 75. Notched Geometry Side View 70
Figure 76. 3D view of the notched bar. 71
Figure 77. Geometric features of a notched bar. 71
Figure 78. 3D view of the welded bar. 72

Figure 79. Geometric features of a butt weld. 72
Figure 80. Geometry of notch used for analysis. 75
Figure 81. Region of application of the x-symmetry boundary condition to the notched geometry. 76
Figure 82. Region of application of the cantilever boundary condition to the notched geometry. 76
Figure 83. Coarse mesh of the notched geometry. 77
Figure 84. Coarse mesh through-thickness stress distribution below the notch tip 77
Figure 85. Comparison of the fine and coarse mesh through-thickness stress distributions below the notch tip. 78
Figure 86. Fine mesh, coarse mesh, and through-thickness stress distribution based on coarse-mesh results. 79
Figure 87. Notched Specimen FALIN Material Data. 81
Figure 88. Notched specimen hysteresis loop. 82
Figure 89. Notched sample through-thickness stress distribution. 83
Figure 90. Notched sample crack initiation 84
Figure 91. Notched sample with a crack across the width 84
Figure 92. FALPR notched sample semi elliptical crack growth output. 85
Figure 93. Replacement of the pair of semi-elliptical cracks with a single edge crack. 86
Figure 94. Notched sample with an obvious edge crack. 86
Figure 95. Failure in the notched sample. 87
Figure 96. Comparison of experimental and predicted fatigue lives for the notched sample. 89
Figure 97. Quarter model of the welded specimen. 90
Figure 98. Region of application of the x-symmetry boundary condition. 90
Figure 99. Region of application of the cantilever boundary condition. 91
Figure 100. Coarsely-meshed welded model. 91
Figure 101. Coarse-mesh stress distribution of the welded specimen. 92
Figure 102. Comparison of coarse and fine finite element mesh distributions. 92
Figure 103. Comparison of coarse and fine finite element distributions, and the stress distribution generated using the coarse finite-element mesh data. 93
Figure 104. Residual stress distribution in the weld toe cross-section. 96
Figure 105. Initiation of cracking in the welded cross-section. 96
Figure 106. Crack across the width of the weldment. 97
Figure 107. Obvious edge crack in the welded geometry. 98
Figure 108. Final failure of the welded component. 99
Figure 109. Comparison of experimental and predicted fatigue lives for the welded sample. 101

List of Tables

Table 1. Notch geometry details 70
Table 2. Weld details. 73
Table 3. Nominal Stresses. 79
Table 4. Nominal Stresses found using the GR3 method. 80
Table 5. Local Elastic Stresses for the Notched Specimen 80
Table 6. Notched specimen strain life predictions 82
Table 7. Number of cycles required for crack to propagate across the thickness of a part for the notched sample. 85
Table 8. Number of cycles required to go from a crack across the width to an obvious edge crack in the notched sample. 87
Table 9. Number of cycles required to go from an obvious edge crack to final failure in the notched sample. 87
Table 10. Predicted lives for the notched sample. 88
Table 11. Experimental lives for the notched sample. 88
Table 12. Maximum local elastic stresses at the weld toe. 94
Table 13. Strain life estimates for the welded configuration. 94
Table 14. Number of cycles required to go from crack initiation to a crack across the width of a part for the welded geometry. 97
Table 15. Number of cycles required to go from a crack across the width to an obvious edge crack in the welded configuration. 98
Table 16. Number of cycles required to go from an obvious edge crack to final failure in the welded geometry. 99
Table 17. Lives to failure for the welded specimen. 99
Table 18. Experimental lives to failure for the welded specimen. 100

Nomenclature

a	Crack size (depth)
a_i	Initial crack size (depth)
A	Instantaneous cross-sectional area
A_0	Original cross section area
b	Fatigue strength exponent
c	Fatigue ductility exponent
C	Fatigue crack growth constant
da/dN	Crack growth rate
$da/dN - \Delta K$	Linear elastic fracture mechanic method (fatigue crack propagation analysis)
D	Fatigue damage
e	Nominal strain
E	Modulus of elasticity
h	Weld height on plate
h_p	Weld height on attachment
K	Stress intensity factor
K_C	Critical stress intensity factor
$K_{\max}$	Maximum stress intensity factor
$K_{\min}$	Minimum stress intensity factor
K_t	Theoretical stress concentration factor
$K_{t,hs}$	Hot spot stress concentration factor
K_σ	Stress concentration factor for $\sigma > \sigma_y$

K_{ε}	Strain concentration factor for $\sigma > \sigma_y$
K'	Cyclic strength coefficient
$K_{t,hs}^{b}$	Hot spot stress concentration factor for pure bending
$K_{t,n}^{b}$	Structural stress concentration factor for pure bending
K^{eff}	Effective stress intensity factor
$K_{\max}^{eff}$	Effective maximum stress intensity factors
$K_{\min}^{eff}$	Effective minimum stress intensity factors
$K_{t,hs}^{m}$	Hot spot stress concentration factor for pure axial loading
K^{res}	Residual stress intensity factor
$K_{t,n}^{t}$	Structural stress concentration factor for pure axial loading
m	Paris equation exponent
$m(y,a)$	Weight function
M	Bending moment
M_1, M_2, M_3	Weight function parameters
n'	Cyclic strain hardening exponent
N	Number of cycles
N_f	Total number of cycles to failure
N_i	Number of cycles to initiate a crack
p	Driving force exponent
P	Applied load
r	Weld toe radius
R	Stress ratio

R^{eff}	Effective stress ratio
S	Nominal stress
$S-N$	The nominal stress method (fatigue analysis)
t	Plate thickness
t_p	Attachment thickness
U	Kurihara parameter

Greek Letters

ΔK	Stress intensity factor range
ΔK_{th}	Threshold stress intensity range
ΔK^{eff}	Effective stress intensity factor range
ΔS	Nominal stress range
$\Delta \varepsilon$	Strain range
$\Delta \sigma$	Stress range
ε	Local strain
$\varepsilon-N$	The strain-life method (fatigue crack initiation analysis)
γ	Fatigue crack growth equation exponent
$\pi = 3.14$	Constant
θ	Weld toe angle
σ	Local stress
σ_{y}	Stress distribution in ' y ' direction
σ_{hs}	Hot spot stress
σ_m	Mean stress

$\sigma_{\max}$	Maximum stress
σ_n	Nominal stress
σ_{Peak}	Peak stress
σ_r	Residual stress
σ_{th}	Threshold stress
σ_y	Material yield stress
σ'_f	Fatigue strength coefficient
σ_{hs}^{b}	Shell bending hot spot stress
σ_n^{ben}	Nominal stress induced by pure bending load
σ_{Peak}^{ben}	Peak stress induced by pure bending load
σ_{hs}^{m}	Shell membrane hot spot stress
σ_n^{ten}	Nominal stress induced by pure tensile load
σ_{Peak}^{ten}	Peak stress induced by pure tensile load

1.0 Introduction

This document describes how a coarse finite element mesh can be used to find the maximum stress acting at the weld toe of a welded joint. This maximum stress value is then typically used to determine the fatigue life of the weldment. By using a coarse finite element mesh to calculate the maximum stress in a weld, fatigue analyses of large and complicated welded structures may be completed even with limited computational resources.

Fatigue life may be calculated using a variety of methods. In this report, both the strain-life method and the fatigue crack growth methods will be examined. Both of these methods require a good estimate for the maximum stress in a weldment.

The maximum stress at the weld toe of a weldment may be much more severe than the nominal stress value that traditional static analysis would indicate, particularly if there are irregularities at the surface. In this paper, a technique known as the hot spot stress concept will be used to determine the maximum stress acting on a weldment. This technique uses a pair of stress concentration factors and the hot spot stress value to determine the maximum stress acting at the weld toe. This method has the advantages of being applicable in almost any situation as well as being easy to use.

At this point, the problem resolves to calculating the hot spot stress acting over the area of interest using coarse-mesh finite element data. For a four-element-thick coarse mesh made up of quadratic elements, it was found that the stress distributions from both the coarse-mesh and fine-mesh models converged over the interior 50% of a cross-section. Using this knowledge, the interior stress distribution is used to predict the hot spot stress, ultimately allowing for a fatigue-life analysis.

The techniques described in this paper are particularly useful in large, statically indeterminate problems where the exact loads at a given cross-section are difficult to find. The arm of an excavator would be a good example of such an assembly. By using a coarse-mesh model, a complete assembly may be modeled. By manipulating the coarse mesh data using the techniques suggested in this report, good estimates for the fatigue life may be found. In contrast, running a fine-mesh analysis would require far more time and processing power.

2.0 Fatigue Analysis

While attempting to describe the mechanical properties of a material, the most common approach is to generate a stress-strain diagram. However, when a stress-strain diagram is created the load is usually applied very slowly, allowing the effects of the strain to be fully manifested. The material is also tested to destruction, so the load is only ever applied once. The resulting data is therefore most useful for static conditions: situations in which the stress level in a part remains constant with respect to time.

In practice, parts are frequently subjected to loads that fluctuate. Components that fail as a result of repeated or fluctuating loads often do so at stress levels well below the ultimate or even yield strength of the material. In order to predict this type of behavior, knowledge of static analysis is generally insufficient. Fatigue is a more complicated phenomenon when compared to static analysis, and knowledge of fatigue and fracture mechanics is essential for designing against this type of failure.

2.1 Literature Background

Fatigue may be defined as the process by which a material fails after repeated exposure to load, ultimately resulting in failure at a load much lower stress than would be expected via static analysis.

Fatigue became of interest to engineers in the mid 1800's, during the industrial revolution. In order to improve upon locomotives and steel bridges which were beginning to appear, the behavior of metals under repeated loads had to be understood. In other to reach this objective, information was collected concerning the circumstances under which structures and components failed.

The first known study into fatigue was conducted by the German mining engineer Albert in the 1829, where he tested metal chains which would later be used in hoists for the mines [1]. A more detailed study was performed by Wohler in the 1850's, where he studied the failure of railway axles [2]. Wohler created diagrams that related the stress a component was subjected to with the number of cycles of load it could take before failing, or an S-N diagram. He observed that below a certain stress, components did not fail, and thereby introduced the concept of a fatigue limit. He also went on to show that the amplitude of the stress acting on a part was more significant than the maximum stress itself.

Goodman went on to show how mean stresses affected the fatigue life of a material [3]. In 1910, Basquin proposed an empirical relationship for the S-N curve of a material, laying the foundations for the modern stress-life approach [4]. The curves tended to follow a linear log-log plot in their finite life regions. In 1920 Griffith wrote a paper detailing the basics of fracture, which would provide the base for the next stage in fatigue life analyses: fatigue crack growth. Unfortunately, his work dealt mostly with glass, and was not used for several decades [5].

By the beginning of the Second World War, fatigue had developed into a major field of research. The linear damage accumulation rule was proposed by Miner, allowing for multiple levels of load to be accounted for during fatigue life analysis [6].

The strain life method was developed by Coffin and Manson, who proposed an empirical relationship between the strain amplitude a component experienced and the fatigue life [7]. They are responsible for developing the idea that plastic strains are responsible for fatigue life. Topper and Morrow also supported the idea of using plastic strains in fatigue life calculations [8]. Their work, combined with Neuber's Rule and the Rainflow fatigue counting method developed by Matsuishi and Endo, provide the basis for modern strain life analysis [9].

Fracture mechanics was pioneered in large part by Irwin, who developed the idea of the stress intensity factor through his studies of the static strength of cracked bodies [10]. Paris later demonstrated that the rate at which a crack grows may be expressed as a function of the stress intensity factor amplitude experienced during loading [11].

The peak stress experienced by a part is required to perform a fatigue analysis. This value can be obtained using either empirical stress intensity factors or finite element analyses. Another alternative approach is to use the hot spot structural stress [12]. The hot spot stress concept was first used for analyzing the welded connections used on offshore structures. Strain gauges are used to pick up the stress acting at a distance from the weld, allowing for the hot spot stress acting at the weld toe to be extrapolated. This stress value can then be combined with nominal stress intensity factors to yield an estimate for the peak stress affecting a part. Some procedures for determining the hot spot stress acting on a structure using shell elements were developed by Niemi [13].

2.2 The Strain-Life Method

The strain life method is used to provide an estimate the number of cycles a component subjected to cyclic load will last before cracks begin to initiate. The first step in performing the strain-life analysis of a component is to find the maximum nominal stress acting on a part. The nominal stress may be found via static analysis, or by the coarse-mesh techniques proposed in this paper. The maximum local elastic stress may then be determined by multiplying the maximum nominal stress with the appropriate stress concentration factor.

Once the maximum local elastic stress has been determined, the Neuber equation may be used to transform the value to maximum local actual stress value [14]. This step is generally only performed if the yield stress of the material has been exceeded, as the elastic and actual stress on a part are identical in the elastic regime. The estimates of the actual stress and strain generated by the Neuber equation (Eq.1) are also known as the Neuber Stress and Neuber Strain.

$$\sigma_{22}^{e}\varepsilon_{22}^{e} = \sigma_{22}^{N}\varepsilon_{22}^{N} \quad (1)$$

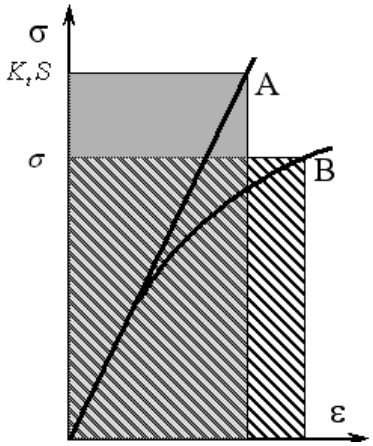

Figure 1. Illustration of how the Neuber stress and strain (B) are related to the elastic stress and strain (A).

Since the Neuber equation has two unknowns in it, the Neuber Stress and Neuber Strain, a second equation is required to solve it. The second equation must relate the stress and strain acting in both the elastic and plastic regimes. The Ramberg-Osgood equation (Eq.2) is often used to accomplish this. The Ramberg-Osgood equation requires a pair of material constants to function, K' and n'. These constants are found experimentally [15].

$$\varepsilon_{22} = \sigma_{22} + \left(\frac{\sigma_{22}}{K'}\right)^{1/n'} \quad (2)$$

Neuber's equation provides a conservative estimate of the actual strain. A non-conservative estimate of the actual strain may be determined using the Equivalent Strain Energy Density (ESED) method [15]. The ESED expression is shown in Eq. 2. The values of K' and n' in the ESED expression are the constants from the Ramberg-Osgood equation, and E is the elastic modulus of the material. Note that the ESED method only has one unknown, and therefore does not need to be solved simultaneously with the Ramberg-Osgood expression.

$$\frac{1}{2}\sigma_{22}^{e}\varepsilon_{22}^{e} = \frac{\sigma_{22}^{a}{}^{2}}{2E} + \left(\frac{\sigma_{22}^{a}}{n'+1}\right)\left(\frac{\sigma_{22}^{a}}{K'}\right)^{1/n'} \quad (3)$$

With the actual strain value, the Manson-Coffin equation may be used to determine the strain life of a component [7]. The Manson-Coffin expression requires the strain amplitude affecting apart to be input, the difference between the maximum and minimum stress values affecting a part. Five

material constants are also required: Young's modulus (E), the true stress (σ'_f) at fracture, the true strain at fracture (ε'_f), and the experimental constants b and c. The expression is shown below:

$$\frac{\Delta\varepsilon}{2} = \frac{\sigma'_f}{E}(2N_f)^b + \varepsilon'_f(2N_f)^c \qquad (4)$$

The value of N_f returned by the expression is the estimate of the number of cycles required to initiate a crack in a material. A crack at initiation usually does not correspond to a failure of a component's ability to carry load, however, and several more cycles of safe life may be obtained from the part is the rate of crack growth in the part may be estimated. In order to perform such an estimate, the fracture mechanics method may be used.

2.3 The Fracture Mechanics Method

The fracture mechanics method is used to estimate the number of cycles of load a component may be exposed to before a crack reaches a critical size. Critical size is usually defined as the point at which a part will experience brittle fracture. However, it should be noted that a part may be considered to have failed from an engineering point of view long before a crack grows to the point that brittle fracture occurs.

Unlike the strain-life method, which uses strain as the independent variable when determining the number of cycles to failure, the fracture mechanics method uses a variable known as the stress intensity factor. The stress intensity factor typically has units of $MPa*m^{1/2}$ in SI units, and is useful in determining the stress intensity at the tip of a crack as a result of a remote load or residual stresses [15].

There are several modes in which fracture can occur. These include opening a crack, shearing a crack in the direction of the crack depth, and shearing the crack in the direction perpendicular to the crack depth. These are often referred to as modes I, II, and III, and are illustrated below [15]:

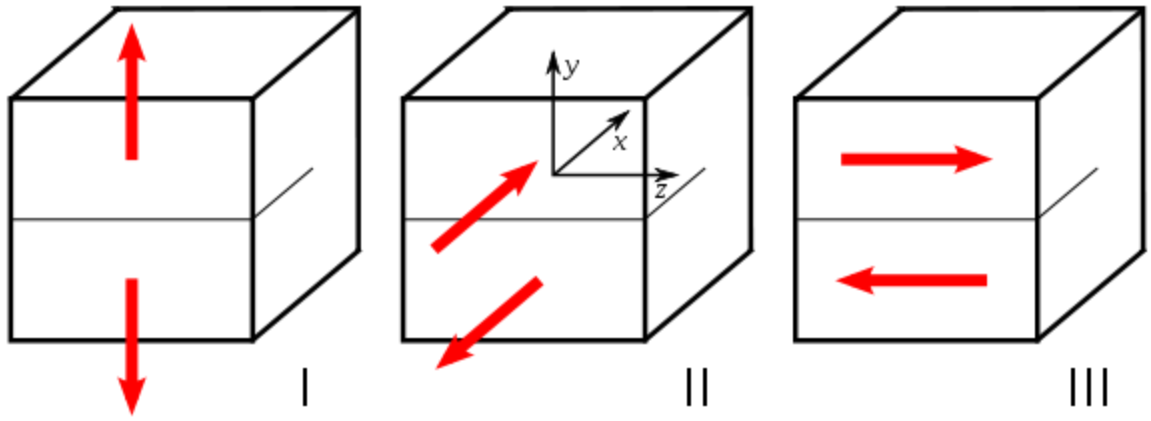

Figure 2. Fracture Modes.

The level of stress intensity is given by the symbol K, followed by a subscript indicating what mode of fracture the stress intensity is referring to. For example, for the stress intensity acting on an opening crack, the symbol would be K_I. Some other critical stress intensity values are K_{th} and K_{Ic}. K_{th} is the threshold stress intensity factor, the stress intensity factor below which a crack will not grow. K_{Ic}, on the other hand, is the critical stress intensity factor, the stress intensity beyond which a part will experience brittle fracture.

The relationship between stress intensity and the number of cycles to failure is given by the da/dN vs. ΔK curve, also known as the fatigue crack growth curve. The value da/dN is the rate at which the crack depth, a, increases with respect to the effective difference in stress intensity acting on a part, ΔK. There are three regions to the curve. In region I, the stress intensity is close to threshold, and the crack grows very slowly. In region II, the graph is nearly linear. Many components operate in this region. Finally, in region III, the material is close to the fracture limit, and crack growth rates are very high. Please note that regions I, II, and III on the fatigue crack growth chart do not necessarily correspond to the fracture modes I, II, and III illustrated in figure 1. A fatigue crack growth graph is shown in figure 2.

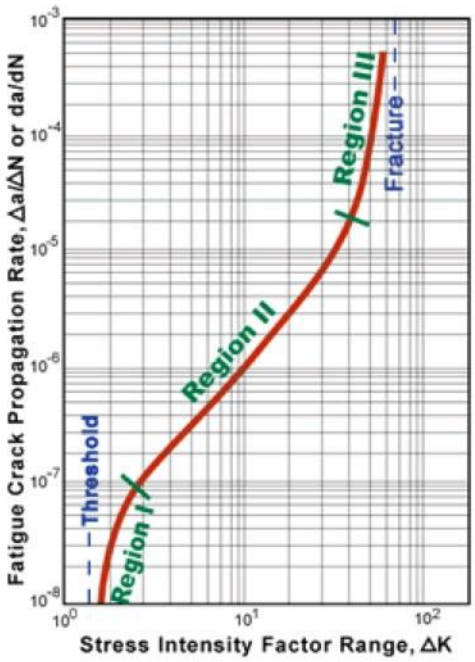

Figure 3. Three Regions of the Fatigue Crack Growth Curve

Several fracture mechanics equations exist that allow for the growth of a crack to be predicted. In this paper, the Paris equation will be used.

2.3.1 The Paris Equation

The Paris equation is applicable in region II of the fatigue crack growth curve, where the logarithmic response of da/dN to ΔK is largely linear. In this region of the fatigue crack growth curve, the Paris equation is applicable. The equation is given below.

$$\frac{da}{dN} = C\ \Delta \mathrm{K}^{\ n} \qquad (5)$$

The Paris equation relies on material constants C and m, as well as the range of stress intensities that affect a part, ΔK. ΔK is defined as $K_{max} - K_{min}$. Once the inputs to the Paris equation are known, it may be solved through integration, with a_i and a_f being the initial and final crack sizes.

$$N_f = \int_{a_i}^{a_f} \frac{da}{C(\Delta K)^m} \qquad (6)$$

As a crack grows, the stress intensity it generates changes. In order to obtain the highest possible accuracy, the da/dN increment should be recalculated after every cycle. The total crack length after a series of cycles would therefore be the initial crack length plus the summation of da/dN values for each increment of crack growth.

$$a_i = a_o + \sum_{i=1}^{N} \Delta a_i = a_o + \sum_{i=1}^{N} C \ \ \Delta K_i \ ^{m} \qquad (7)$$

Using the above equation, a crack may be grown until a_i reaches its critical value, or plastic yielding occurs.

IT should also be noted that the constants for the Paris equation are dependant on the ratio of stress intensity that a component is subjected to. The stress intensity ratio is defined as follows.

$$R = \frac{K_{\min}}{K_{\max}} \qquad (8)$$

Given an R-ratio between -5 and 0.5, Kurihara's equation [16] may be used to convert the actual ΔK value to the effective value, ΔK_{eff}, at an R-ratio of -1. The equation is given below:

$$\frac{\Delta K_{eff}}{\Delta K} = \frac{1}{1.5 - R} \qquad (9)$$

By accounting for the changing stress intensity factor during crack growth and the effect of the R-ratio, the Paris equation can be a very effective tool in computing the life of materials subjected to cyclic load in region II of the fatigue crack growth curve.

2.3.2 Calculation of the Stress Intensity Factor

The stress intensity factor can be determined using a variety of techniques, but for the purposes of this paper the weight function method will be examined. If the correct weight function is known, the stress intensity factor may be determined by integrating the product of the stress distribution σ_y in the crack plane with the weight function m(y,a), where a is the crack length [17]. The expression is shown below:

$$K = \int_0^a \sigma(y) \cdot m(y,a) \cdot dy \qquad (10)$$

Where the generalized weight function for a one dimensional crack m(y,a) is given in Eq. 11.

$$m(y,a) = \frac{2}{\sqrt{2\pi(a-y)}} \left[1 + M_1 \left(1 - \frac{y}{a}\right)^{1/2} + M_2 \left(1 - \frac{y}{a}\right) + M_3 \left(1 - \frac{y}{a}\right)^{3/2} \ldots \right] \qquad (11)$$

This expression is useful for crack geometries such as edge cracks, but two-dimensional crack models are often required to obtain an accurate estimate for the fatigue life of a component [18]. These two dimensional cracks are often semi-elliptical, and have a pair of critical points at which the stress intensity factor must be calculated: the deepest point in the crack, and the surface point. It should be

noted that although there are a pair of surface points, in the case of semi-elliptical crack they will have identical stress intensity factors.

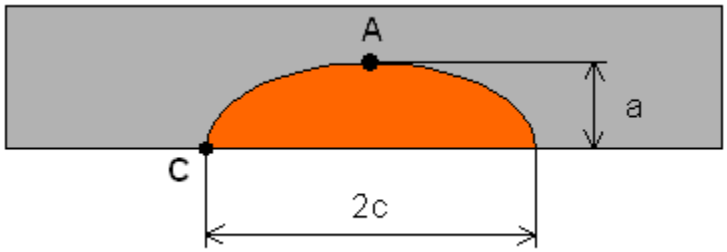

Figure 4. Locations at which stress intensity factors are calculated on a semi-elliptical crack.

The deepest point in a semi-elliptical crack will be referred to as point A, and the surface point as point B. The stress intensity factors for each point much be calculated separately.

$$K_A = \int_0^a \sigma(y) m_A(y,a) dy \qquad (12)$$

$$K_B = \int_0^a \sigma(y) m_B(y,a) dy \qquad (13)$$

Note that the only distinction between Eq. 12 and Eq. 13 is the weight function. The weight functions $m_A(y,a)$ and $m_B(y,a)$ are given below.

$$m_A(y,a) = \frac{2}{\sqrt{2\pi(a-y)}}\left[1 + M_{1A}\left(1-\frac{y}{a}\right)^{1/2} + M_{2A}\left(1-\frac{y}{a}\right) + M_{3A}\left(1-\frac{y}{a}\right)^{3/2}\right] \qquad (14)$$

$$m_B(y,a) = \frac{2}{\sqrt{2\pi y}}\left[1 + M_{1B}\left(\frac{y}{a}\right)^{1/2} + M_{2B}\left(\frac{y}{a}\right) + M_{3B}\left(\frac{y}{a}\right)^{3/2}\right] \qquad (15)$$

Given the weight functions and stress distribution in a component, the stress intensity factors affecting a part may therefore be determined. Those stress intensities, in turn, may be input into the Paris equation to perform a fatigue crack growth analysis.

2.3.3 The Crack Shape Model

As stated earlier, two-dimensional cracks are typically assumed to be semi-elliptical in nature. This is because when planar cracks initiate from a surface, they are most often observed to have an approximately semi-elliptical shape. The depth of the crack is referred to as 'a' and the width of the crack is traditionally assigned a value of '2c'.

The rate of crack growth can be calculated for every cycle in both the ‘c’ and ‘a’ directions, and the tendency is for the cracks to grow faster in width than in depth. As a result of this, semi-elliptical cracks tend to morph into edge cracks if given sufficient time. Also, the difference in growth rates in the ‘a’ and ‘c’ directions therefore results in the crack changing in shape with every cycle. The a/c ratio is often used to characterize the shape of a semi-elliptical crack.

3.0 Stress Concentrations and Distributions in Welded Connections

The maximum stress acting on a weldment is found by first determining the nominal stress acting on the weldment at the location of interest, and then using the appropriate stress concentration factor to determine the maximum elastic stress value. These stress concentration factors are usually found from handbooks. Finite element methods are also used to determine the maximum stress acting on a weldment, and have the advantage of being effective regardless of how strange geometry is, while handbooks are limited to standard shapes.

The stress state in a weld is multiaxial, but resolves to two normal and a single shear component at the surface. The stress concentration that occurs at the weld toe results in the stress component normal to the weld toe generating most of the fatigue damage.

The maximum elastic stress, or peak stress, acting on a cross-section is found using the appropriate stress concentration factor and the nominal stress at the weld toe of a weldment. The peak stress may be found using the following expression:

$$\sigma_{Peak} = K_t \sigma_n \qquad (16)$$

Similarly, the hot spot stress may also be used to determine the peak stress, and will be covered in the following section.

$$\sigma_{Peak} = K_{t,hs} \sigma_{hs} \qquad (17)$$

3.1 The Hot Spot Stress Concept

The hot spot stress concept was first used to perform structural analyses on offshore structures [19]. Strain gauges placed at known distances from a weld were used to extrapolate a stress value at the weld toe, known as the hot spot stress. The strain gauges had to be placed sufficiently far away from the weld to be unaffected by the geometric effect of the weld toe on the strain readings, and distances of 0.4t and 1t are typically used, where t is the thickness of the plate [20].

The hot spot stress can be used to determined the peak stress via the hot spot stress concentration factor, $K_{t,hs}$. The hot spot stress is itself the sum of the membrane and bending stresses acting at the surface of a weldment [21]. The bending stress is referred to as the stress generated by the moment acting on a weldment, and the membrane stress is the result of the compressive or tensile forces on the weldment. The hot spot stresses can therefore be decomposed into the normal and bending stresses if the hotspot stress on both the compression and tension surfaces of a weldment is known. These hot spot stresses are also referred to as shell stresses. The shell stresses are labeled σ_A

and σ_B. The axial and bending stresses obtained by decomposing the shell stresses are referred to be σ^m_{hs} and σ^b_{hs}.

$$\sigma^m_{hs} = \frac{\sigma_A + \sigma_B}{2} \qquad (18)$$

$$\sigma^b_{hs} = \frac{\sigma_A - \sigma_B}{2} \qquad (19)$$

The decomposition from shell stresses to membrane and bending stresses is shown pictorially in the following figure:

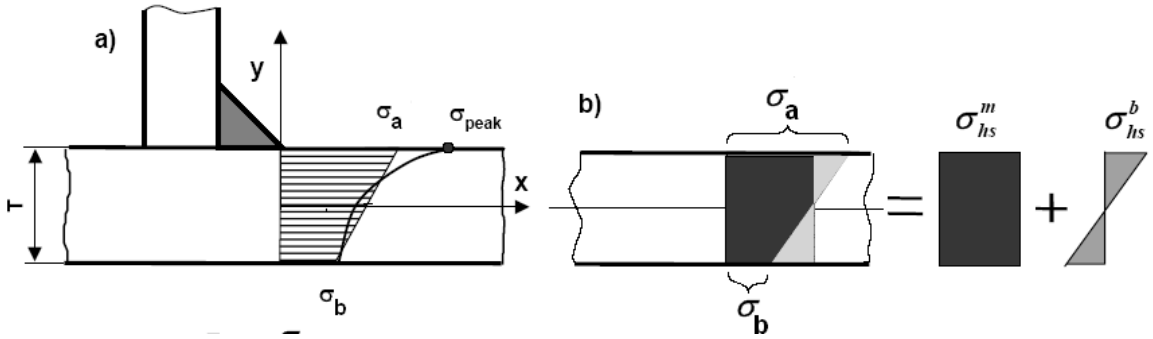

Figure 5. Decomposition of hot spot stress into a hot spot bending and hotspot membrane stress.

Since the hot spot stress varies with the level of membrane and bending stress acting on a weldment, the value of $K_{t,hs}$ also varies with the ratio of $\sigma^m_{hs}/\sigma^b_{hs}$. As a result of this, a table of $K_{t,hs}$ values would be required to determine the peak stress value for any given geometry. An alternative is to break up the stress concentration factor into a pair of factors: $K^b_{t,hs}$ for the bending stress and $K^m_{t,hs}$ for the membrane stress [21]. Using a pair of stress concentration factors, the peak stress is determined according to the following expression:

$$\sigma_{Peak} = \sigma^m_{hs} \cdot K^m_{t,hs} + \sigma^b_{hs} \cdot K^b_{t,hs} \qquad (20)$$

The advantage to Eq. 18 is that the ratio between the bending and membrane stresses no longer effects the stress concentration factor, allowing for the table of the factors to be greatly simplified.

3.2 Stress Concentration Factors near Fillet Welds

The stress concentration factor near a fillet weld may be obtained using analytical, numerical, or experimental techniques for any given loading mode. The value for hot spot stress and nominal stress are identical in the case of either pure bending or pure axial loading. Given this relationship, in the case of purely axial loading the following statement is true:

$$\sigma_{hs} = \sigma_{hs}^{m} = \sigma_{n}^{ten} \qquad (21)$$

Likewise, for pure bending the hotspot and nominal stresses are related as follows:

$$\sigma_{hs} = \sigma_{hs}^{b} = \sigma_{n}^{bend} \qquad (22)$$

The stress distributions acting in the vicinity of a fillet weld is shown in the following figure. Stress field 'A' denotes the normal stress distribution in the weld throat. Stress field B marks the normal stress distribution in the plate at the weld toe, and C the normal stress distribution away from the weld toe. Stress field D illustrates how the normal stress decreases with separation from the weld toe. Stress field E shows the shear stress distribution in the weld throat. Finally, Stress field F shows the hot spot stress distribution at the weld toe [21].

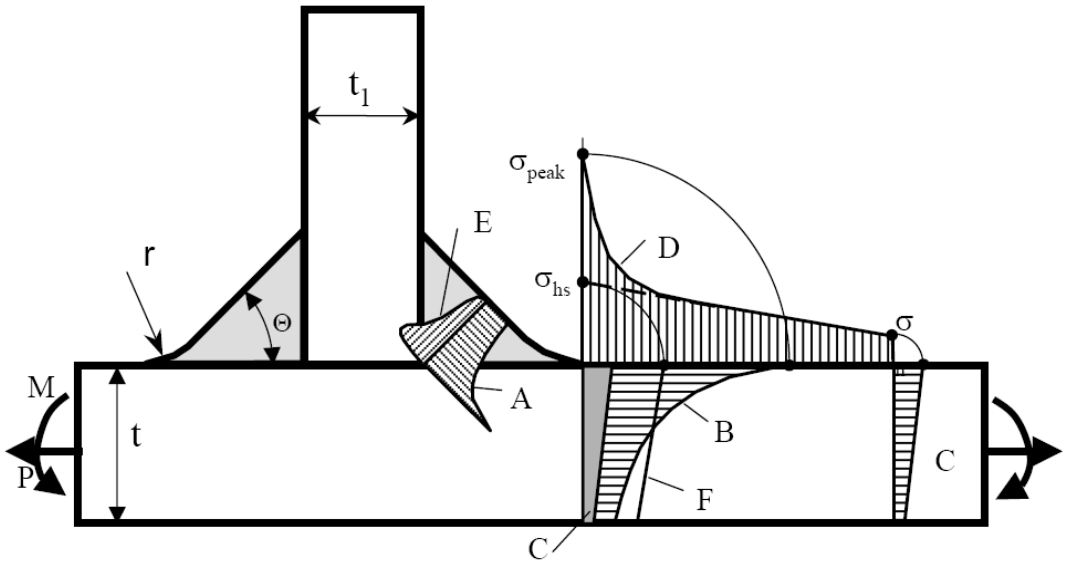

Figure 6. Stresses acting near a fillet weld's toe

Since the nominal stresses are equal to the hotspot stresses for pure axial and pure bending loads, the stress concentration factors required to predict the peak stress in a geometry would therefore also be identical. For axial loading, the stress concentration factors are related as follows:

$$K_{t,n}^{t} = K_{t,hs}^{t} = \frac{\sigma_{Peak}^{ten}}{\sigma_{n}^{ten}} = \frac{\sigma_{Peak}^{ten}}{\sigma_{hs}^{m}} \qquad (23)$$

The relationship between the hot spot stress and nominal stress is shown in the following figure:

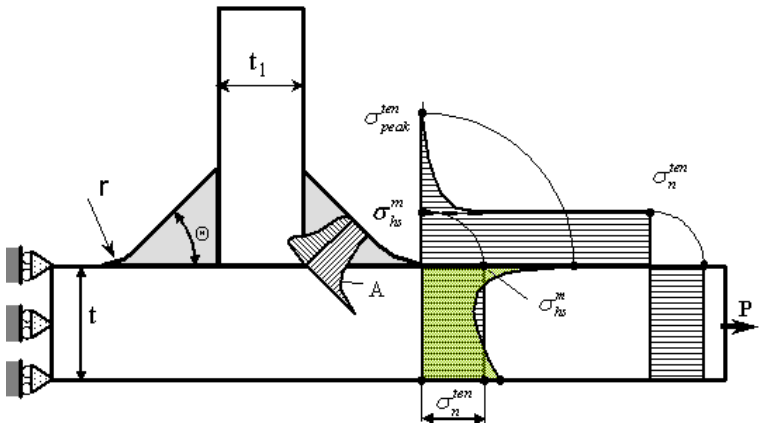

Figure 7. For a pure axial load the nominal stress equals the bending stress.

Likewise, the bending stress concentration factors are related as follows:

$$K^b_{t,n} = K^b_{t,hs} = \frac{\sigma^{ben}_{Peak}}{\sigma^{ben}_{n}} = \frac{\sigma^{ben}_{Peak}}{\sigma^{b}_{hs}} \qquad (24)$$

Using this information, the expression for determining the peak stress in a mixed bending and axial loading situation may be rewritten using the nominal stress concentration factors. By using the nominal stress concentration factors, any stress concentration factor handbook may be used to go from the hot spot stresses to the peak stress value.

$$\sigma_{Peak} = \sigma^m_{hs} \cdot K^t_{t,n} + \sigma^b_{hs} \cdot K^b_{t,n} \qquad (25)$$

The combined effect of the bending and axial stresses on a weldment are shown in the following figure:

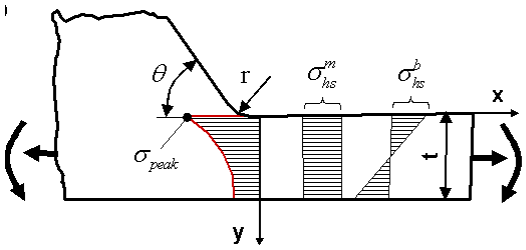

Figure 8. Stress distribution in the weld toe cross section of a T-Joint, with membrane and bending stresses shown.

The hot spot axial and bending stresses equal the nominal axial and bending stresses. The axial and bending stress concentration factors are then multiplied into the axial and bending stress values respectively, and the sum of the two results in the peak stress value.

3.2.1 Stress Concentration Factors for a T-Joint Subjected to an Axial Load

There are several empirical expressions used to estimate the stress concentration factor for a T-Joint subjected to an axial load. The following expression is suggested by Monahan [22], and provides a conservative estimate of the stress concentration factor in question. In this expression, Θ is the angle between the weld and the plate, t is the thickness of the plate, and r is the weld toe radius.

$$K_{t,hs}^{m} = 1 + 0.388\theta^{0.37} \cdot \left(\frac{t}{r}\right)^{0.454} \qquad (26)$$

A less conservative estimate for the stress concentration factor was suggested by Iida and Uemura [23], which accepts more geometric inputs than the expression suggested by Monahan.

$$K_{t,n}^{t} = K_{t,hs}^{m} = \frac{1 - \exp\left(-0.9\theta\sqrt{\frac{W}{2h}}\right)}{1 - \exp\left(-0.45\pi\sqrt{\frac{W}{2h}}\right)} \cdot \left(\frac{1}{2.8\left(\frac{W}{t}\right) - 2} \cdot \frac{h}{r}\right)^{0.65} \qquad (27)$$

Where W is defined as follows:

$$W = (t + 2h) + 0.3(t_p + 2h_p) \qquad (28)$$

The variables used in the above expressions are shown in the following figure:

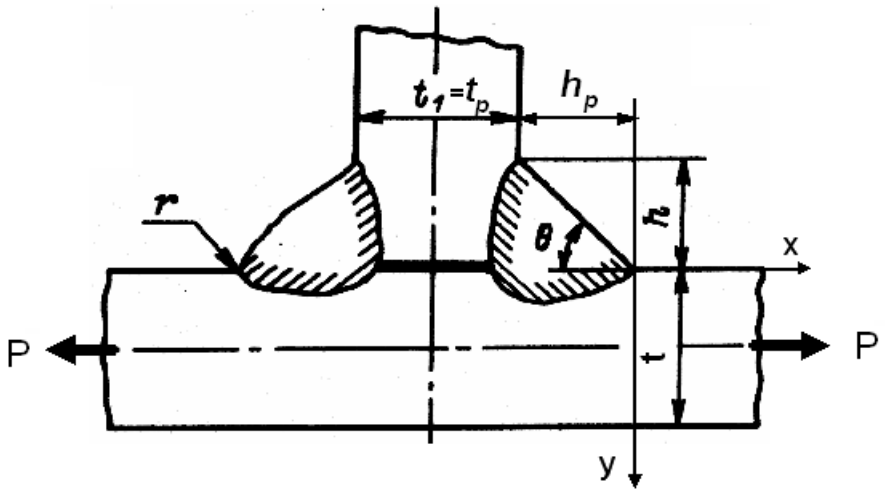

Figure 9. T-Joint Subjected to axial load.

The expression suggested by Iida and Uemura have been verified for values of r/t ranging from 0.025 to 0.4, and for Θ in the range of 20° to 50°. Eq. 27 and Eq. 28 were used to find the stress concentration factors for the analyses presented in this report.

3.2.2 Stress Concentration Factors for a T-Joint Subjected to a Bending Load

Empirical equations also exist to calculate the stress concentration factor in the case of a bending load. The following expression is suggested by Monahan [22], and provides a conservative estimate of the stress concentration factor in question. In this expression, Θ is the angle between the weld and the plate, t is the thickness of the plate, and r is the weld toe radius.

$$K_{t,hs}^{b} = 1 + 0.512\theta^{0.572} \cdot \left(\frac{t}{r}\right)^{0.469} \qquad (29)$$

Similarly, Iida and Uemura [23] determined a less conservative estimate for the stress concentration factor in a fillet weld under bending:

$$K_{t,n}^{b} = K_{t,hs}^{b} = 1 + \frac{1 - \exp\left(-0.9\theta\sqrt{\frac{W}{2h}}\right)}{1 - \exp\left(-0.45\pi\sqrt{\frac{W}{2h}}\right)} \cdot 1.9\sqrt{\tanh\left(\frac{2t_p}{t+2h} + \frac{2r}{t}\right)} \cdot \tanh\left(\frac{\left(\frac{2h}{t}\right)^{0.25}}{1-\frac{r}{t}}\right) \cdot \left(\frac{0.13 + 0.65\left(1-\frac{r}{t}\right)^{4}}{\left(\frac{r}{t}\right)^{1/3}}\right) \qquad (30)$$

W is defined in Eq. 28. The expression is valid for r/t values ranging from 0.025 to 0.4, and for values of Θ between 20° and 50°. The remaining variables are shown in the following figure:

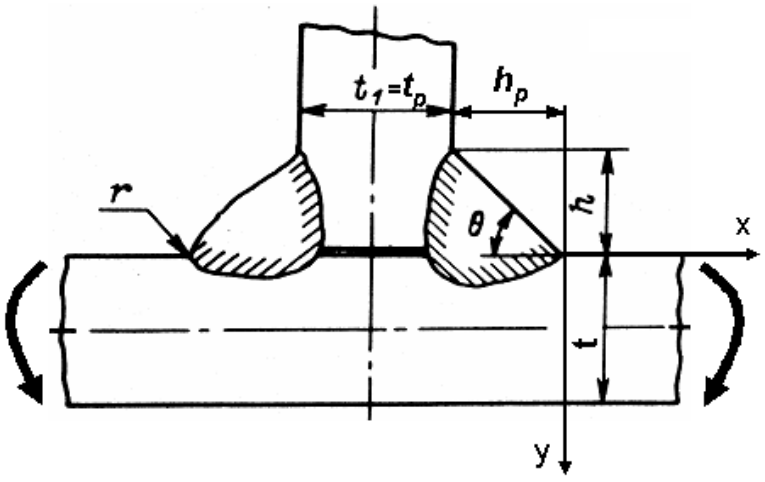

Figure 10. Fillet weld under bending load.

Bending stress concentration factors were calculated using Eq.30 in this report.

3.3 Stress Concentration Factors near Butt Welds

The other type of geometry that will be examined in this report in the butt weld. Similar to the fillet weld, the nominal and hot spot stress concentration factors acting on a butt weld are identical during pure axial load and pure bending load. The shell stresses for any loading case may therefore be measured and decomposed into the bending and axial components, as shown in Eq. 18 and Eq.19.

Once the bending and axial loads are determined, they may be multiplied by the appropriate values of $K^{b}_{t,n}$ and $K^{t}_{t,n}$ respectively, and summed to estimate the peak stress acting at the weld toe as shown in Eq. 25.

3.3.1 Stress Concentration Factors for a butt joint Subjected to an Axial Load

The stress concentration factor used to determine the peak stress in the butt weld subjected to an axial load was developed by Iida and Uemura [23]. It is shown below:

$$K^{m}_{t,hs} = 1 + \frac{1 - \exp\left(-0.9\theta\sqrt{\frac{W}{2h}}\right)}{1 - \exp\left(-0.45\pi\sqrt{\frac{W}{2h}}\right)} \times 2\left[\frac{1}{2.8\left(\frac{W}{t}\right) - 2} \times \frac{h}{r}\right]^{0.65} \quad (31)$$

Where:

$$W = t + 2h + 0.6h_p \quad (32)$$

The variables used in the above expressions are shown in the follow figure:

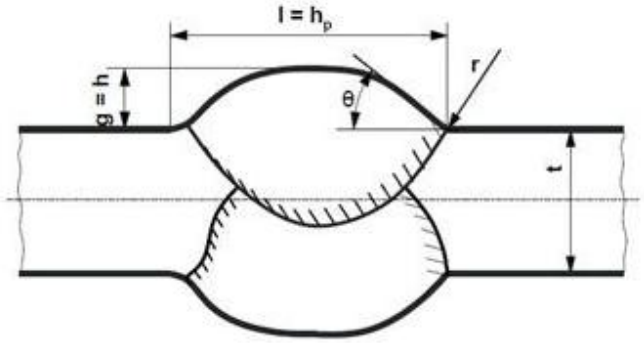

Figure 11. Butt Weld

The expression suggested by Iida and Uemura have been verified for values of r/t ranging from 0.025 to 0.4, and for Θ in the range of 20° to 50°. Eq. A and Eq. B were used to find the stress concentration factors for the analyses presented in this report.

3.3.2 Stress Concentration Factors for a butt Joint Subjected to a Bending Load

The stress concentration factor used to determine the peak stress in the butt weld subjected to an bending load was developed by Iida and Uemura [23]. It is shown below:

$$K^{b}_{t,hs} = 1 + \frac{1 - \exp\left(-0.9\theta\sqrt{\frac{W}{2h}}\right)}{1 - \exp\left(-0.45\pi\sqrt{\frac{W}{2h}}\right)} \times 1.5\sqrt{\tanh\left(\frac{2r}{t}\right)} \times \tanh\left[\frac{\left(\frac{2h}{t}\right)^{0.25}}{1 - \frac{r}{t}}\right] \times \left[\frac{0.13 + 0.65\left(1 - \frac{r}{t}\right)^{4}}{\left(\frac{r}{t}\right)^{\frac{1}{3}}}\right] \quad (33)$$

Where W is defined as it was in Eq. 31.

The variables used in the above expressions are shown in the following figure:

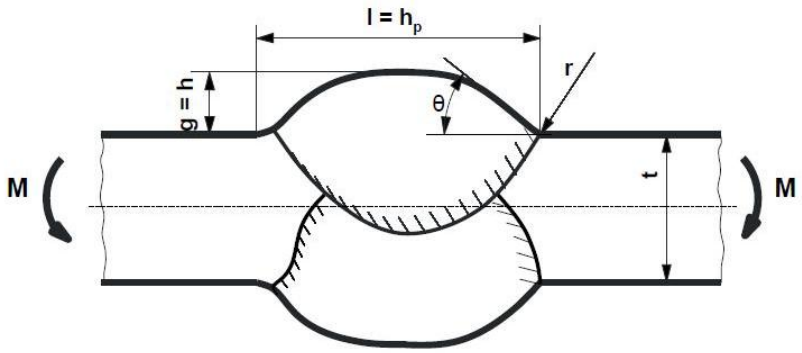

Figure 12. Butt weld under bending load

The expression suggested by Iida and Uemura have been verified for values of r/t ranging from 0.025 to 0.4, and for Θ in the range of 20° to 50°. Eq. C and Eq. D were used to find the stress concentration factors for the analyses presented in this report.

3.4 Simulation of the Stress Distribution in the Weld Toe Cross-Section

The stress distribution through a cross-section is useful in performing fatigue crack growth analysis of a weldment. In order to perform such an analysis, the product of the weight function stress field must be integrated to generate the stress intensity factor value, as shown in

The stress distribution in the weld toe cross-section may be simulated using relationships relating the peak stress affecting a weldment and the weldment's geometry. A common approach for fillet welds is to use Monahan's Equation to estimate the stress distribution through a cross section based off of the geometry of the weld and the peak stress acting in the weldment.

For other geometries, such as a butt weld, a stress distribution suggested by Glinka was found to generate a stress distribution almost identical to that generated by a fine-mesh finite-element analysis.

3.4.1 Monahan's Equation

Monahan's equation is very useful in estimating the stress distribution at the weld toe cross section of a fillet weld. It requires only the peak stress of the weld, and several geometric values describing the shape of the weld itself [22].

The stress distribution suggested by Monahan for a weldment subjected to axial load is given below:

$$\sigma(y) = \frac{K_{t,hs}^{m}\sigma_{hs}^{m}}{2\sqrt{2}}\left[\left(\frac{y}{r}+\frac{1}{2}\right)^{-1/2}+\frac{1}{2}\left(\frac{y}{r}+\frac{1}{2}\right)^{-3/2}\right]\frac{1}{G_m} \tag{34}$$

Where:

$$K_{t,hs}^{m} = 1+0.388\cdot\theta^{0.37}\left(\frac{r}{t}\right)^{-0.454} \tag{35}$$

$$G_m = 1 \ \ for \ \frac{y}{r} \le 0.3 \tag{36}$$

$$G_m = 0.06+\frac{0.94\cdot\exp\ -E_m\cdot T_m}{1+\ E_m{}^{3}\ T_m{}^{0.8}\cdot\exp\ -E_m\cdot T_m{}^{1.1}} \ \ for \ \frac{y}{r} > 0.3 \tag{37}$$

$$E_m = 1.05\cdot\theta^{0.18}\left(\frac{r}{t}\right)^{q} \tag{38}$$

$$q = -0.12\theta^{-0.62} \tag{39}$$

$$T_m = \frac{y}{t} - 0.3\frac{r}{t} \tag{40}$$

The through thickness stress distribution generated by the bending load is given by the following set of expressions:

$$\sigma(y) = \frac{K^b_{t,hs}\sigma^b_{hs}}{2\sqrt{2}}\left[\left(\frac{y}{r}+\frac{1}{2}\right)^{-1/2} + \frac{1}{2}\left(\frac{y}{r}+\frac{1}{2}\right)^{-3/2}\right]\frac{1-2\left(\frac{y}{t}\right)}{G_b} \tag{41}$$

Where:

$$K^b_{t,hs} = 1 + 0.512\cdot\theta^{0.572}\left(\frac{r}{t}\right)^{-0.469} \tag{42}$$

$$G_b = 1 \ \ for \ \frac{y}{r} \le 0.4 \tag{43}$$

$$G_b = 0.07 + \frac{0.93\cdot\exp\ -E_b\cdot T_b}{1+\ E_b{}^{3}\ T_b{}^{0.6}\cdot\exp\ -E_b\cdot T_b^{1.2}} \ \ for \ \frac{y}{r} > 0.4 \tag{44}$$

$$E_b = 0.9\left(\frac{r}{t}\right)^{-\left(0.0026+\frac{0.0825}{\theta}\right)} \tag{45}$$

$$T_b = \frac{y}{t} - 0.4\frac{r}{t} \tag{46}$$

The axial and bending stress distribution may be superimposed to determine the overall stress distribution acting on a cross-section. The simplified comprehensive expression for the stress distribution generated by a combined axial and bending load on a fillet weld is given below:

$$\sigma(y) = \left[\frac{K^m_{t,hs}\sigma^m_{hs}}{2\sqrt{2}}\cdot\frac{1}{G_m} + \frac{K^b_{t,hs}\sigma^b_{hs}}{2\sqrt{2}}\cdot\frac{1-2\left(\frac{y}{t}\right)}{G_b}\right]\left[\left(\frac{y}{r}+\frac{1}{2}\right)^{-1/2} + \frac{1}{2}\left(\frac{y}{r}+\frac{1}{2}\right)^{-3/2}\right] \tag{47}$$

The above expression can therefore be used to go from a peak stress and geometric features to the stress distribution at the weld-toe cross section of a fillet weld. This information may then be used for subsequent fatigue crack growth analysis, which would otherwise require fine mesh analysis to generate a reliable representation of the stress distribution.

3.4.2 Glinka's Notch Tip Stress Distribution

Although Monahan's equation provides a good estimate for the stress distribution in the case of a fillet weld, it can fail to provide a reasonable stress distribution in the case of a butt weld or a notch. The distribution suggested by Glinka [15] provides a good match to fine-mesh finite element results for most cases. The expression is shown below:

$$\sigma_{yy} = \frac{\sigma_{peak}}{2}\left[\left(\frac{x}{r}+1\right)^{-2} + \left(\frac{x}{r}+1\right)^{-4}\right]\left(1-\frac{x}{\kappa}\right) \quad for \; x < 3.5r \qquad (48)$$

Where κ is the distance from the notch tip to the neutral axis, and r is the notch tip radius. It should be noted that for a case of pure axial loading, κ goes to infinity.

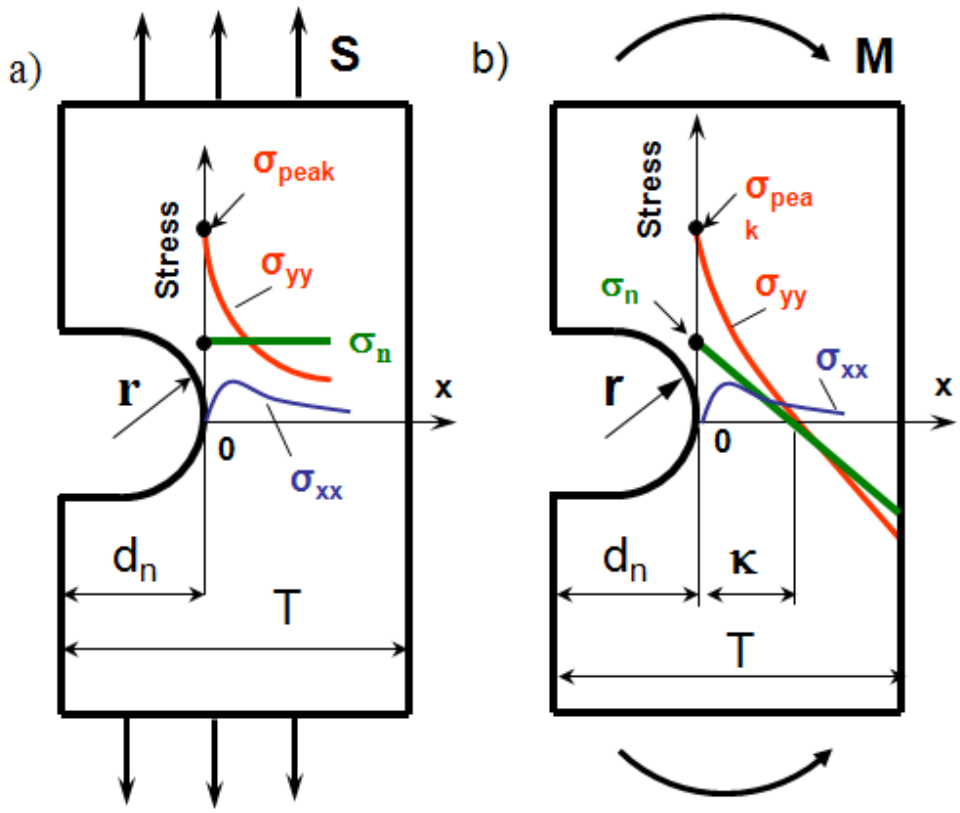

Figure 13. Illustration of variable involved in Glinka's distribution for stresses near a notch tip

The expression is only accurate out to 3.5 notch radii, however, after which point it should be merged with the nominal stress distribution in the cross-section of the weldment as smoothly as possible.

4.0 Coarse Three-Dimensional Mesh Finite Element Model

The coarse finite element mesh used, also known as the GR3 method, allows for the peak stress acting at a critical cross section to be determined using a finite element mesh only 4 elements thick, along with some post-processing. The weld toe is modeled as a sharp corner. An example of such a course mesh is shown in the following figure:

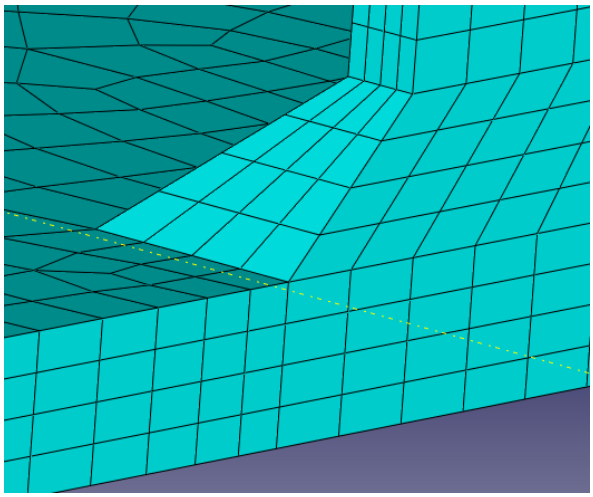

Figure 14. A coarse finite element mesh.

Weld toe radii and other small notch-like features in a geometry have the effect of creating sharp stress spikes in a weldment, and need to be carefully meshed in order to create a reliable stress estimate. Meshing such small features often requires millions of additional finite elements in order to achieve a reliable estimate of their effect. This is shown in the following figure:

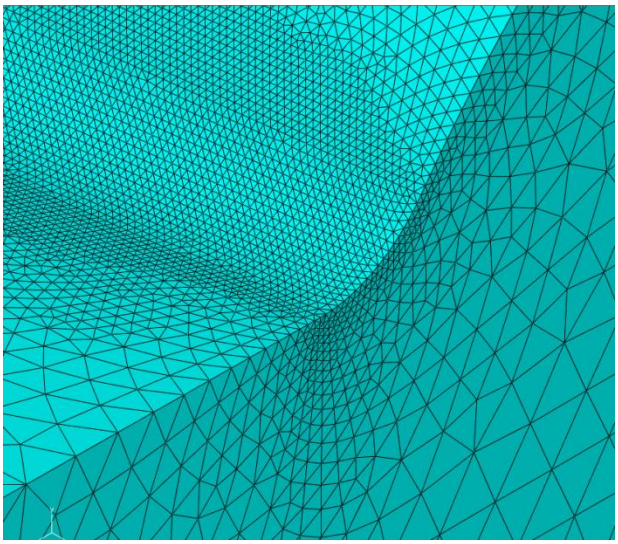

Figure 15. A finely-meshed weld toe.

By using a coarse finite element mesh and accounting for the effects of weld toe radii and other comparable features in post-processing, large and complicated structures subjected to complex loadings may be analyzed quickly.

The coarse finite element mesh does not give a good estimate of the stress at the weld toe unless it is properly post-processed. Initially, the coarse finite element mesh will underestimate the stress at the surface. A comparison between the output of a coarse finite element mesh model and a fine finite element mesh model with the weld toe modeled is shown in the following figure:

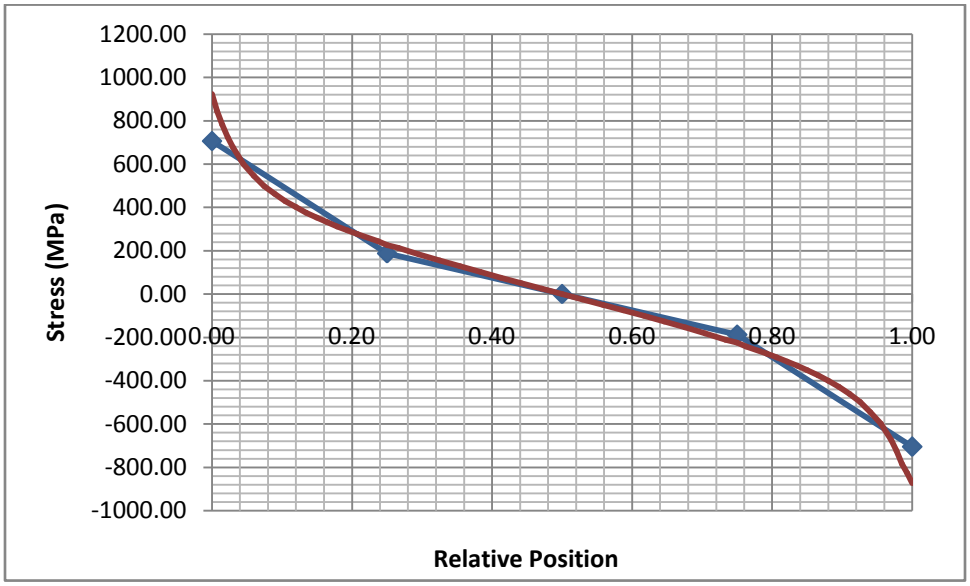

Figure 16. Coarse (Blue) and Fine (Brown) Mesh Stress Distribution for a T-Joint

The difference in peak stress estimated by the coarse and fine finite element meshes is considerable. However, over the inboard 50% of the cross-section, there does not appear to be much difference between the output of the fine finite element mesh and the coarse one. Therefore, the only reliable data generated by the coarse finite element mesh is only over the inboard half of the cross-section.

This observation would typically be quite useless from and engineering point of view, as the peak stresses in a weldment almost invariably occur at the surface of a weldment. However, by examining several different welded geometries, it was found that the inboard 50% of the cross-section always accounts for 10% of the total moment acting on a cross-section. Therefore, by calculating the moment generated by the inboard 50% of the cross-section from the coarse finite element data and multiplying by 10, the total moment acting on a cross-section could be found.

In a generalized loading case, a cross-section may be subjected to both a moment and an axial load. The axial load was calculated by simply integrating the stress distribution over the area of the cross-section.

The two above methods extract the acting moment and load at a given cross-section from the coarse mesh data. Now that that information is known, the nominal bending and axial stresses may be calculated using classical analysis. The bending stress acting is found using the following expression:

$$\sigma_n^{bend} = \frac{Mc}{I} \qquad (49)$$

Where M is the moment extracted from the coarse mesh data, c is the distance from the weld toe to the neutral axis, and I is the moment of inertia of the cross-section. The procedure for extracting the value of the moment M from the coarse finite element mesh data will be covered in Section 4.2.

The membrane stress is found using the following expression:

$$\sigma_n^{ten} = \frac{P}{A} \qquad (50)$$

Where P is the load extracted from the coarse-mesh data and A is the cross-sectional area. The procedure for extracting the load P from the coarse finite element mesh data will be covered in Section 4.3.

At this point, the bending and axial stress concentration factors may be calculated using the expressions suggested by Iida and Uemura. The nominal bending and membrane stresses are then entered into Eq.25 along with the stress concentration factors, yielding the peak stress value.

The peak stress value may then be used to perform a strain life analysis, as outlined in Section 2.1. However, if fatigue crack growth analysis is required, a full stress distribution must be found. The stress distribution may be calculated using Monahan's equation in the case of a fillet weld, or the method proposed by Glinka for other cases.

4.1 Procedure for Generating the Coarse 3D Finite Element Mesh

The finite element mesh should be four elements thick, and care should be taken to keep aspect ratios in the vicinity of the weld toe should be no greater than 3. It is also convenient if mesh seeds are placed at both surface, and at locations 25%, 50%, and 75% through the thickness of the cross-section. This is not a necessity, however, and merely makes it easier to extract the stress values from the required locations. If the nodes are at different locations, the stresses at the locations 25% and 75% through the cross-section may be interpolated from the values at the other nodes.

An important detail is that for the 4-element thick mesh to work, the order of the elements in the mesh must be quadratic. Linear elements will not provide sufficient accuracy.

The mesh elements may be either hexagonal or tetrahedral in shape.

4.2 Calculation of the Total Moment from the Finite Element Mesh Data

The total moment acting on the cross-section may be determined by first extracting the stress values acting at locations 25%, 50%, and 75% through the cross-section. These three points define the stress values acting at the nodes of the two interior element of the GR3 model. This is illustrated in the following figure, with the required stress values highlighted in red, and the inboard 50% of the cross-section highlighted in violet:

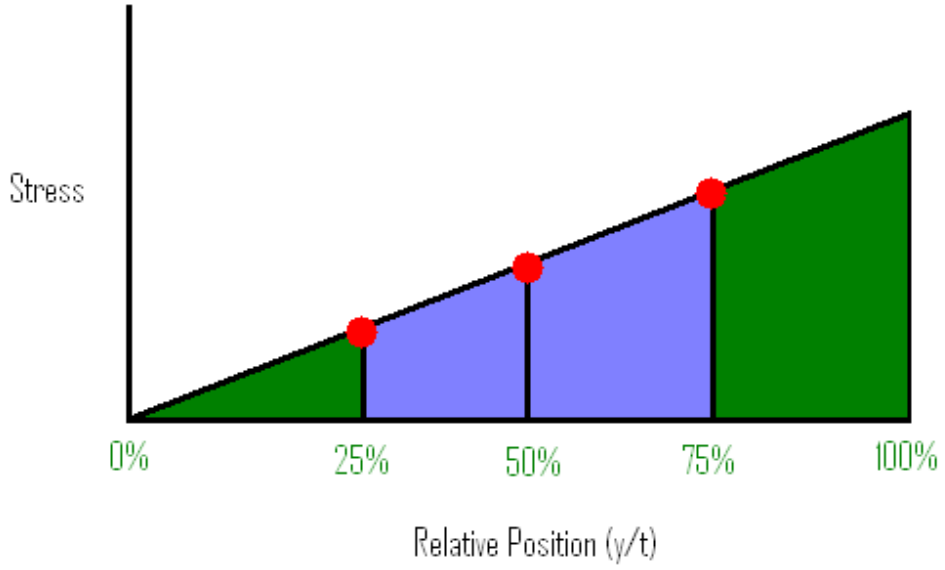

Figure 17. Stresses extracted from the coarse-mesh finite element model

In general, the moment generated by a stress field over a slice of depth Δx of a planar cross section is defined by the following integral:

$$M_b = \int_0^{t_y} \int_{x_i}^{x_i+\Delta x} \sigma(x,y) \cdot (y_{NA} - y) \cdot dx \cdot dy \qquad (51)$$

For a unit thickness slice of a cross section, and assuming that the change in stress value in the x direction is small, the double integral can be done away with and the moment generated by a stress distribution is described by the following integral:

$$M_b = \int_0^t \sigma(y) \cdot (y_{NA} - y) \cdot dy \qquad (52)$$

Where 'σ(y)' is the stress distribution, 'y_{NA}' is the position of the neutral axis, and 'y' is a position along the through thickness. The value 't' represent the thickness of the cross-section.

As stated in Section 4.0, the moment generated by the inboard 50% of the cross-section account for 10% of the total moment acting on the cross section. This relationship is captured by the following expression:

$$M_b = 10 \cdot M_{Inboard} \qquad (53)$$

In the case of the coarse mesh model, the inboard moment, $M_{Inboard}$, may be found by numerical integrating the linear stress distributions from 25% to 50% of the thickness, and then from 50% to 75% of the thickness. The linear stress distribution spanning the i'th element may be expressed in the following form:

$$\sigma_i(y) = a_i y + b_i \qquad (54)$$

The a_i term is defined as follows:

$$a_i = \frac{\sigma_i - \sigma_{i+1}}{y_i - y_{i+1}} \qquad (55)$$

And the b_i term is defined below:

$$b_i = \frac{\sigma_{i+1} \cdot y_i - \sigma_i \cdot y_{i+1}}{y_i - y_{i+1}} \qquad (56)$$

The expression for the stress distribution, Eq. 54, may be substituted into Eq. 52, and integrated to create as estimate for the moment generated by an i'th slice. The expression is given below:

$$M_{b,i} = \frac{\sigma_i - \sigma_{i+1} \quad y_i^3 - y_{i+1}^3}{3 \;\; y_i - y_{i+1}} + \left[\;\; \sigma_i - \sigma_{i+1} \;\; y_{NA} - \sigma_{i+1} y_i + \sigma_i y_{i+1} \right] \frac{y_i + y_{i+1}}{2} - \;\; \sigma_{i+1} y_i - \sigma_i y_{i+1} \;\; y_{NA} \qquad (57)$$

The total moment can then be found by summing the moment generated by the two inboard elements of the coarsely-meshed cross-section. The total moment is therefore expressed as follows:

$$M_{Inboard} = \sum_{i=2}^{3} \frac{\sigma_i - \sigma_{i+1} \quad y_i^3 - y_{i+1}^3}{3 \quad y_i - y_{i+1}} + \sum_{i=2}^{3} \left[\sigma_i - \sigma_{i+1} \quad y_{NA} - \sigma_{i+1} y_i + \sigma_i y_{i+1} \right] \frac{y_i + y_{i+1}}{2} - \sum_{i=2}^{3} \sigma_{i+1} y_i - \sigma_i y_{i+1} \quad y_{NA}$$

(58)

Finally, now that the inboard moment is known, the total moment may be found using Eq. 53. The slices 2 and 3 refer to the slices going from 25% to 50% of the way through the through thickness and from 50% to 75% of the through thickness. The result is shown below:

$$M_b = 10 \left\{ \sum_{i=2}^{3} \frac{\sigma_i - \sigma_{i+1} \quad y_i^3 - y_{i+1}^3}{3 \quad y_i - y_{i+1}} + \sum_{i=2}^{3} \left[\sigma_i - \sigma_{i+1} \quad y_{NA} - \sigma_{i+1} y_i + \sigma_i y_{i+1} \right] \frac{y_i + y_{i+1}}{2} - \sum_{i=2}^{3} \sigma_{i+1} y_i - \sigma_i y_{i+1} \quad y_{NA} \right\}$$

(59)

At this point, the bending stress may be found using classical analysis, as shown in Eq.49.

4.3 Calculation of the Total Load from the Finite Element Mesh Data

The total load acting on the cross-section must also be determined from the coarse-mesh finite-element data. In contrast to the calculation of the moment, where only the inboard data points were used, the total load is found using all of the nodes of the finite element mesh through a cross-section.

Analogously to Eq. 51, the load generated by a stress field over a slice of a planar cross section is defined by the following integral:

$$P = \int_0^t \int_{x_i}^{x_i + \Delta x} \sigma \quad x, y \quad \cdot dx \cdot dy \qquad (60)$$

Once again, assuming that the change in stress over the slice in the x direction is small, and taking a slice of unit thickness, the double integral may be reduced to a single integral:

$$P = \int_0^t \sigma(y) \cdot dy \qquad (61)$$

By substituting a linear distribution for the stresses between nodes and integrating, the expression simplifies to the following:

$$P_i = \left(\frac{\sigma_i + \sigma_{i+1}}{2} \right) \left| y_i - y_{i+1} \right| \qquad (62)$$

This term is then summed up over all of the elements in the cross-section to return the total load value. For the four-element finite element meshes used in the coarse model, this returns the following expression:

$$P = \sum_{i=1}^{5} \left(\frac{\sigma_i + \sigma_{i+1}}{2} \right) \left| y_i - y_{i+1} \right| \qquad (63)$$

The load at this point may now be entered into Eq.50, and the membrane stress may be found.

4.4 Validation of the Coarse 3D Finite Element Mesh

The validation of the membrane and bending stresses generated using the coarse-mesh finite element data was carried out for a variety of different geometries. These were mostly taken from standard John Deere test geometries. The geometries studied are listed below:

- T-Joint under In-Plane Bending
- T-Joint under Out-of-Plane Bending
- Circular Tube on Plate under Bending
- Circular Tube on Plate under Tension

Each of these geometries were analyzed using data provided from the John Deere company. The coarse mesh data, post processed as outlined in this Section, consistently returned peak stress values close to the peak stress indicated by the finely meshed finite element models.

The validation process extended to determining that the total moment predicted to be acting on the cross-section in the fine mesh case was approximately equal to ten times the moment generated by the inboard part of the coarsely-mesh cross-section. A margin of error of +/-10 % is allowed for.

4.4.1 In-Plane Bending Welded T-Joint Analysis

The first welded connection that will be analyzed is the T-joint. For this geometry, the stress distribution in the region of interest will be found using a coarse mesh only 4 elements thick. This stress distribution will then be compared to the stress distribution generated using a finely-meshed model. It is expected that the stress distributions for the two meshes should align over the inboard 50% of the cross section.

It is also expected that the moment generated by the stress distribution over the inboard 50% of the cross section will account for 10% of the total moment. The total moment can therefore be found

using only the stress distribution of the inboard 50% of the cross-section. Once this total moment is known, both the hotspot and peak stresses can be found, and finally the fatigue life of a weldment may be determined.

The joint was assumed to be made of a typical structural steel, and was analyzed given a geometry provided by Rakesh Goyal at John Deere. The geometry was meshed using hexagonal elements, with the mesh density being higher in the areas of interest. The area of interest in this case was the cross-section running through the base plate below the weld toe line. The fine mesh data used for comparison in the following analyses was also provided by the Rakesh Goyal [24].

4.4.1.1 Material Properties

The material assumed for this trial was standard structural steel. This matched the earlier work done by Rakesh Goyal of John Deere, making comparisons of the results easier.

The material was assumed to have a Young's Modulus of 200 GPa and a Poisson's Ratio of 0.3. It was also assumed to behave in a perfectly elastic manner. This is a reasonable assumption to make, as most design cases limit their applied stress values to the elastic regime.

4.4.1.2 Geometry of T-Joint

The geometry of the T-Joint is shown in the following figure:

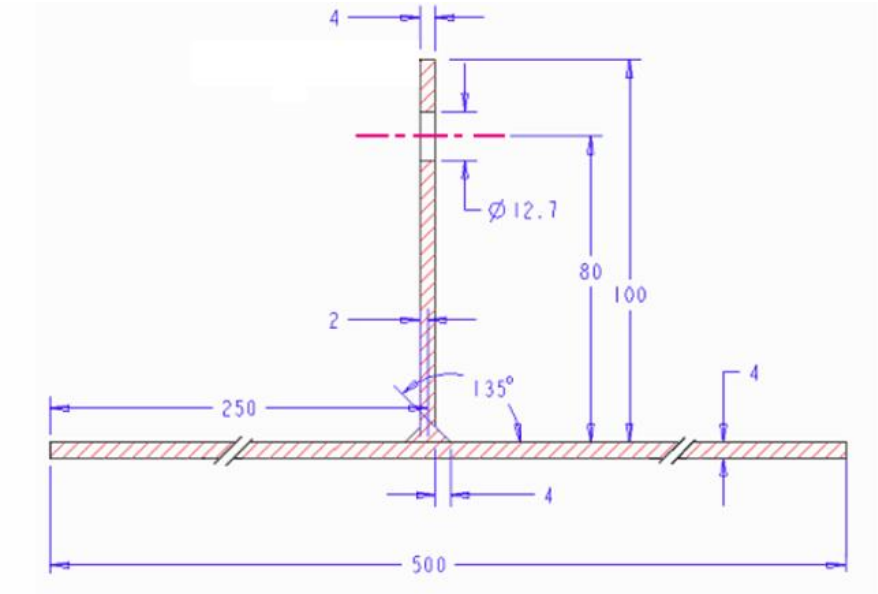

Figure 18. Geometry of the T-Joint [24].

The base plate has dimensions of 500 mm x 500 mm x 4 mm, and the vertical plate has a depth of 50 mm. The original geometry is shown in Figure 16.

In order to minimize the computational complexity of the problem, the geometry was cut along the axis of symmetry of the loading case. The resulting geometry is shown in Figure 17.

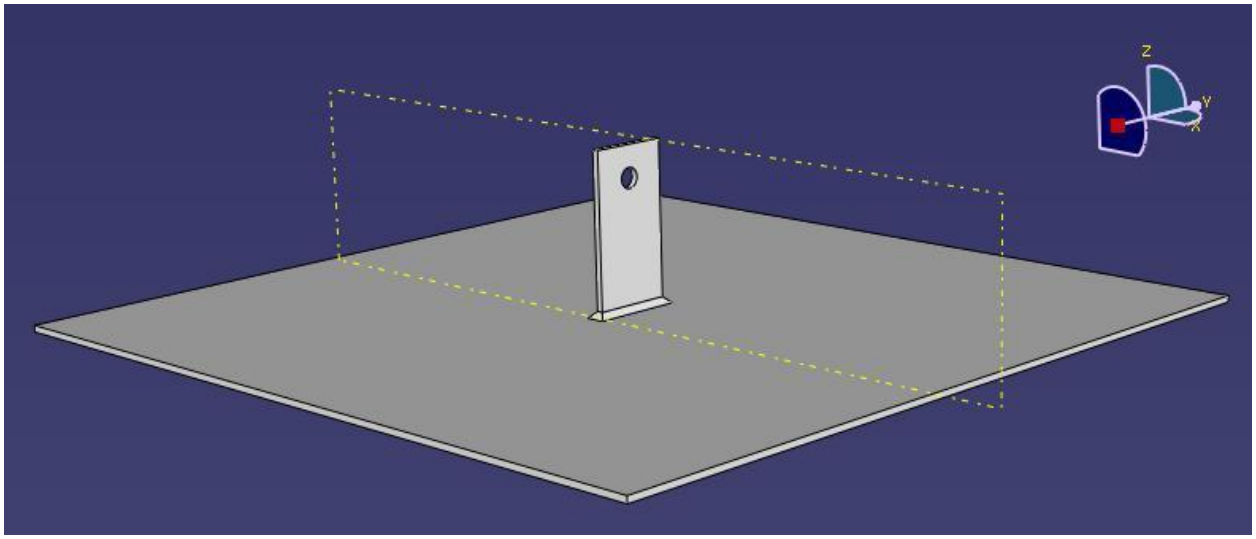

Figure 19. Model of the complete T-Joint geometry.

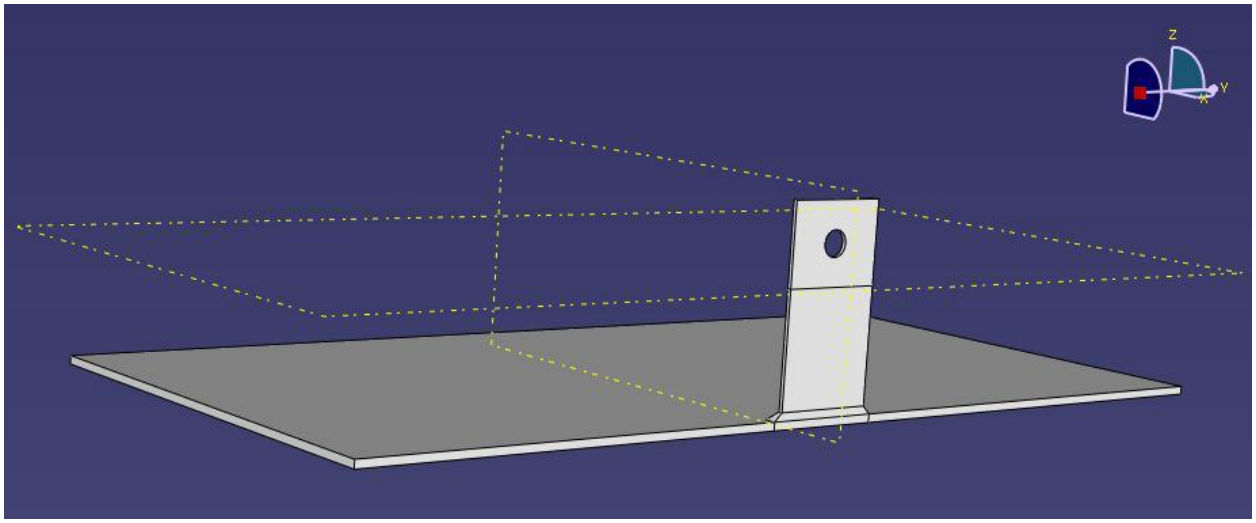

Figure 20. Model of the T-Joint geometry cut along its axis of symmetry

Loads and boundary conditions were then applied to the model.

Boundary conditions consisted of pinned constraints at the two corners of the base plate furthest from the vertical plate, and an x-symmetry condition along the entire cut face. The x-symmetry condition constrains the geometry from displacing in the x-direction, and from rotating about the y- and z-axes. The applied boundary conditions are shown in the following figures.

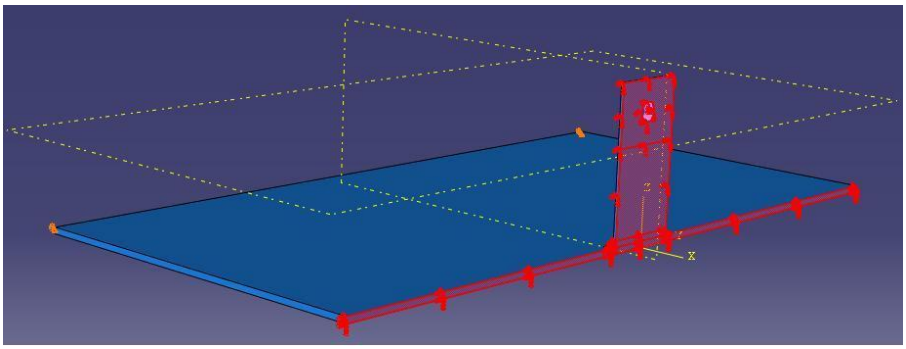

Figure 21. Area subjected to x-symmetry boundary condition highlighted in red.

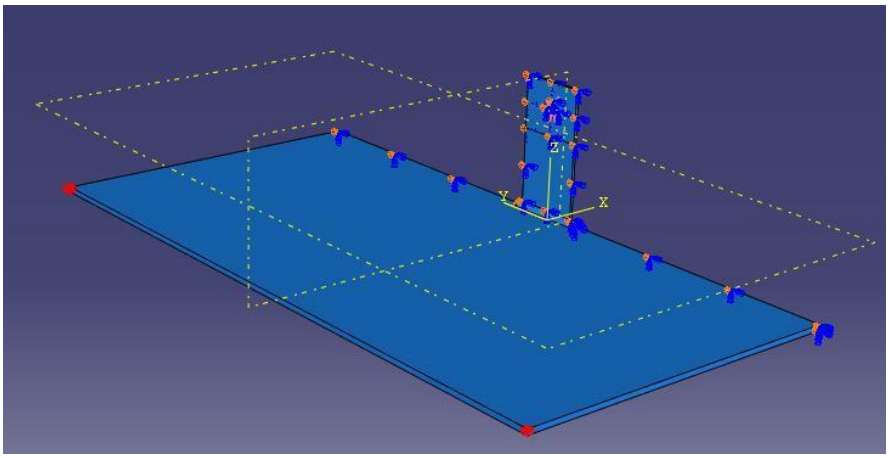

Figure 22. Points subjected to pinned boundary condition highlighted in red.

The load applied to this case was a concentrated load applied as shown in the following figure. A load of 500 N was applied to the region shown in the image below.

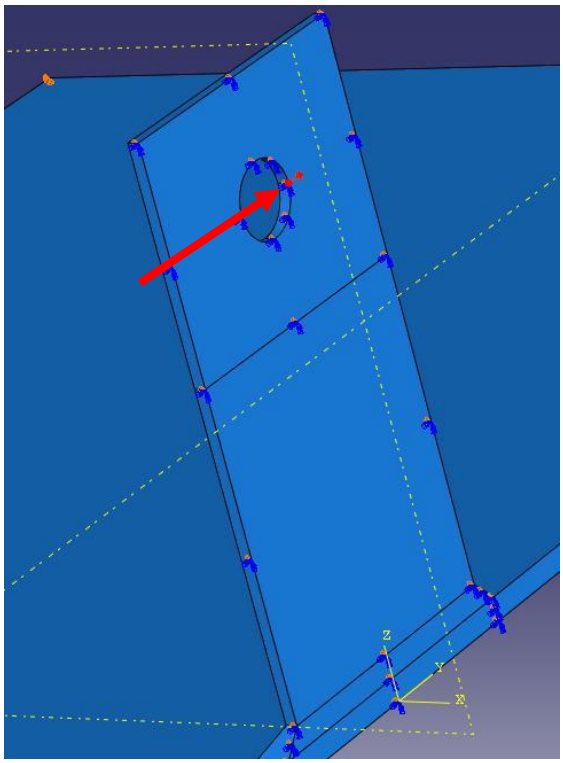

Figure 23. Point of application and direction of load marked by red arrow.

4.4.1.3 Meshing of the T-Joint

The geometry was meshed entirely using hexagonal quadratic elements. Structured meshes were used wherever possible, but regions with more complicated geometries were meshed using swept meshing techniques. For the swept meshes, mapped meshing techniques were used where appropriate.

The sections of the geometry meshed using swept, advancing front meshing techniques are shown below in yellow, while the sections of the geometry that were used using structured meshes are highlighted in green in the following figure. Once again, all of the elements used were quadratic in nature.

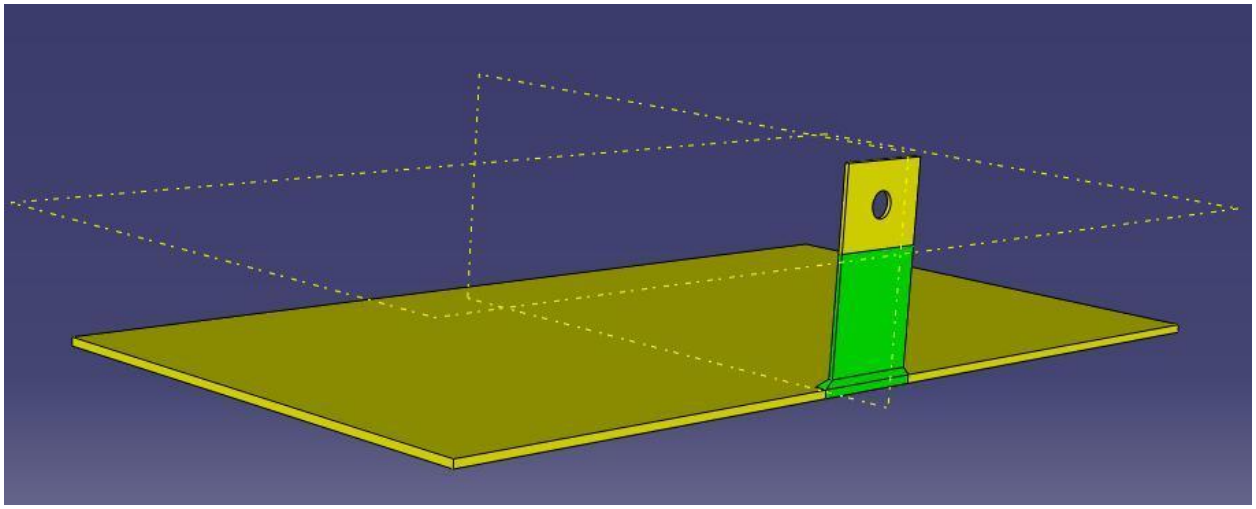

Figure 24. Types of meshing techniques used during the analysis.

The primary region of interest in this case was the cross-section through the base-plate underneath the weld toe line. There are two weld toe lines of interest in the T-joint geometry, and they are highlighted in the following figure. The cross-section below either one of these lines may be used for analysis.

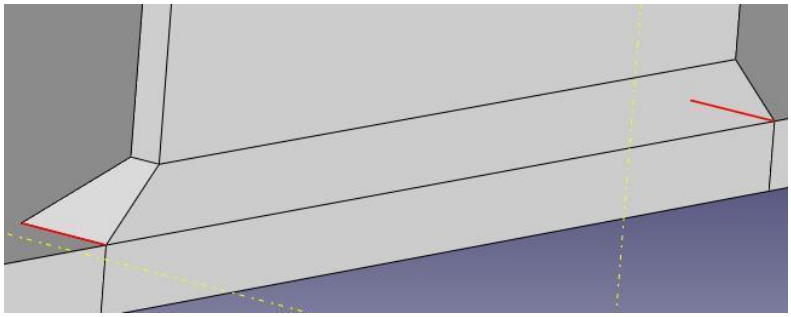

Figure 25. Weld toe lines of interest.

Regions close to the area of interest were meshed relatively finely, with an effort being made to ensure all of the elements were as close to cubic as possible. Further away from the area of interest, coarser meshes were used to minimize the computational intensity. The resulting mesh is shown in the following figures.

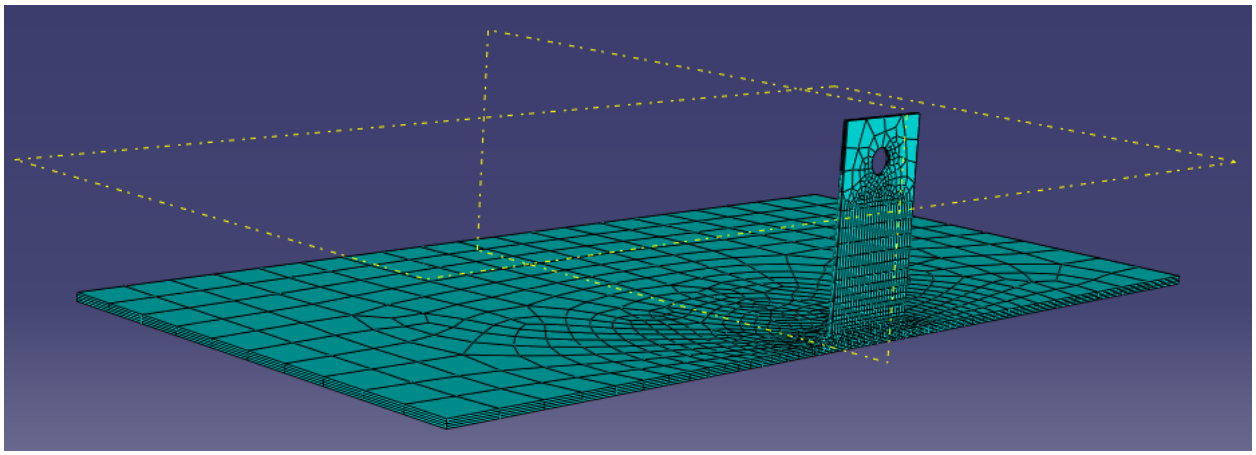

Figure 26. Global overview of the mesh used for a T-Joint under In-Plane Bending.

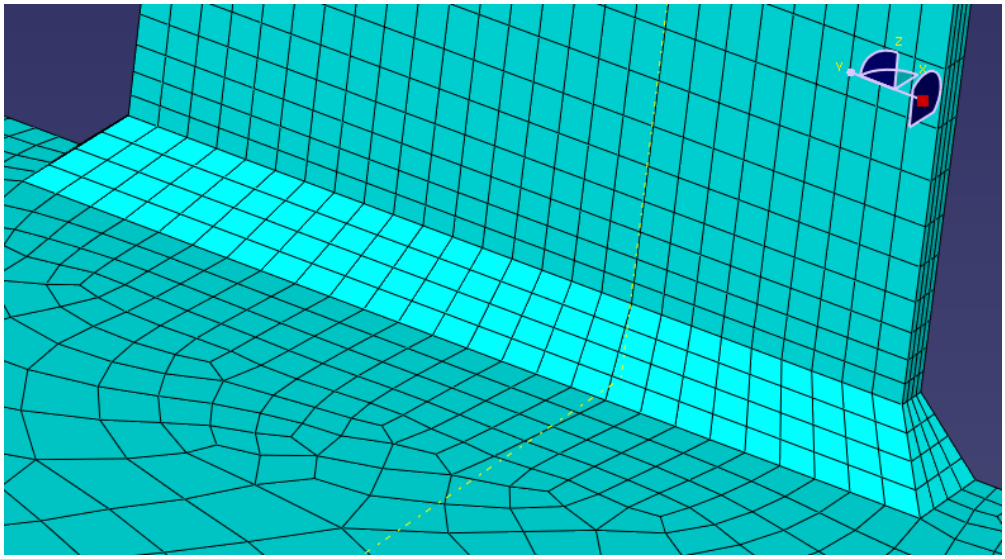

Figure 27. Mesh in the weld area for a T-Joint under In-Plane Bending.

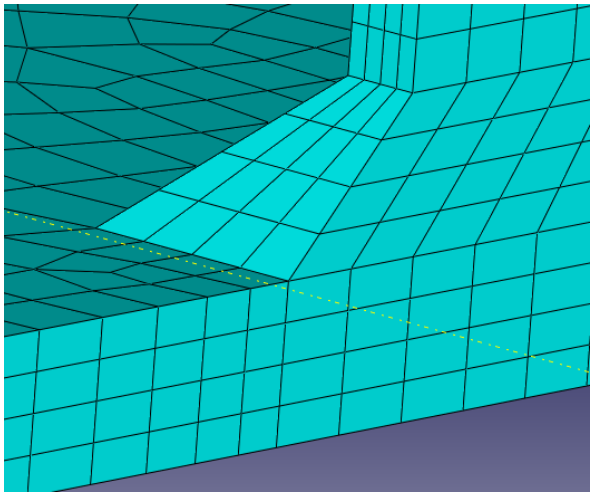

Figure 28. Mesh in the area of interest for a T-Joint under In-Plane Bending.

The stress distributions generated by the above meshes using quadratic elements were found to give sufficiently accurate stress readings in the inboard 50% of the cross section of the base plate directly underneath the weld toe line.

4.4.1.4 Three-Dimensional Coarse Mesh Stress Distribution in the T-Joint

The stress distribution generated by the above mesh is shown in the following figure.

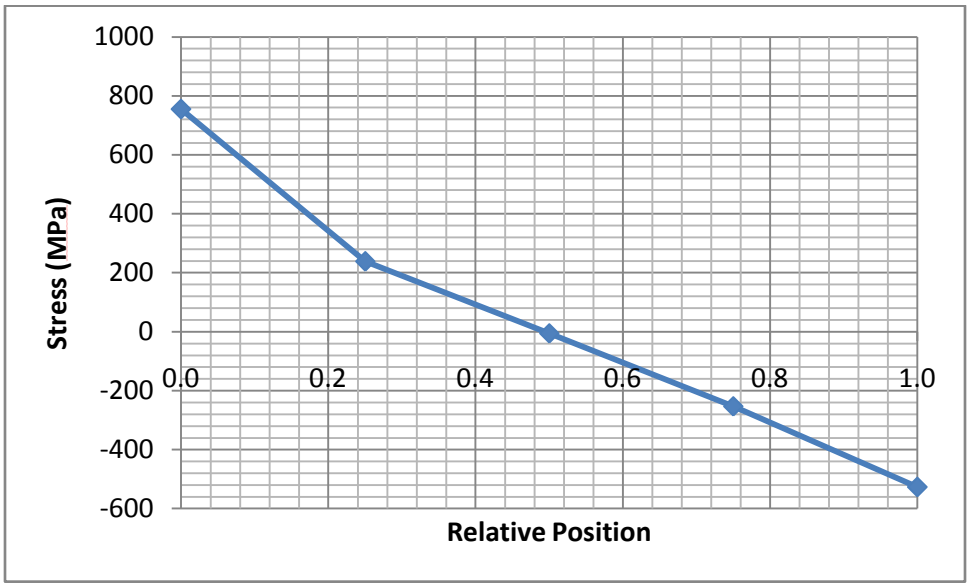

Figure 29. Coarse mesh stress distribution for a T-Joint under in-plane bending.

The coarse mesh distribution is expected to coincide with the fine mesh stress distribution of the cross section from the 0.25 to 0.75 relative position marks. This will be verified in the following section, where the coarse and fine mesh stress distributions for this cross section will be overlaid.

4.4.1.5 Three-Dimensional Fine Mesh Stress Distribution in the T-Joint

In order to assess the accuracy of the stress distribution generated by the coarse mesh, the stress distribution generated by a finely-meshed model of the T-joint was to create a comparison. The finely-meshed data used in this case was produced by Rakesh Goyal, of John Deere. The geometry used was identical to the one shown in section 4.4.1.2, except that a radius of 0.55 mm was applied to the edges of the fillet weld.

The fine mesh stress distribution is shown in the following figure.

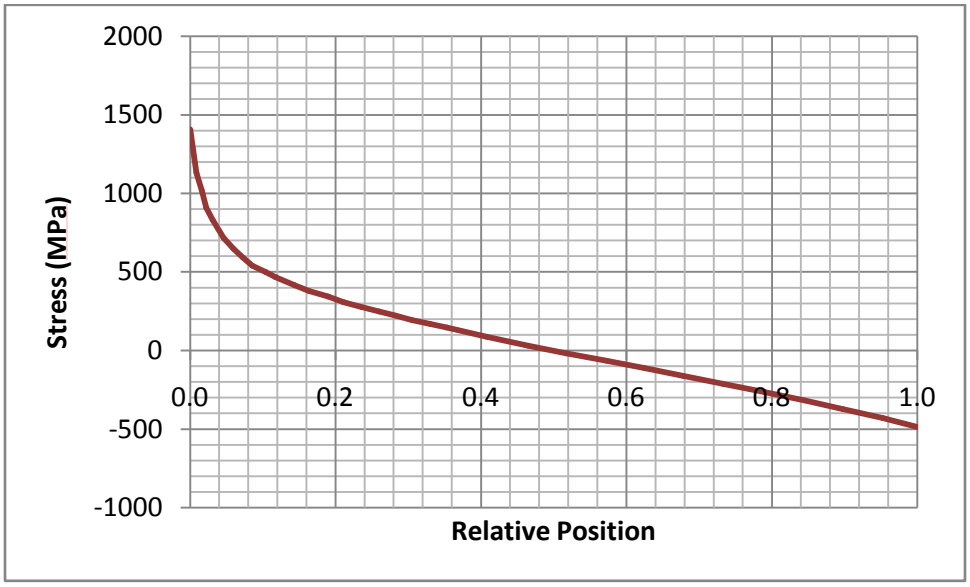

Figure 30. Fine mesh stress distribution for a T-Joint under in-plane bending [24].

The coarse and fine mesh distributions can now be overlaid to verify if the two distributions match over the domain of relative positions from 0.25 to 0.75. This is shown in the following figure.

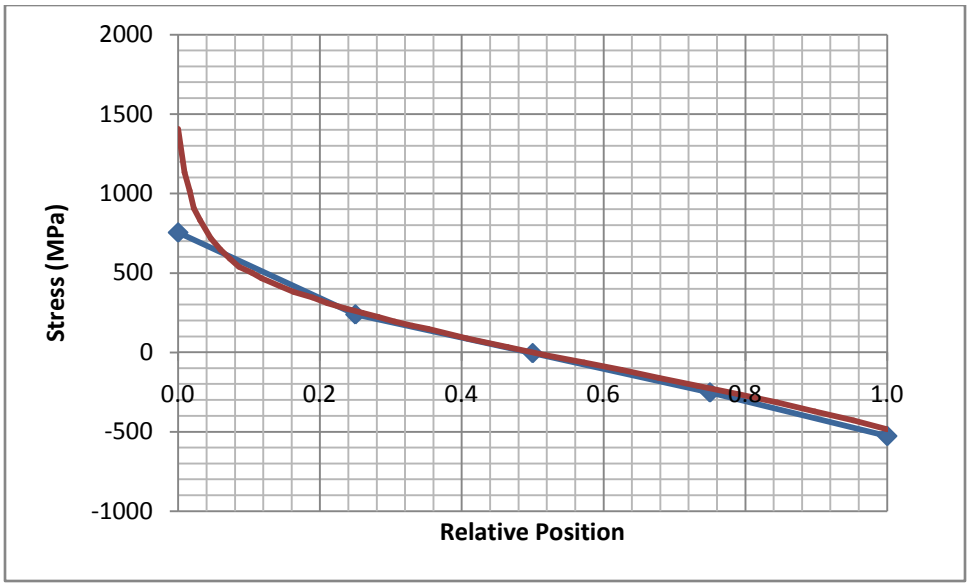

Figure 31. Overlay of coarse and fine mesh stress distributions for a T-Joint under in-plane bending.

.

It can be seen that the two distributions do match up over the inboard 50% of the cross-section. It can therefore be said that the coarse mesh data for the stress distribution is valid for the interior half of the cross-section. It will now be shown that the data from the interior of the cross-section may be manipulated to generate maximum stress values.

4.4.1.6 Ratio of Inboard and Total Bending Moments

It is expected that the ratio between the inboard and total bending moments be 0.1. This relationship has been found to hold for a variety of loading conditions and geometries.

In this case, the total moment acting in the finely-meshed case was found to be 97.48 Nm. The moment generated by the inboard 50% of the coarse-mesh stress distribution was found to be 10.23 Nm. The ratio between these two values is therefore 0.10, confirming the prediction.

4.4.2 Out-of-Plane Bending Welded T-Joint Analysis

The second welded connection that will be analyzed is the T-joint, but this time with the bending in the out-of-plane direction. For this geometry, the stress distribution in the region of interest will be found using a coarse mesh only 4 elements thick. This stress distribution will then be compared to the stress distribution generated using a finely-meshed model. It is expected that the stress distributions for the two meshes should align over the inboard 50% of the cross section.

It is also expected that the moment generated by the stress distribution over the inboard 50% of the cross section will account for 10% of the total moment. The total moment can therefore be found

using only the stress distribution of the inboard 50% of the cross-section. Once this total moment is known, both the hotspot and peak stresses can be found, and finally the fatigue life of a weldment may be determined.

The joint was assumed to be made of a typical structural steel, and was analyzed given a geometry provided by Rakesh Goyal at John Deere. The geometry was meshed using hexagonal elements, with the mesh density being higher in the areas of interest. The area of interest in this case was the cross-section running through the attached plate below the weld toe line.

4.4.2.1 Material Properties

The material assumed for this trial was standard structural steel. This matched the earlier work done by Rakesh Goyal of John Deere, making comparisons of the results easier.

The material was assumed to have a Young's Modulus of 200 GPa and a Poisson's Ratio of 0.3. It was also assumed to behave in a perfectly elastic manner. This is a reasonable assumption to make, as most design cases limit their applied stress values to the elastic regime.

4.4.2.2 Geometry of T-Joint

The geometry of the T-Joint is shown in the following figure:

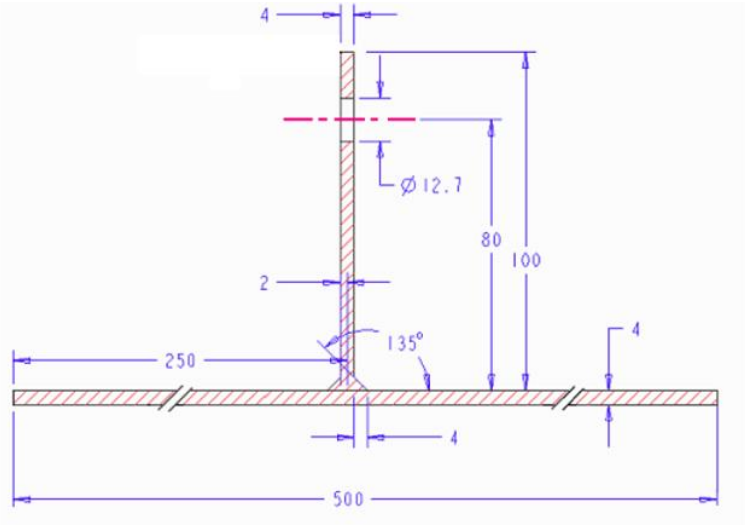

Figure 32. Geometry of the T-Joint [24]

The base plate has dimensions of 500 mm x 500 mm x 4 mm, and the vertical plate has a depth of 50 mm. The original geometry is shown in Figure 30.

In order to minimize the computational complexity of the problem, the geometry was cut along the axis of symmetry of the loading case. The resulting geometry is shown in Figure 31.

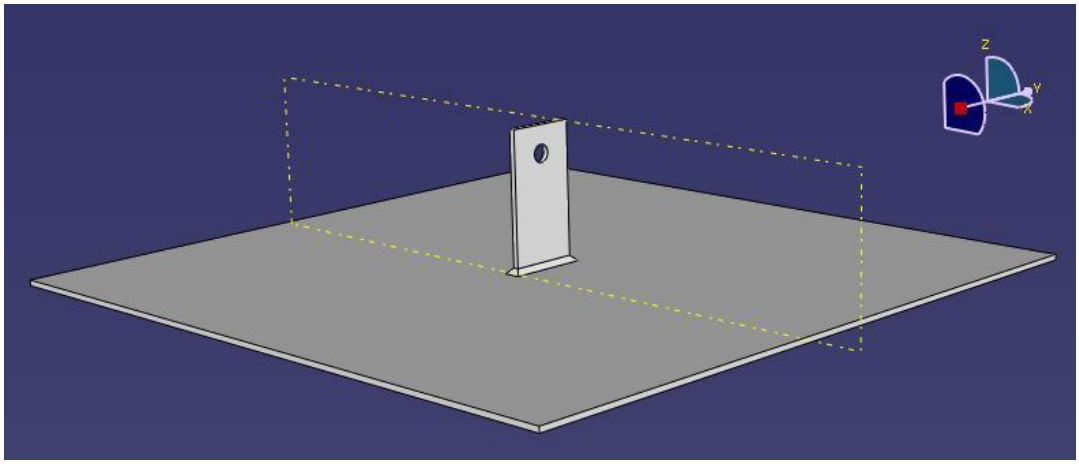

Figure 33. Model of the complete geometry of the T-Joint

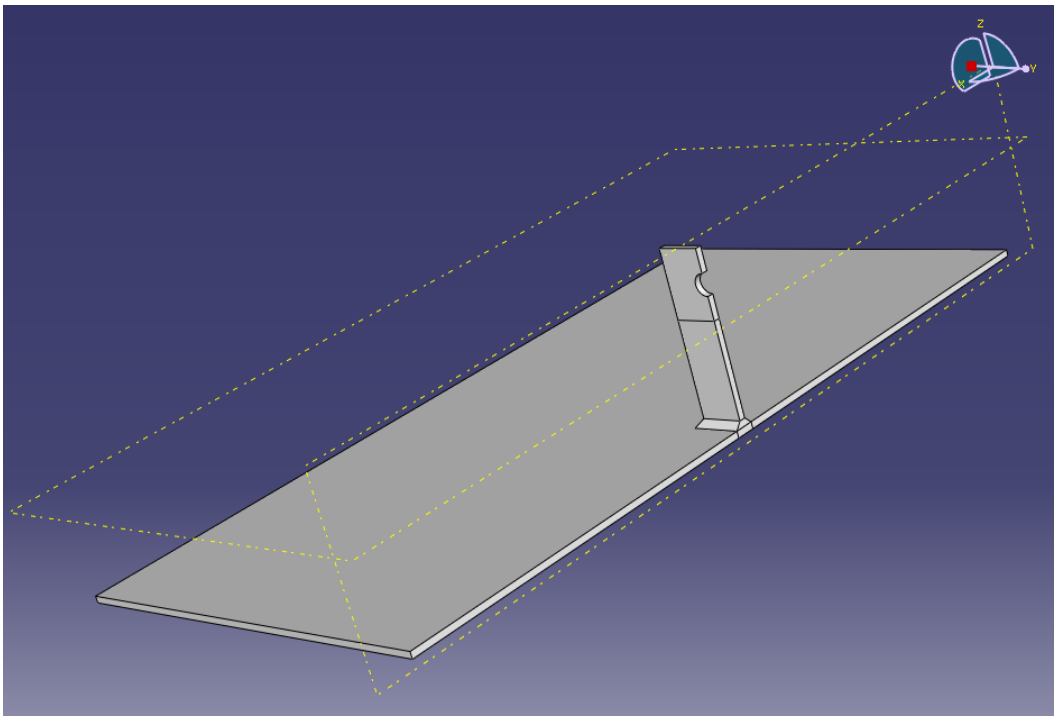

Figure 34. Model of the T-Joint geometry cut along its axis of symmetry

Loads and boundary conditions were then applied to the model.

Boundary conditions consisted of pinned constraints at the two corners of the base plate furthest from the vertical plate, and a y-symmetry condition along the entire cut face. The y-symmetry condition constrains the geometry from displacing in the y-direction, and from rotating about the x- and z-axes. The applied boundary conditions are shown in the following figures.

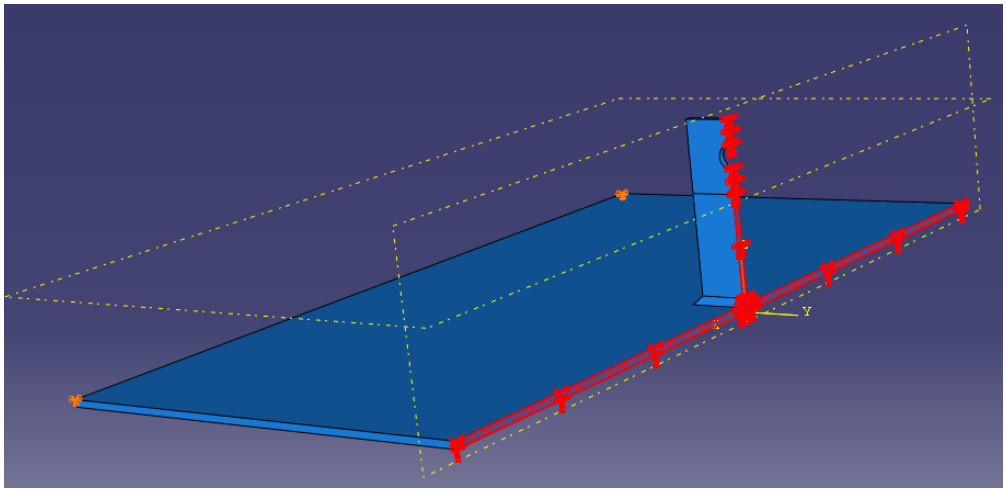

Figure 35. Area subjected to y-symmetry boundary condition highlighted in red.

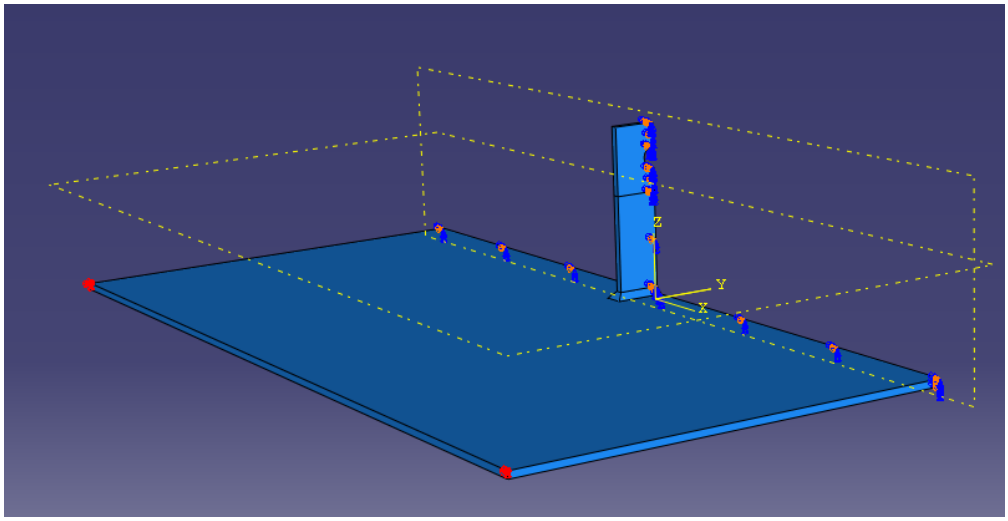

Figure 36. Points subjected to pinned boundary condition highlighted in red.

The load applied to this case was a surface traction applied as shown in the following figure. A resulting load of 500 N was applied to the region shown in the image below.

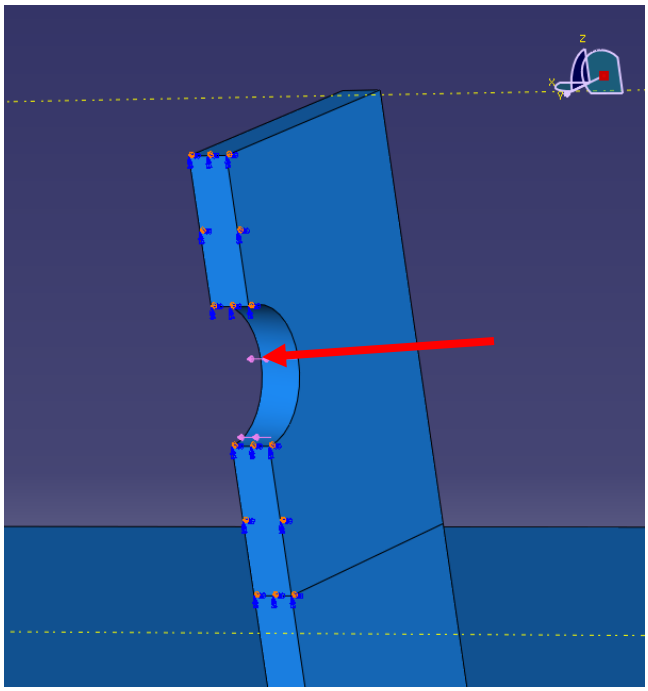

Figure 37. Point of application and direction of load marked by red arrow.

4.4.2.3 Meshing of the T-Joint

The geometry was meshed entirely using hexagonal quadratic elements. Structured meshes were used wherever possible, but regions with more complicated geometries were meshed using swept meshing techniques. For the swept meshes, mapped meshing techniques were used where appropriate.

The sections of the geometry meshed using swept, advancing front meshing techniques are shown below in yellow, while the sections of the geometry that were used using structured meshes are highlighted in green in the following figure. Once again, all of the elements used were quadratic in nature.

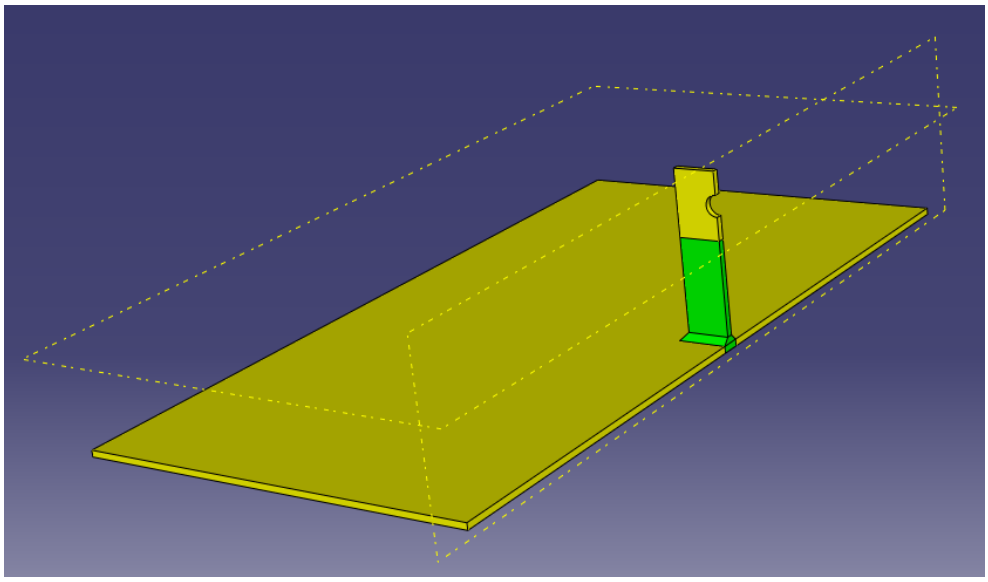

Figure 38. Types of meshing techniques used during the analysis.

The primary region of interest in this case was the cross-section through the base-plate underneath the weld toe line. There are two weld toe lines of interest in the T-joint geometry, and they are highlighted in the following figure. The cross-section below either one of these lines may be used for analysis.

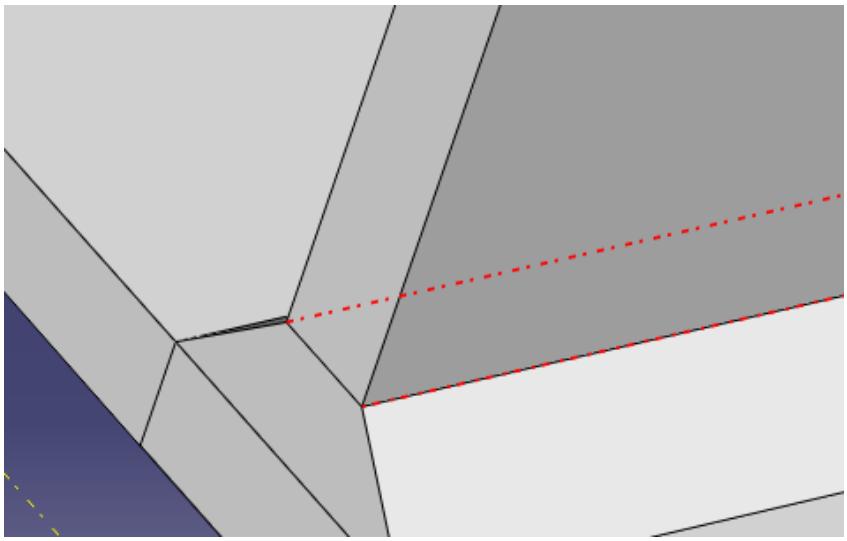

Figure 39. Weld toe lines of interest.

Regions close to the area of interest were meshed relatively finely, with an effort being made to ensure all of the elements were as close to cubic as possible. Further away from the area of interest, coarser meshes were used to minimize the computational intensity. The resulting mesh is shown in the following figures.

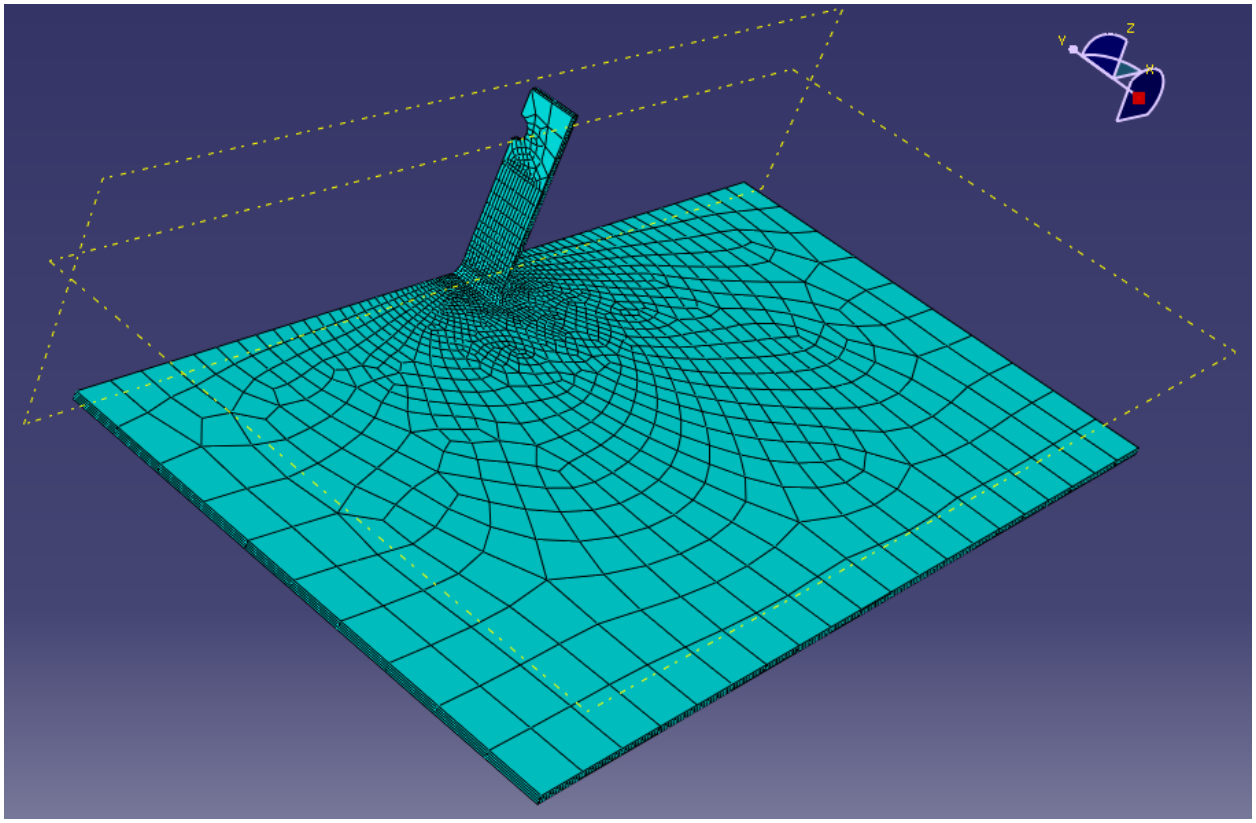

Figure 40. Global overview of the mesh used for a T-joint in out-of-plane bending.

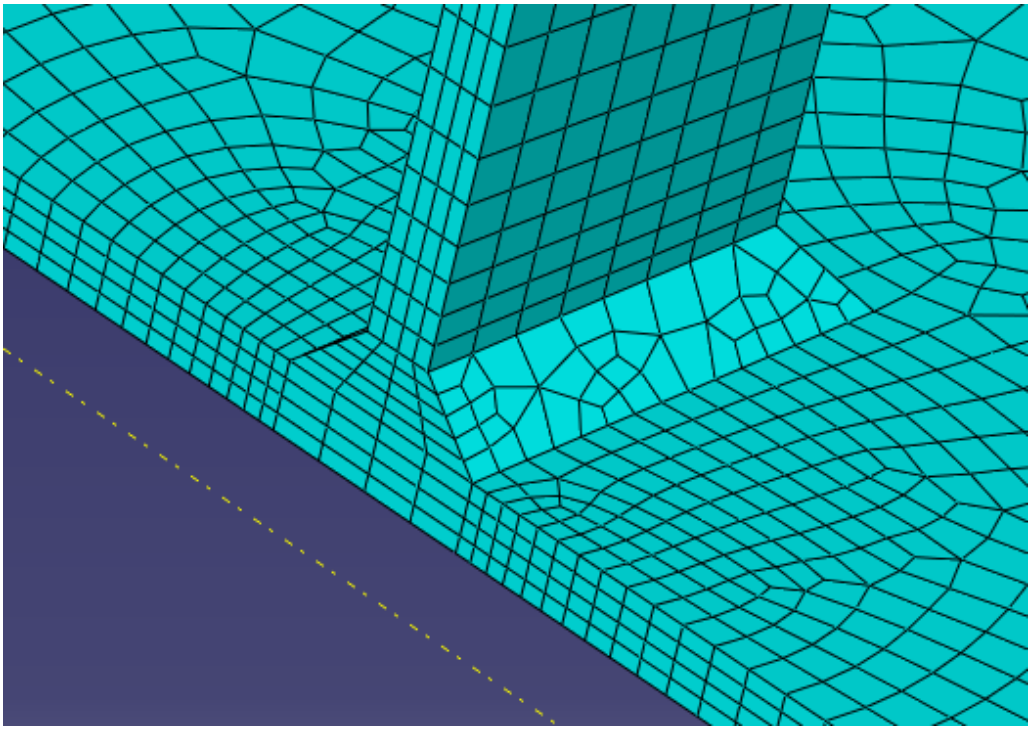

Figure 41. Mesh in the weld area for a T-joint in out-of-plane bending.

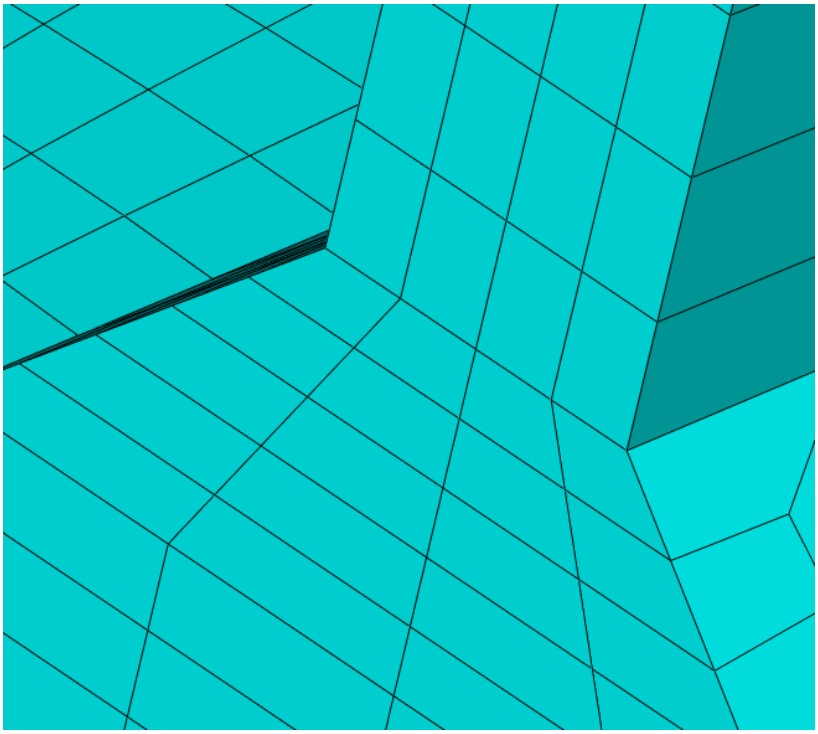

Figure 42. Mesh in the area of interest for a T-joint in out-of-plane bending.

The stress distributions generated by the above meshes using quadratic elements were found to give sufficiently accurate stress readings in the inboard 50% of the cross section of the base plate directly underneath the weld toe line.

4.4.2.4 Three-Dimensional Coarse Mesh Stress Distribution in the T-Joint

The stress distribution generated by the above mesh is shown in Fig.43.

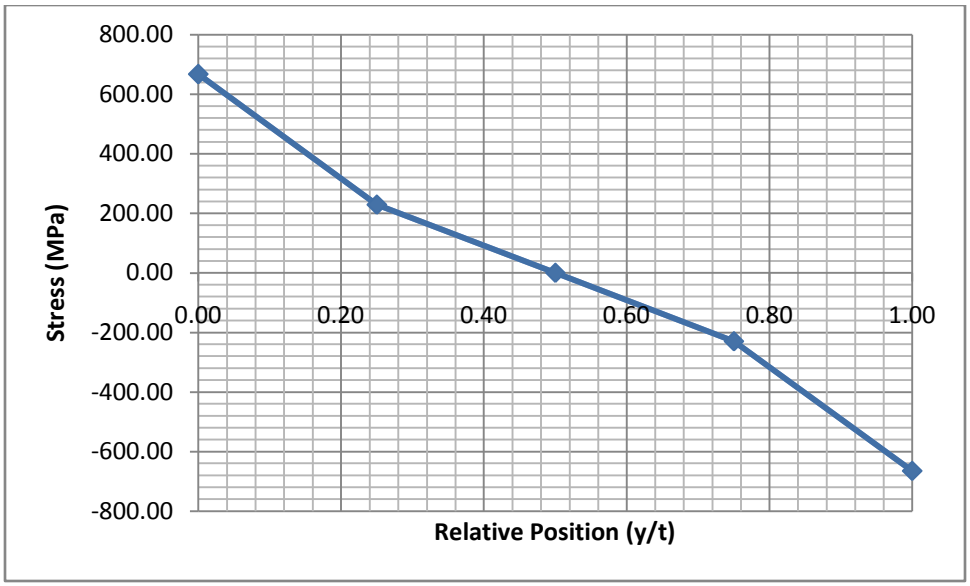

Figure 43. T-Joint coarse mesh stress distribution.

The coarse mesh distribution is expected to coincide with the fine mesh stress distribution of the cross section from the 0.25 to 0.75 relative position marks. This will be verified in the following section, where the coarse and fine mesh stress distributions for this cross section will be overlaid.

4.4.2.5 Three-Dimensional Fine Mesh Stress Distribution in the T-Joint

In order to assess the accuracy of the stress distribution generated by the coarse mesh, the stress distribution generated by a finely-meshed model of the T-joint was to create a comparison. The finely-meshed data used in this case was produced by Rakesh Goyal, of John Deere. The geometry used was identical to the one shown in section 4.4.2.2, except that a radius of 0.55 mm was applied to the edges of the fillet weld.

The fine mesh stress distribution is shown in Fig.44.

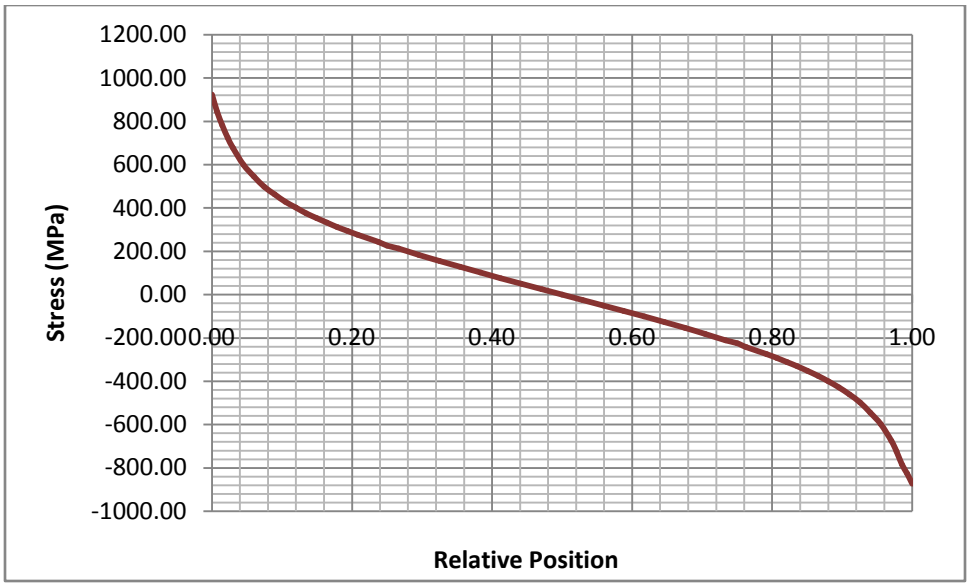

Figure 44. T-Joint fine mesh stress distribution [24].

The coarse and fine mesh distributions can now be overlaid to verify if the two distributions match over the domain of relative positions from 0.25 to 0.75. This is shown in the following figure.

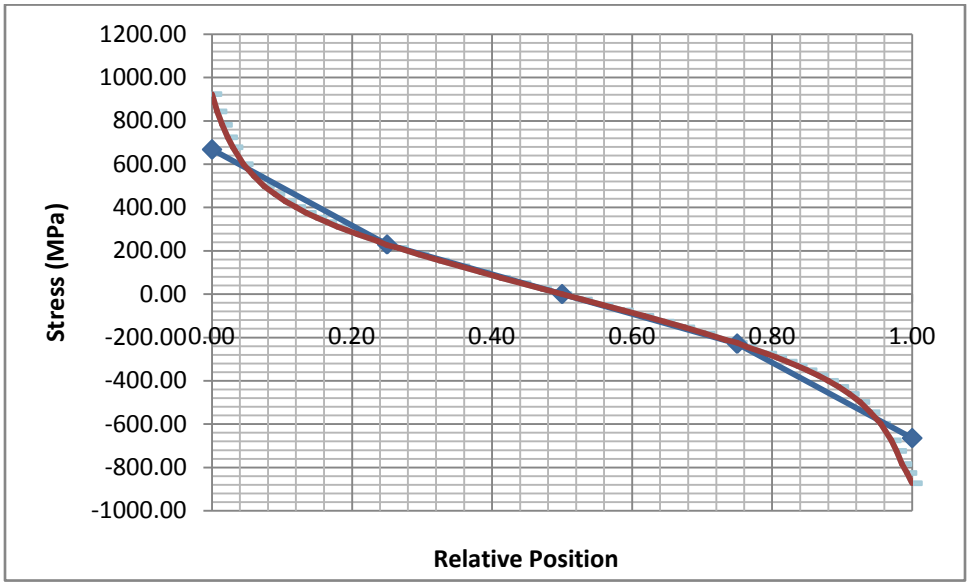

Figure 45. Overlay of coarse and fine mesh stress distributions for the T-Joint.

It can be seen that the two distributions do match up over the inboard 50% of the cross-section. It can therefore be said that the coarse mesh data for the stress distribution is valid for the interior half of the cross-section. It will now be shown that the data from the interior of the cross-section may be manipulated to generate maximum stress values.

4.4.2.6 Ratio of Inboard and Total Bending Moments

It is expected that the ratio between the inboard and total bending moments be 0.1. This relationship has been found to hold for a variety of loading conditions and geometries.

In this case, the total moment acting in the finely-meshed case was found to be 97.15 Nm. The moment generated by the inboard 50% of the coarse-mesh stress distribution was found to be 9.56 Nm. The ratio between these two values is therefore 0.10, confirming the prediction.

4.4.3 Circular Tube on Plate Under Bending

The third welded connection that will be analyzed is the circular tube on a plate. For this geometry, the stress distribution in the region of interest will be found using a coarse mesh only 4 elements thick. This stress distribution will then be compared to the stress distribution generated using a finely-meshed model. It is expected that the stress distributions for the two meshes should align over the inboard 50% of the cross section.

It is also expected that the moment generated by the stress distribution over the inboard 50% of the cross section will account for 10% of the total moment. The total moment can therefore be found using only the stress distribution of the inboard 50% of the cross-section. Once this total moment is known, both the hotspot and peak stresses can be found, and finally the fatigue life of a weldment may be determined.

The joint was assumed to be made of a typical structural steel, and was analyzed given a geometry provided by Rakesh Goyal at John Deere. The geometry was meshed using hexagonal elements, with the mesh density being higher in the areas of interest. The area of interest in this case was the cross-section running through the base plate below the weld toe line.

4.4.3.1 Material Properties

The material assumed for this trial was standard structural steel. This matched the earlier work done by Rakesh Goyal of John Deere, making comparisons of the results easier.

The material was assumed to have a Young's Modulus of 200 GPa and a Poisson's Ratio of 0.3. It was also assumed to behave in a perfectly elastic manner. This is a reasonable assumption to make, as most design cases limit their applied stress values to the elastic regime.

4.4.3.2 Geometry of Circular Tube on Plate

The geometry and loading of the cylindrical tube on the plate is shown in Fig.46.

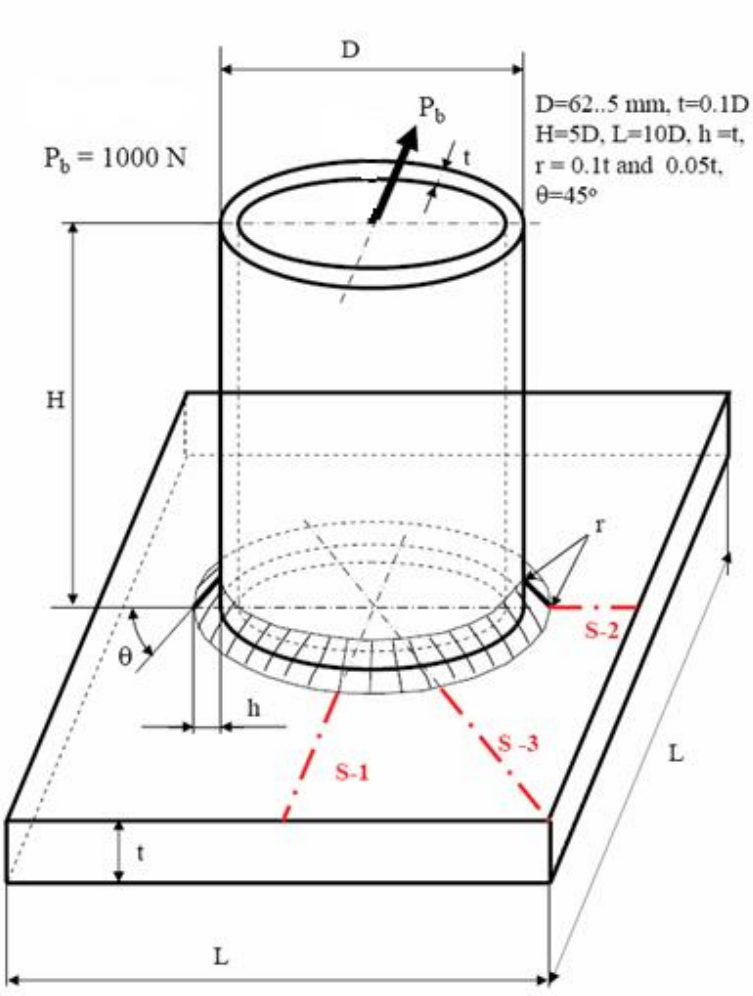

Figure 46. Circular Tube on Plate [24].

The base plate has dimensions of 625 mm x 625 mm x 6.25 mm, and the cylinder has a height of 312.5 mm. The weld toe radius is 0.3125 mm. The angle of the weld is 45°, with a height of 6.25 mm. Finally, the diameter of the tube is 62.5 mm.

In order to minimize the computational complexity of the problem, the geometry was cut along the axis of symmetry of the loading case. The resulting geometry is shown in the following figure.

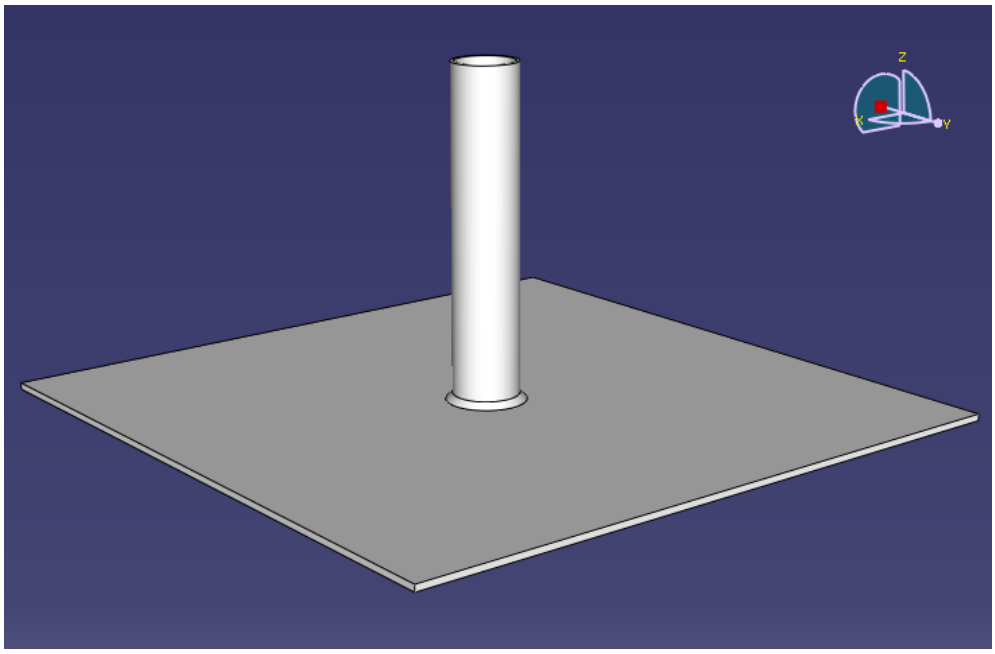

Figure 47. Circular Tube on Plate Full Model.

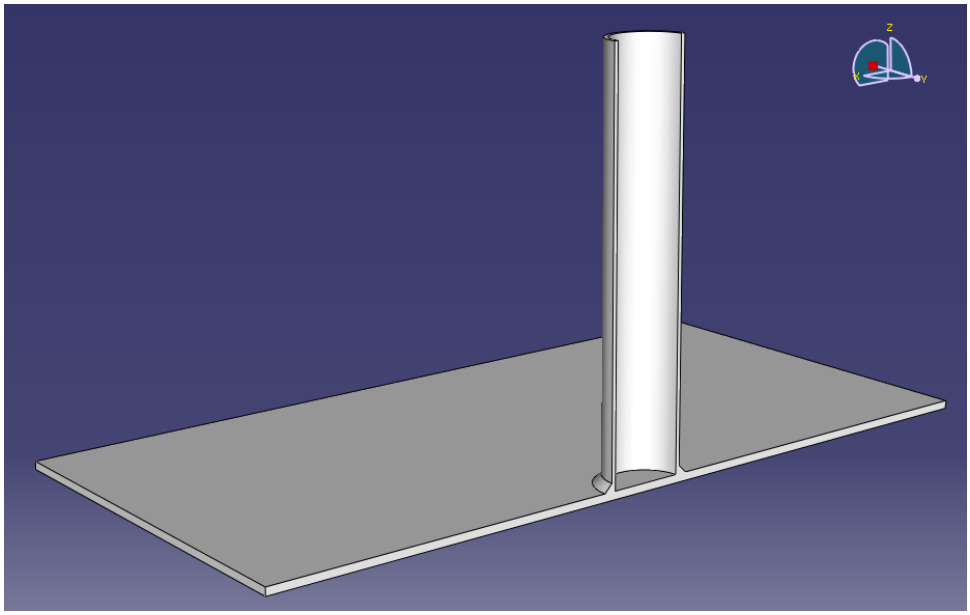

Figure 48. Model of the T-Joint geometry cut along its axis of symmetry

Loads and boundary conditions were then applied to the model.

Boundary conditions consisted of pinned constraints at the two corners of the base plate furthest from the vertical plate, and an x-symmetry condition along the entire cut face. The x-symmetry

condition constrains the geometry from displacing in the y-direction, and from rotating about the x- and z-axes. The applied boundary conditions are shown in the following figures.

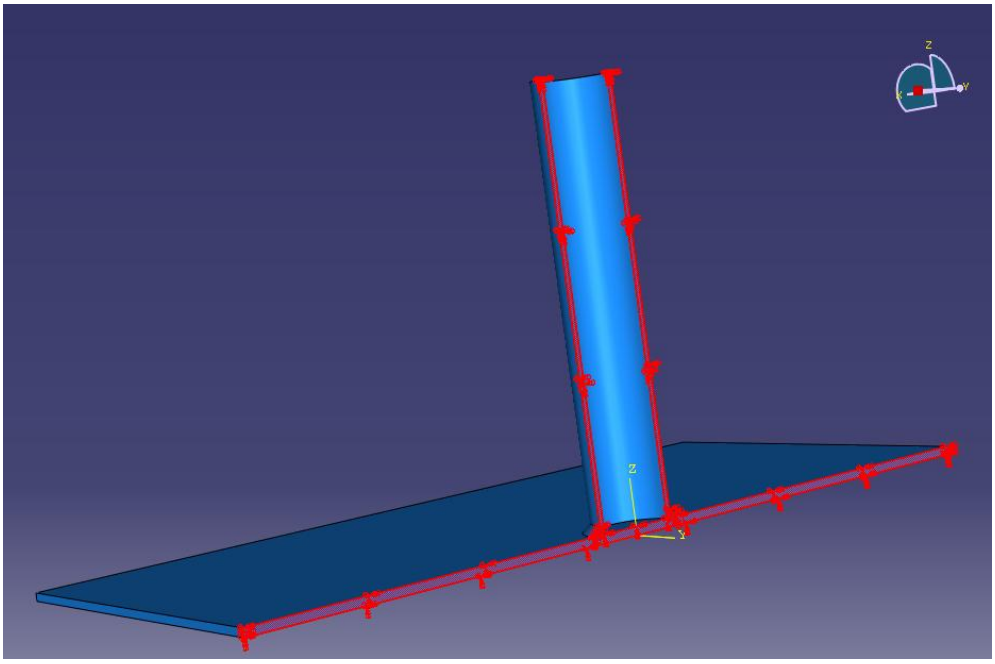

Figure 49. Area subjected to y-symmetry boundary condition highlighted in red.

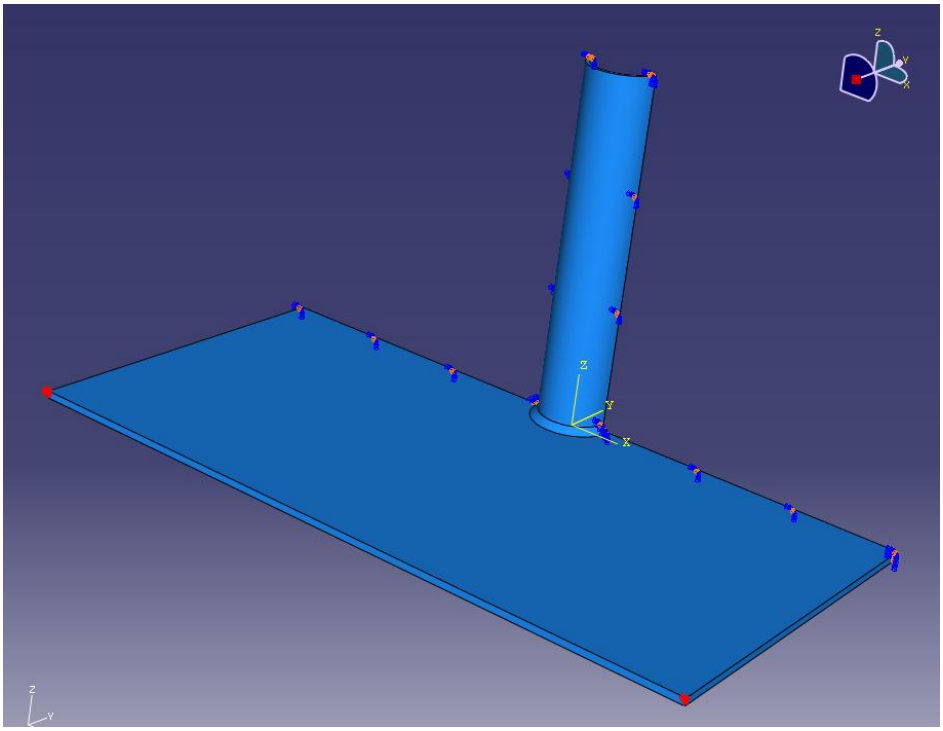

Figure 50. Points subjected to pinned boundary condition highlighted in red.

The load applied to this case was a surface traction applied as shown in the following figure. A load of 500 N was generated by applying a surface traction over the upper rim area of the tube. The magnitude of the applied surface traction was 1.71 MPa.

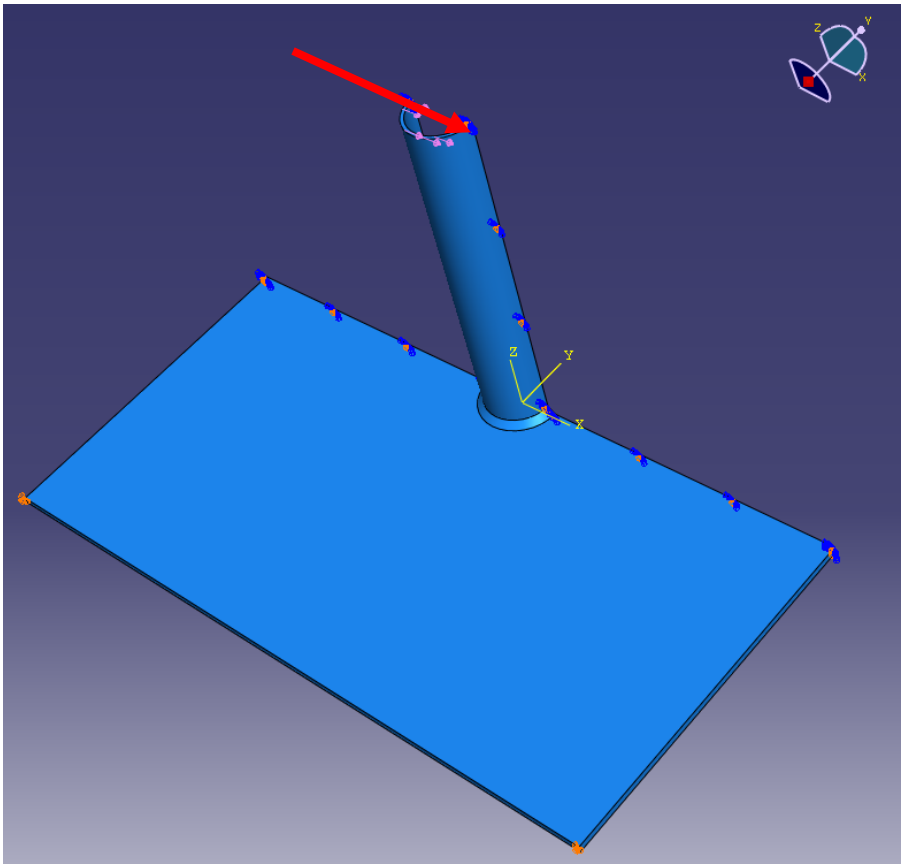

Figure 51. Point of application and direction of load marked by red arrow.

4.4.3.3 Meshing of the T-Joint

The geometry was meshed entirely using hexagonal quadratic elements. Structured meshes were used wherever possible, but regions with more complicated geometries were meshed using swept meshing techniques. For the swept meshes, mapped meshing techniques were used where appropriate.

The sections of the geometry meshed using swept advancing front meshing techniques are shown below in yellow, and the regions meshed using a structured mesh are shown in green. Advancing front meshing was used in the base plate, and structured meshing in the tube and weld.

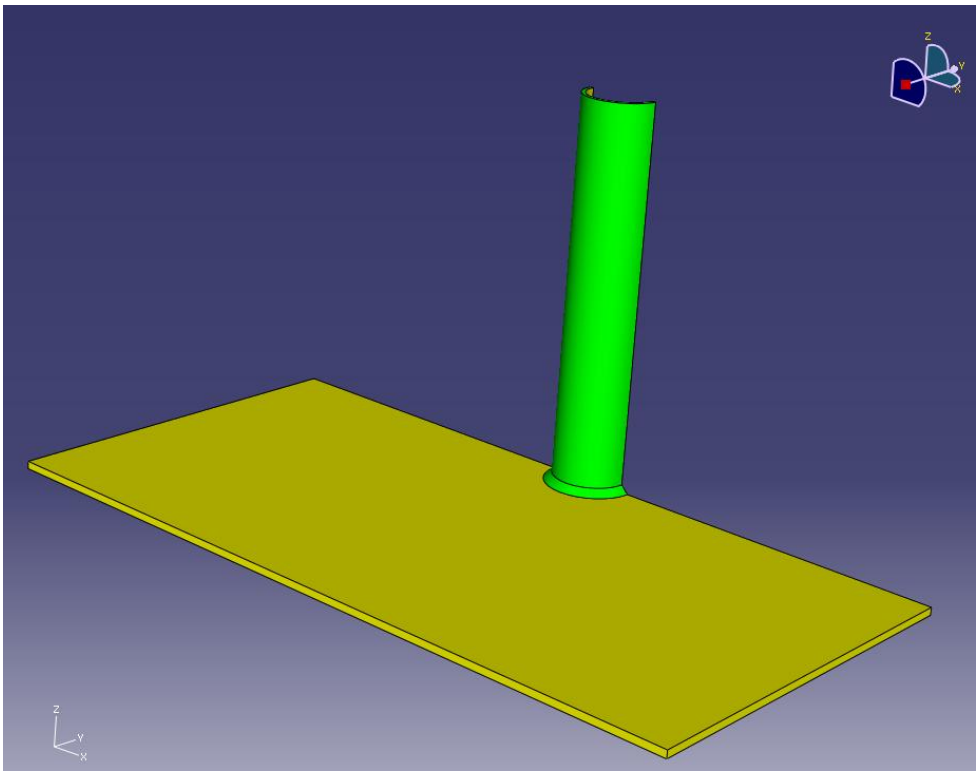

Figure 52. Types of meshing techniques used during the analysis.

The primary region of interest in this case was the cross-section in the base plate under the weld toe line. There is one weld toe line of interest in the tube on plate geometry, and it is highlighted in the following figure. The cross-section below to this line along the axis of symmetry may be used for analysis.

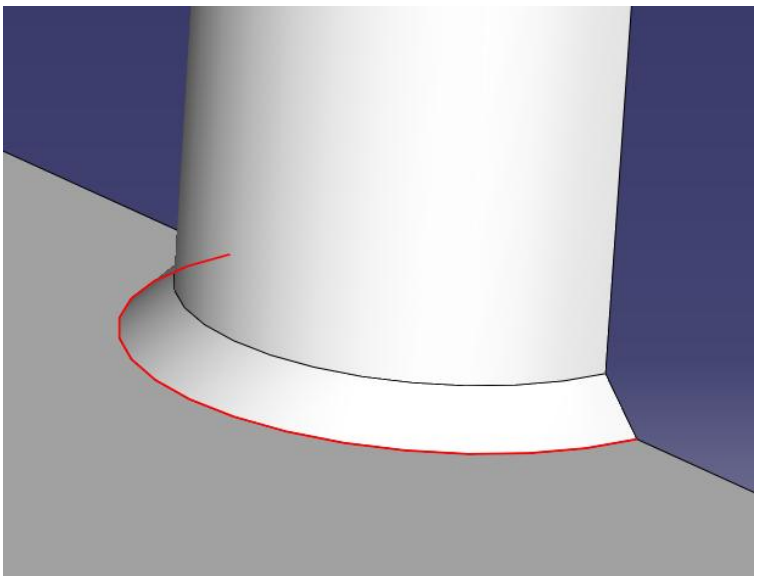

Figure 53. Weld toe line of interest.

Regions close to the area of interest were meshed relatively finely, with an effort being made to ensure all of the elements were as close to cubic as possible. Further away from the area of interest, coarser meshes were used to minimize the computational intensity. The resulting mesh is shown in the following figures.

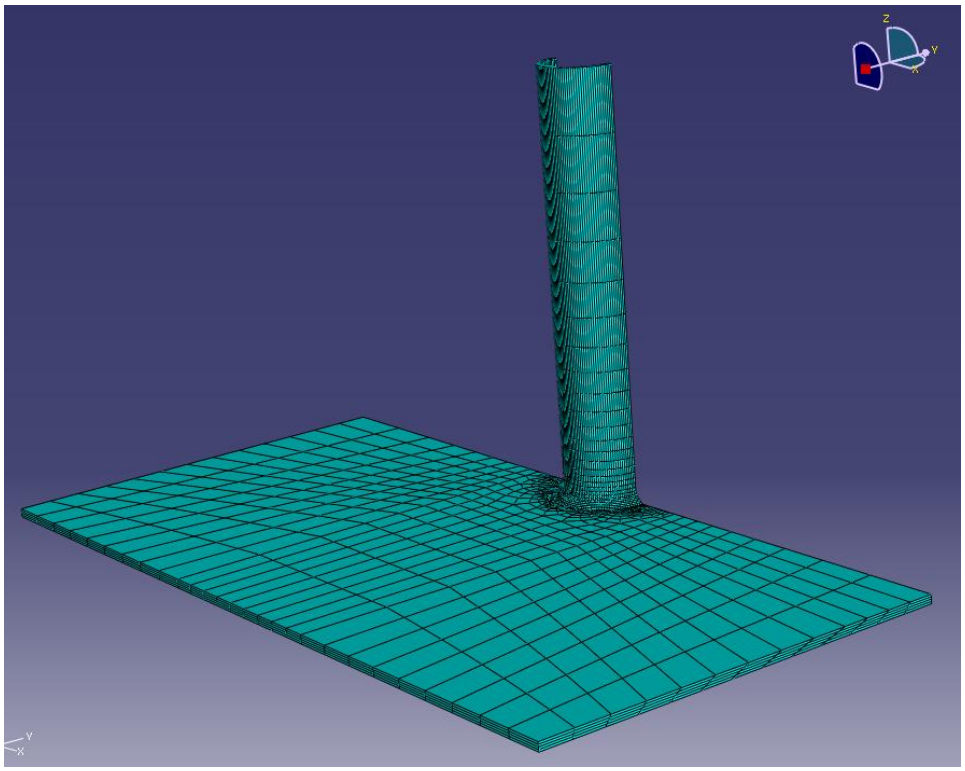

Figure 54. Global overview of the mesh used for a circular tube on plate under bending.

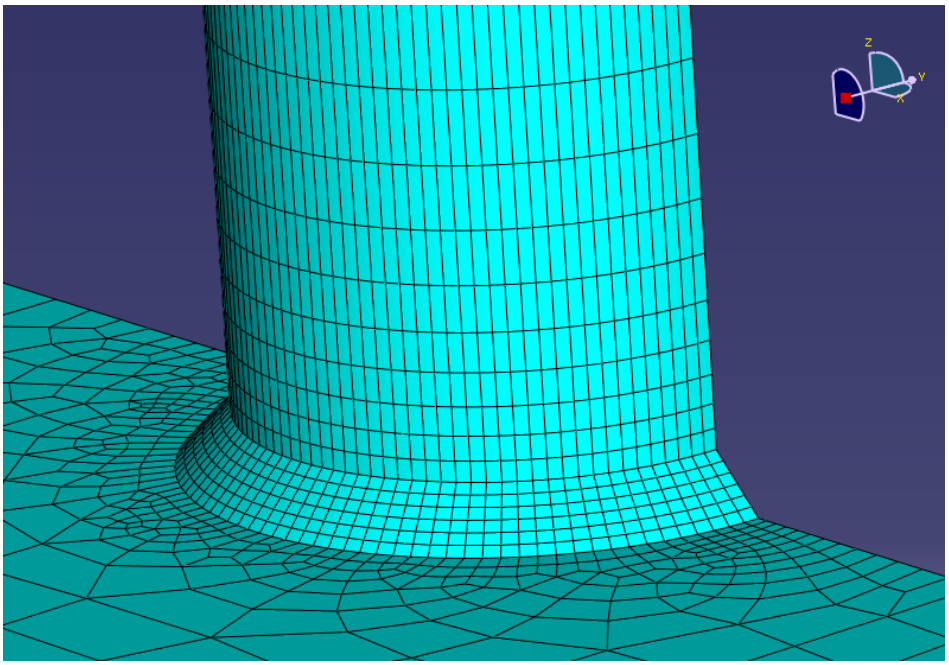

Figure 55. Mesh in the weld area for a circular tube on plate under bending.

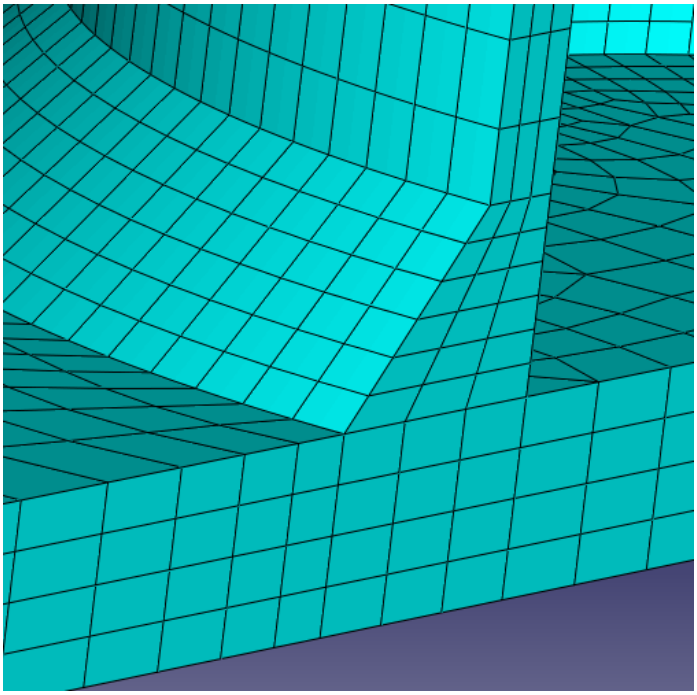

Figure 56. Mesh in the area of interest for a circular tube on plate under bending.

The stress distributions generated by the above meshes using quadratic elements were found to give sufficiently accurate stress readings in the inboard 50% of the cross section of the base plate directly underneath the weld toe line.

4.4.3.4 Three-Dimensional Coarse Mesh Stress Distribution in the Circular Tube on Plate

The stress distribution generated by the above mesh is shown in the following figure.

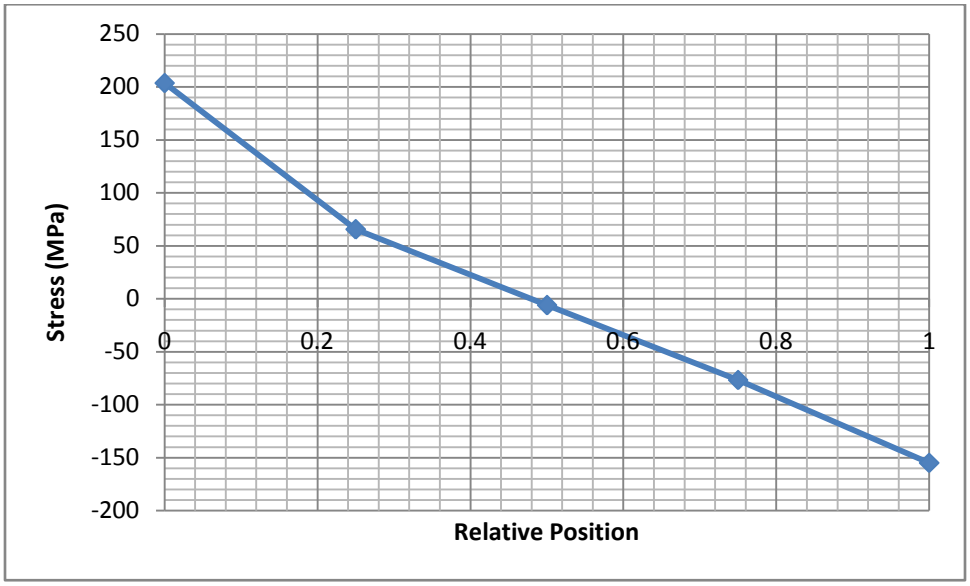

Figure 57. Coarse mesh stress distribution for a circular tube on plate under bending.

The coarse mesh distribution is expected to coincide with the fine mesh stress distribution of the cross section from the 0.25 to 0.75 relative position marks. This will be verified in the following section, where the coarse and fine mesh stress distributions for this cross section will be overlaid.

4.4.3.5 Three-Dimensional Fine Mesh Stress Distribution in the Circular Tube on Plate

In order to assess the accuracy of the stress distribution generated by the coarse mesh, the stress distribution generated by a finely-meshed model of the T-joint was to create a comparison. The finely-meshed data used in this case was produced by Rakesh Goyal, of John Deere. The geometry used was identical to the one shown in section 4.4.3.2, except that a radius of 0.3125 mm was applied to the edges of the fillet weld.

The fine mesh stress distribution is shown in the following figure.

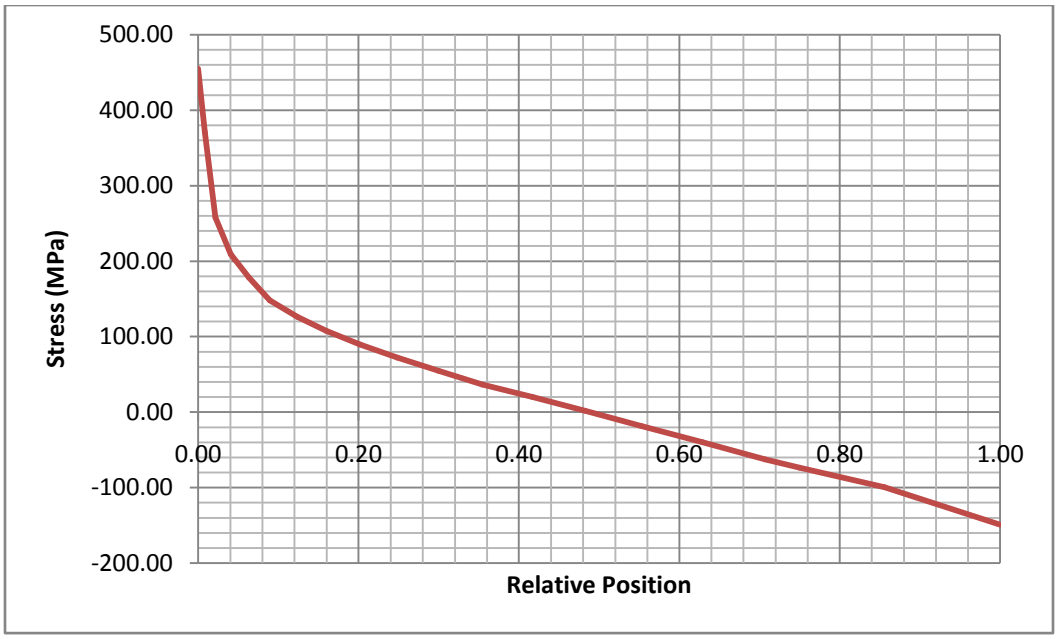

Figure 58. Fine mesh stress distribution for a circular tube on plate under bending [24].

The coarse and fine mesh distributions can now be overlaid to verify if the two distributions match over the domain of relative positions from 0.25 to 0.75. This is shown in the following figure.

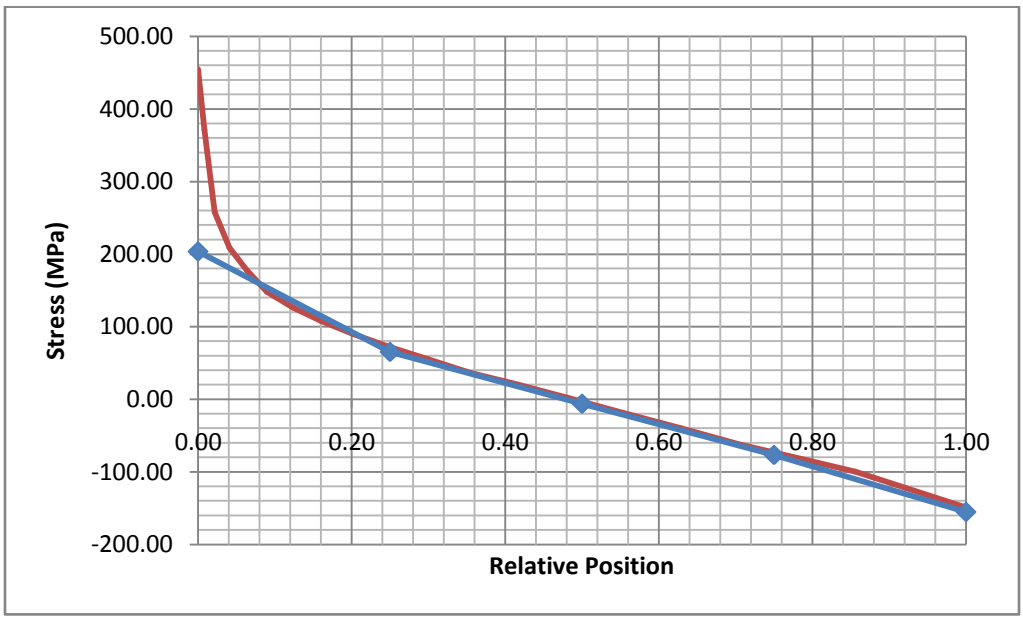

Figure 59. Overlay of coarse and fine mesh stress distributions for the circular tube on plate under bending.

It can be seen that the two distributions do match up over the inboard 50% of the cross-section. It can therefore be said that the coarse mesh data for the stress distribution is valid for the interior half

of the cross-section. It will now be shown that the data from the interior of the cross-section may be manipulated to generate maximum stress values.

4.4.3.6 Ratio of Inboard and Total Bending Moments

It is expected that the ratio between the inboard and total bending moments be 0.1. This relationship has been found to hold for a variety of loading conditions and geometries.

In this case, the total moment acting in the finely-meshed case was found to be 28.7 Nm. The moment generated by the inboard 50% of the coarse-mesh stress distribution was found to be 2.92 Nm. The ratio between these two values is therefore 0.10, confirming the predicted value.

4.4.4 Circular Tube on Plate Under Tension

The third welded connection that will be analyzed is the circular tube on a plate. For this geometry, the stress distribution in the region of interest will be found using a coarse mesh only 4 elements thick. This stress distribution will then be compared to the stress distribution generated using a finely-meshed model. It is expected that the stress distributions for the two meshes should align over the inboard 50% of the cross section.

It is also expected that the moment generated by the stress distribution over the inboard 50% of the cross section will account for 10% of the total moment. The total moment can therefore be found using only the stress distribution of the inboard 50% of the cross-section. Once this total moment is known, both the hotspot and peak stresses can be found, and finally the fatigue life of a weldment may be determined.

The joint was assumed to be made of a typical structural steel, and was analyzed given a geometry provided by Rakesh Goyal at John Deere. The geometry was meshed using hexagonal elements, with the mesh density being higher in the areas of interest. The area of interest in this case was the cross-section running through the base plate below the weld toe line.

4.4.4.1 Material Properties

The material assumed for this trial was standard structural steel. This matched the earlier work done by Rakesh Goyal of John Deere, making comparisons of the results easier.

The material was assumed to have a Young's Modulus of 200 GPa and a Poisson's Ratio of 0.3. It was also assumed to behave in a perfectly elastic manner. This is a reasonable assumption to make, as most design cases limit their applied stress values to the elastic regime.

4.4.4.2 Geometry of Circular Tube on Plate

The geometry and loading of the cylindrical tube on the plate is shown in the following figure:

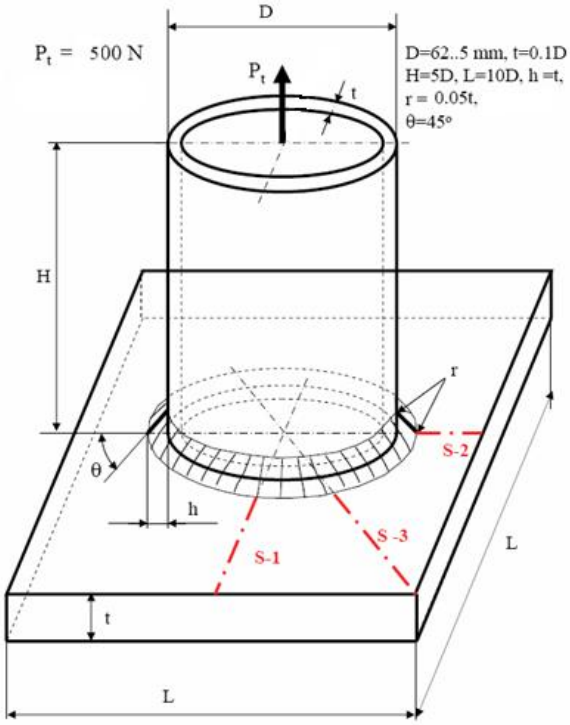

Figure 60. Dimensions and load acting on circular tube on plate under tension [24].

The base plate has dimensions of 625 mm x 625 mm x 6.25 mm, and the cylinder has a height of 312.5 mm. The weld toe radius is 0.3125 mm. The angle of the weld is 45°, with a height of 6.25 mm. Finally, the diameter of the tube is 62.5 mm.

In order to minimize the computational complexity of the problem, the geometry was cut along both axes of symmetry of the loading case. The resulting geometry is shown in Fig.61.

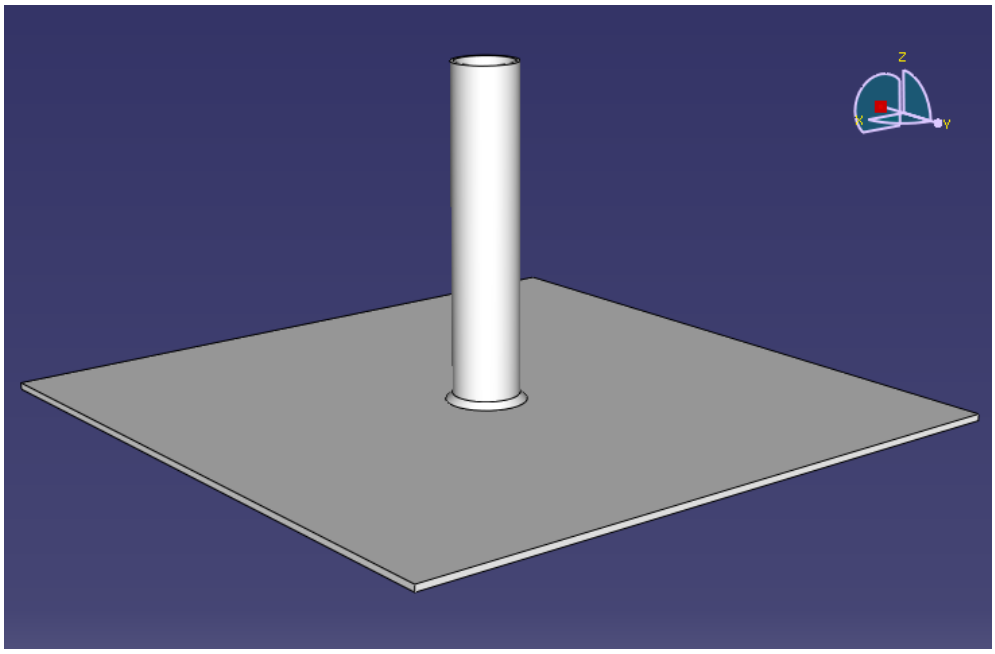

Figure 61. Circular Tube on Plate Full Model.

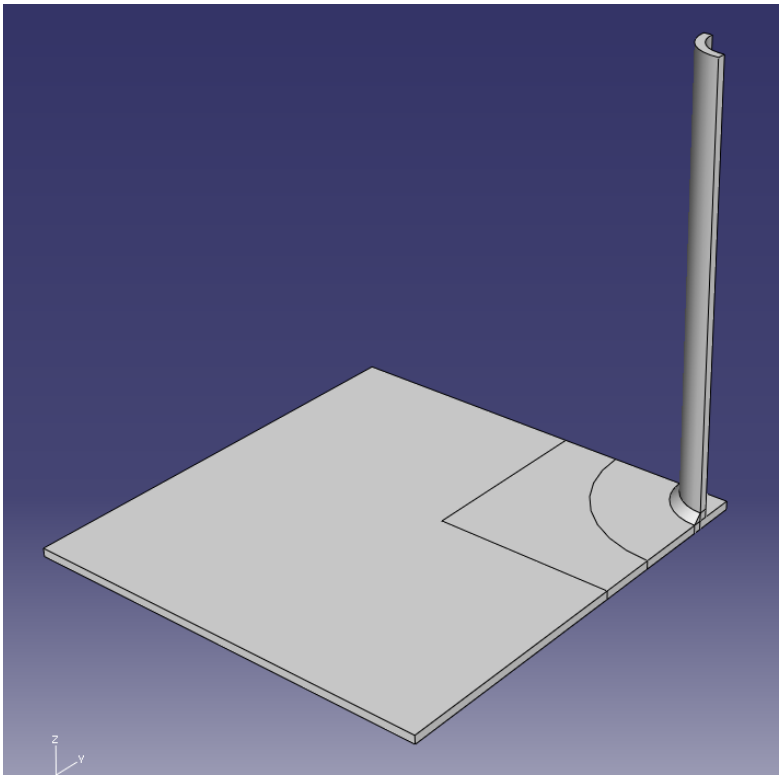

Figure 62. Model of the T-Joint geometry cut along both axes of symmetry

Loads and boundary conditions were then applied to the model.

Boundary conditions consisted of pinned constraint at the corner of the base plate furthest from the tube. The face cut along the x-axis was set to have a y-symmetry boundary condition. This implied the face could not displace in the y-direction, and could not rotate about the x- or z-axes. The face cut along the y-axis was set to have a x-symmetry boundary condition. This implied the face could not displace in the x-direction, and could not rotate about the y- or z-axes. The applied boundary conditions are shown in the following figures.

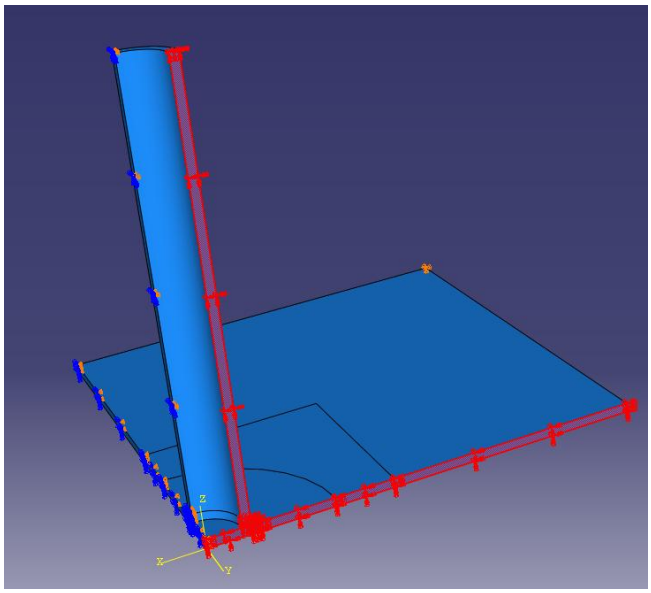

Figure 63. Area subjected to y-symmetry boundary condition highlighted in red.

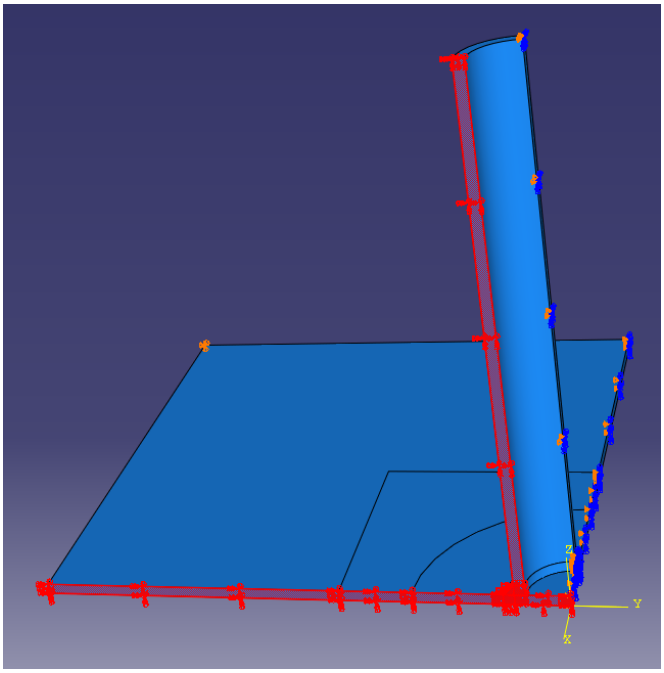

Figure 64. Area subjected to x-symmetry boundary condition highlighted in red.

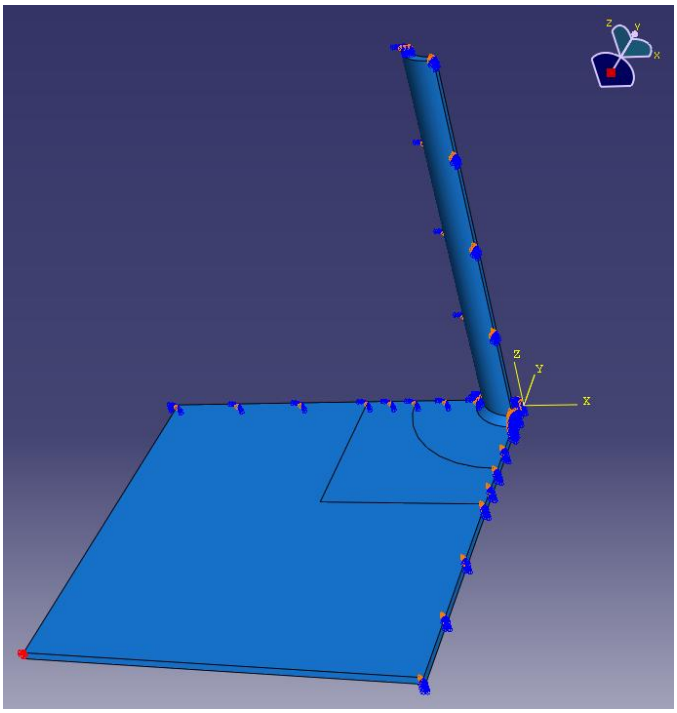

Figure 65. Point subjected to pinned boundary condition highlighted in red.

The load applied to this case was a surface traction applied as shown in the following figure. A load of 125 N was generated by applying a surface traction over the upper rim area of the tube. The magnitude of the applied pressure was -0.47 MPa.

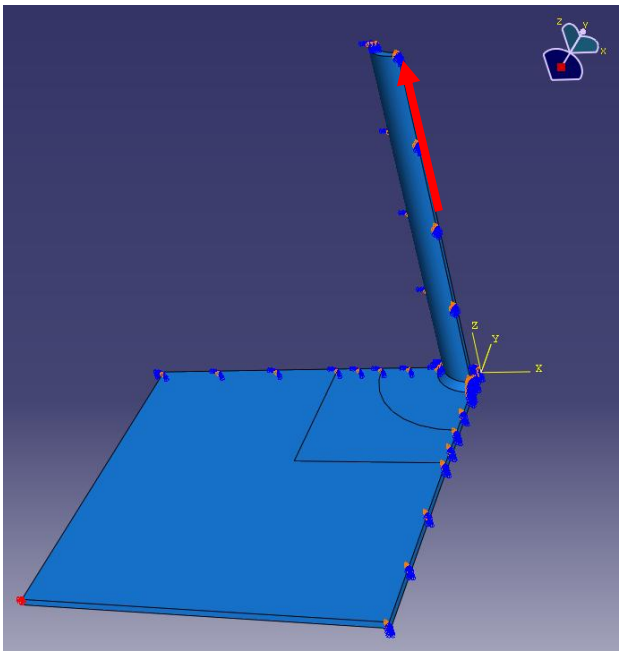

Figure 66. Point of application and direction of load marked by red arrow.

4.4.4.3 Meshing of the Circular Tube on Plate

The geometry was meshed entirely using hexagonal quadratic elements. Structured meshes were used wherever possible, but regions with more complicated geometries were meshed using swept meshing techniques. For the swept meshes, mapped meshing techniques were used where appropriate.

The sections of the geometry meshed using swept advancing front meshing techniques are shown below in yellow, and the regions meshed using a structured mesh are shown in green. Advancing front meshing was used almost exclusively for this geometry.

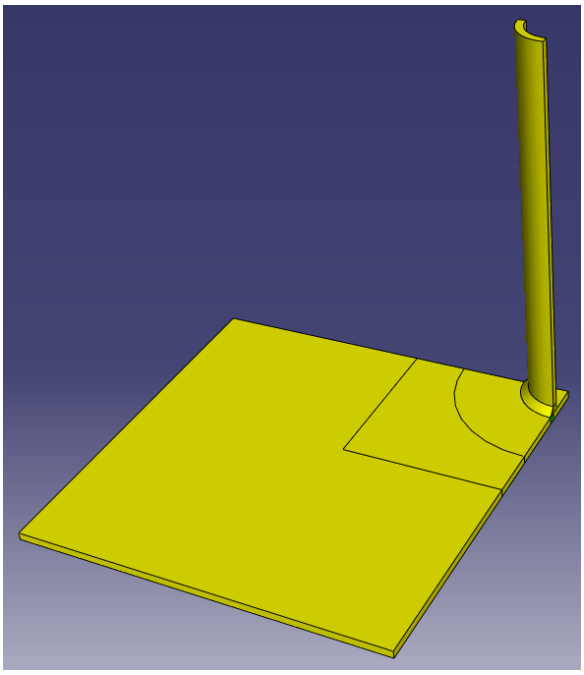

Figure 67. Types of meshing techniques used during the analysis.

The primary region of interest in this case was the cross-section in the tube adjacent to the weld toe line. There is one weld toe line of interest in the tube on plate geometry, and it is highlighted in the following figure. The cross-section adjacent to this line along the axis of symmetry may be used for analysis.

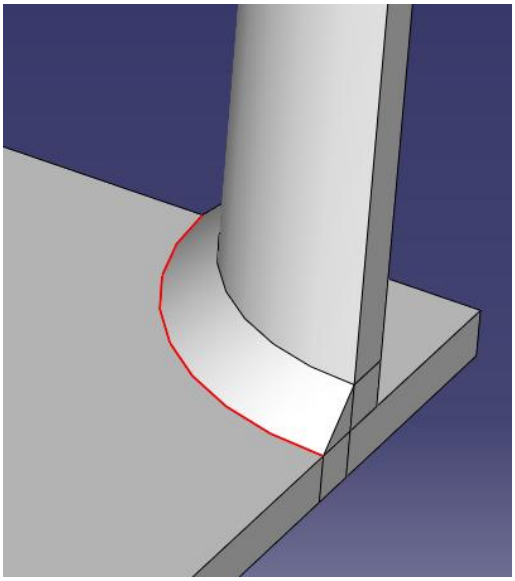

Figure 68. Weld toe line of interest.

Regions close to the area of interest were meshed relatively finely, with an effort being made to ensure all of the elements were as close to cubic as possible. Further away from the area of interest,

coarser meshes were used to minimize the computational intensity. The resulting mesh is shown in the following figures.

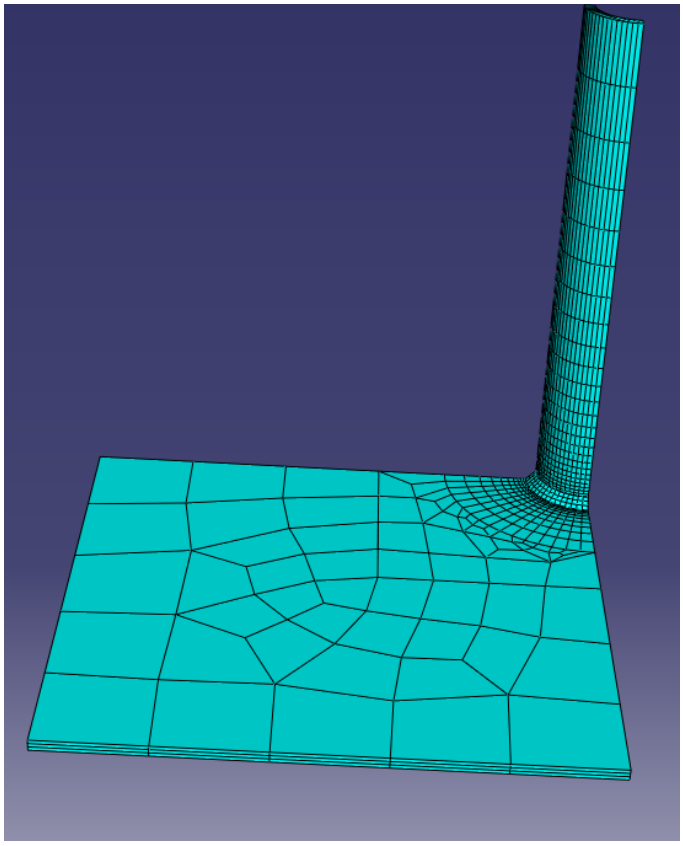

Figure 69. Global overview of the mesh used for a circular tube on plate under tension.

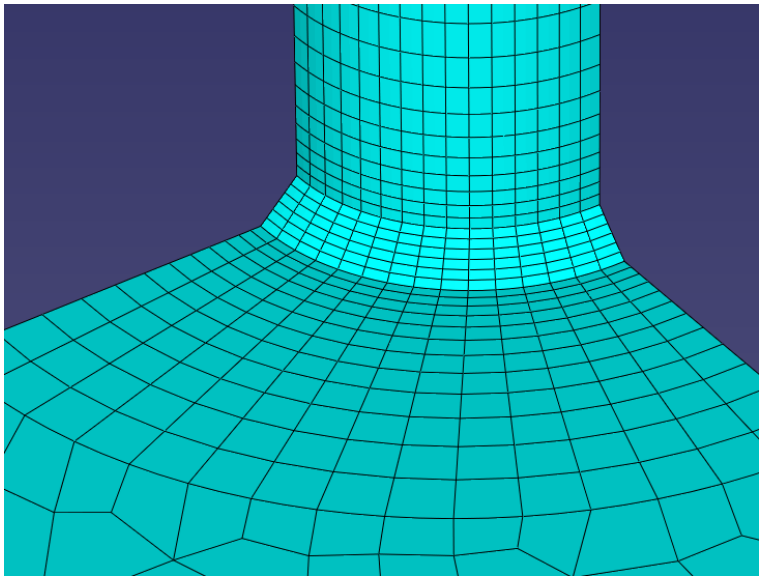

Figure 70. Mesh in the weld area for a circular tube on plate under tension.

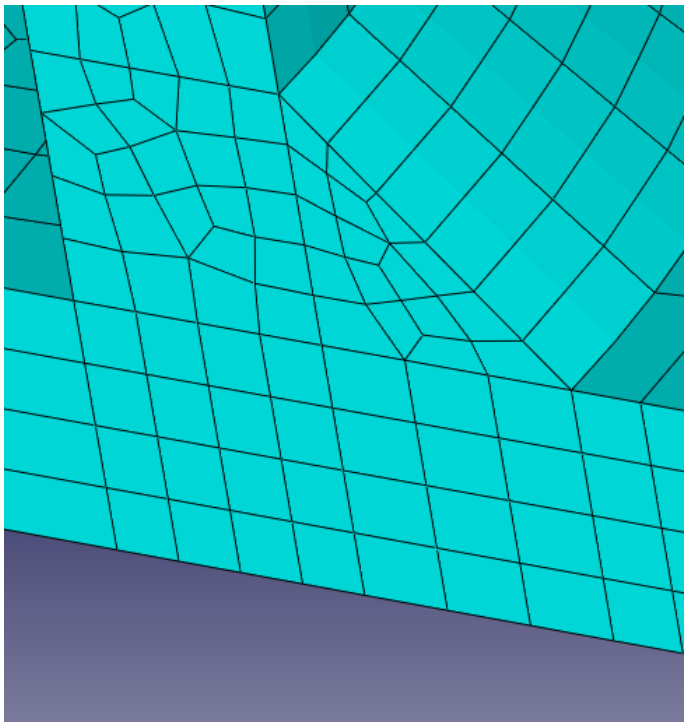

Figure 71. Mesh in the area of interest for a circular tube on plate under tension.

The stress distributions generated by the above meshes using quadratic elements were found to give sufficiently accurate stress readings in the inboard 50% of the cross section of the base plate directly underneath the weld toe line.

4.4.4.4 Three-Dimensional Coarse Mesh Stress Distribution in the Circular Tube on Plate under Tension

The stress distribution generated by the above mesh is shown in Fig.72.

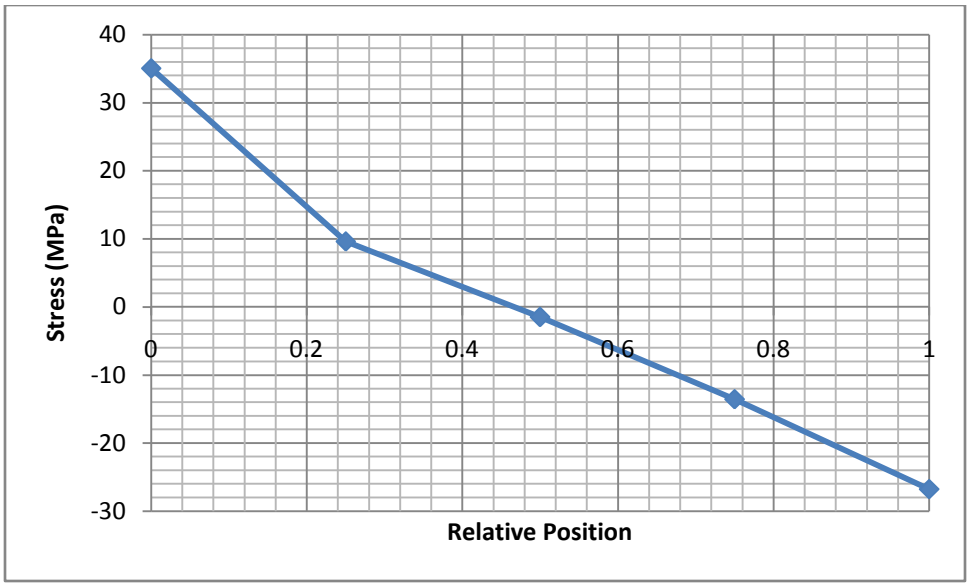

Figure 72. Circular tube on plate bending coarse mesh stress distribution.

The coarse mesh distribution is expected to coincide with the fine mesh stress distribution of the cross section from the 0.25 to 0.75 relative position marks. This will be verified in the following section, where the coarse and fine mesh stress distributions for this cross section will be overlaid.

4.4.4.5 Three-Dimensional Fine Mesh Stress Distribution in the Circular Tube on Plate

In order to assess the accuracy of the stress distribution generated by the coarse mesh, the stress distribution generated by a finely-meshed model of the T-joint was to create a comparison. The finely-meshed data used in this case was produced by Rakesh Goyal, of John Deere. The geometry used was identical to the one shown in section 4.4.1.2, except that a radius of 0.55 mm was applied to the edges of the fillet weld.

The fine mesh stress distribution is shown in Fig.73.

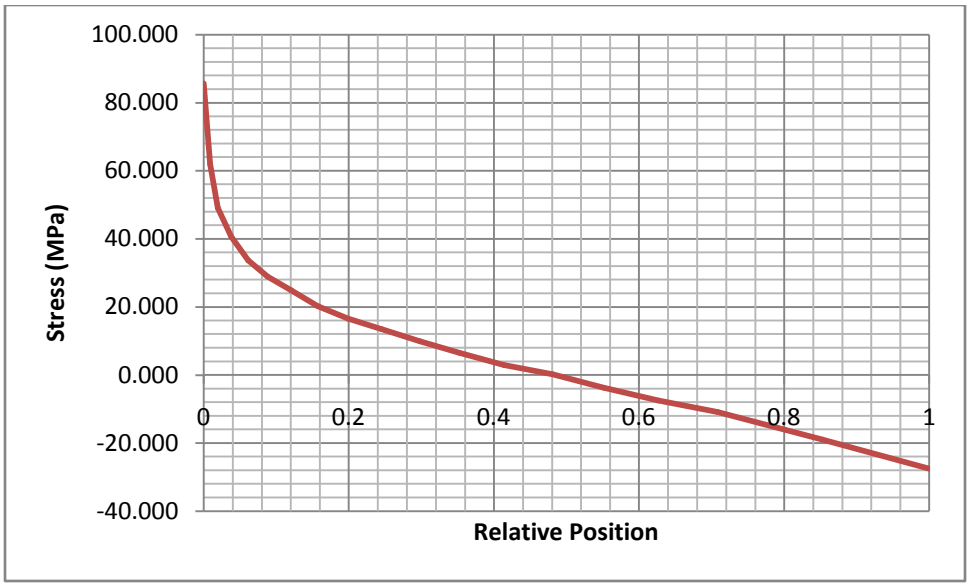

Figure 73. T-Joint fine mesh stress distribution [24].

The coarse and fine mesh distributions can now be overlaid to verify if the two distributions match over the domain of relative positions from 0.25 to 0.75. This is shown in the following figure.

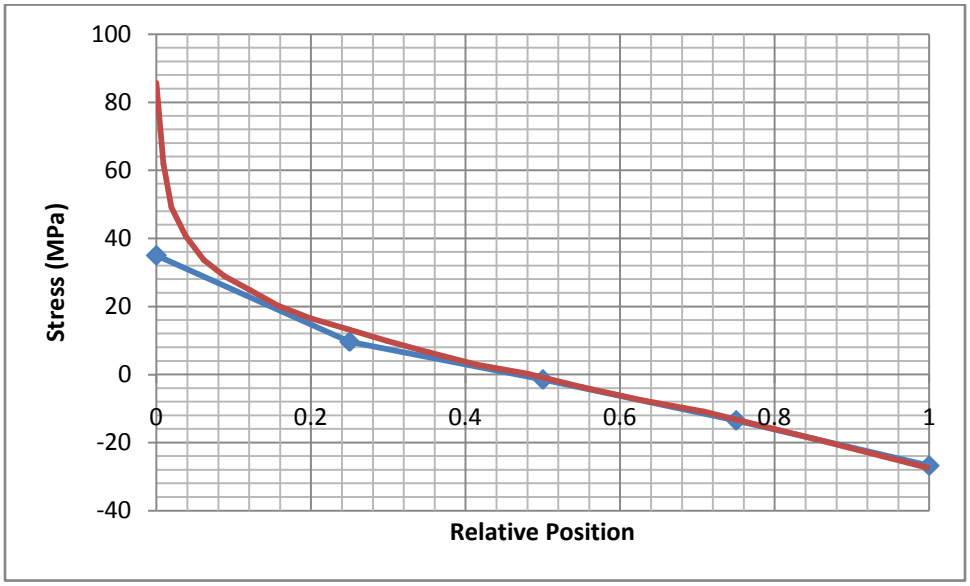

Figure 74. Overlay of coarse and fine mesh stress distributions for the T-Joint.

It can be seen that the two distributions do match up over the inboard 50% of the cross-section. It can therefore be said that the coarse mesh data for the stress distribution is valid for the interior half of the cross-section. It will now be shown that the data from the interior of the cross-section may be manipulated to generate maximum stress values.

4.4.4.6 Ratio of Coarse and Fine Mesh Load Values

It is expected that the ratio between the inboard and total bending moments be 0.1. This relationship has been found to hold for a variety of loading conditions and geometries.

In this case, the total moment acting in the finely-meshed case was found to be 0.48 Nm. The moment generated by the inboard 50% of the coarse-mesh stress distribution was found to be 5.32 Nm. The ratio between these two values is therefore 0.09, slightly off from the predicted value of 0.10, but within the +/-10% allowance specified.

5.0 Experimental Verification

This section outlines the analysis procedure used to predict the fatigue life of a notched and welded component at three distinct load levels. These components were tested by the Fatigue Design and Evaluation Committee of the Society of Automotive Engineers to help determine the accuracy with which the life of a welded structure may be estimated [25]. The GR3 method was used to determine the stresses acting at the critical cross-sections.

The analysis sought to determine the fatigue life for each of the failure conditions for each of the loading cases specified. The fatigue life to crack initiation was found using the strain-life approach. The fatigue life to a crack across the width of a weldment was then found by taking the number of cycles indicated by the strain-life approach and adding the number of cycles required to grow a semi-elliptical crack from its initiation to the point where the crack spans the width of the weldment.

Next, the crack was treated as an edge crack, and the number of cycles required for it to reach the obvious edge crack and brittle fracture stages were determined.

The resulting predictions gave estimates for the various lives of the two components at different load levels. The predictions were then compared to the experimental data generated by the Fatigue Design and Evaluation Committee in order to verify their accuracy.

5.1 Geometries of the two test specimens

The samples tested were both made from 1.5” x 1.5” square cross-section bar stock. The bar itself was 2’ long, end to end. A weld or a notch was placed 1.125” on either side of the midpoint of the bar. The major dimensions for the fatigue test samples are shown in Fig. 75.

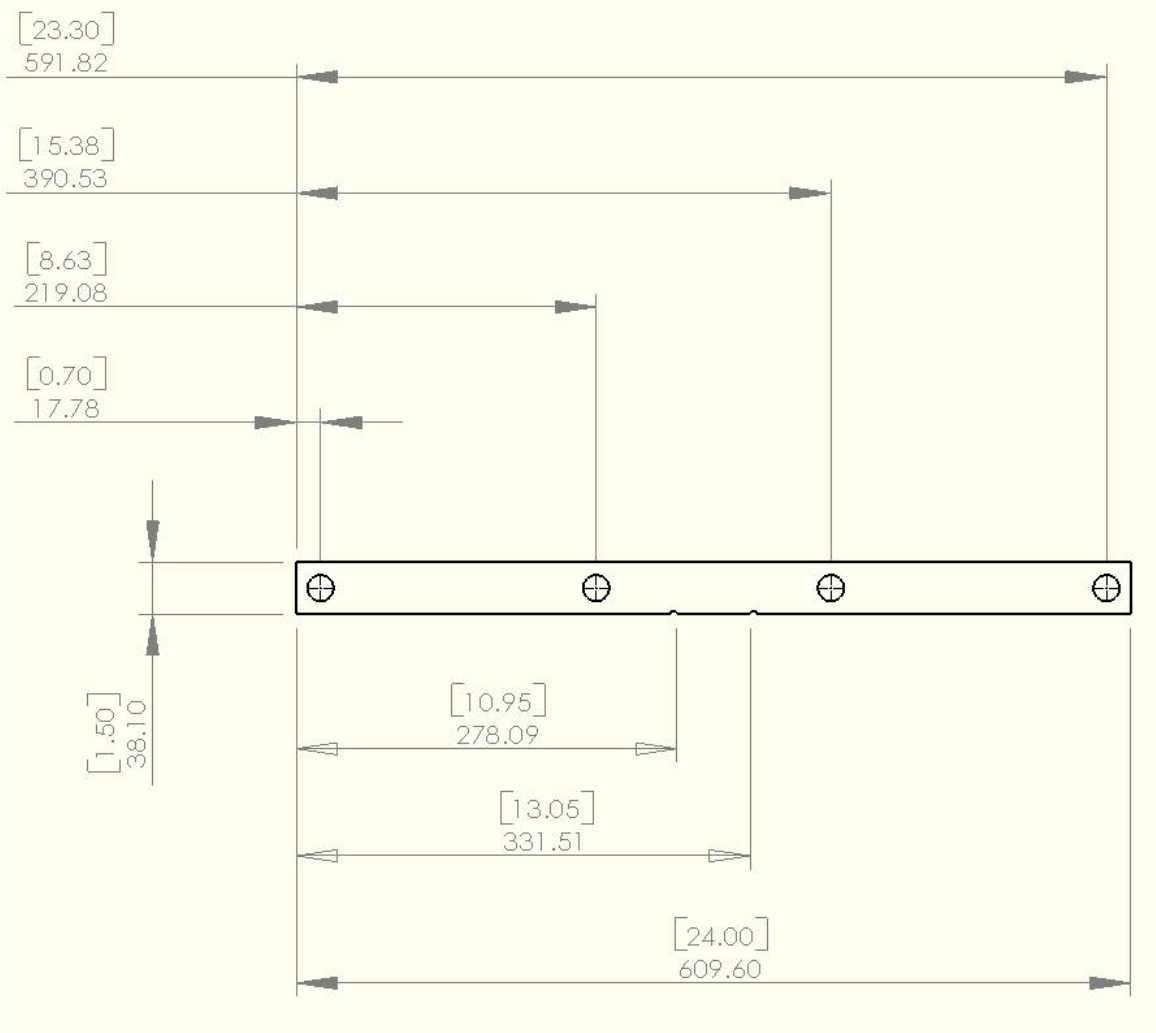

Figure 75. Notched Geometry Side View

5.1.1 Notch Geometry

The notch itself was a U-type notch, with a specified depth and radius. These parameters are summarized in Table 1.

Table 1. Notch geometry details

Radius	0.125”
Depth	0.09375”

The notch was designed to generate a stress concentration factor comparable to that of the weld. An image of the notched configuration is shown in Fig. 76.

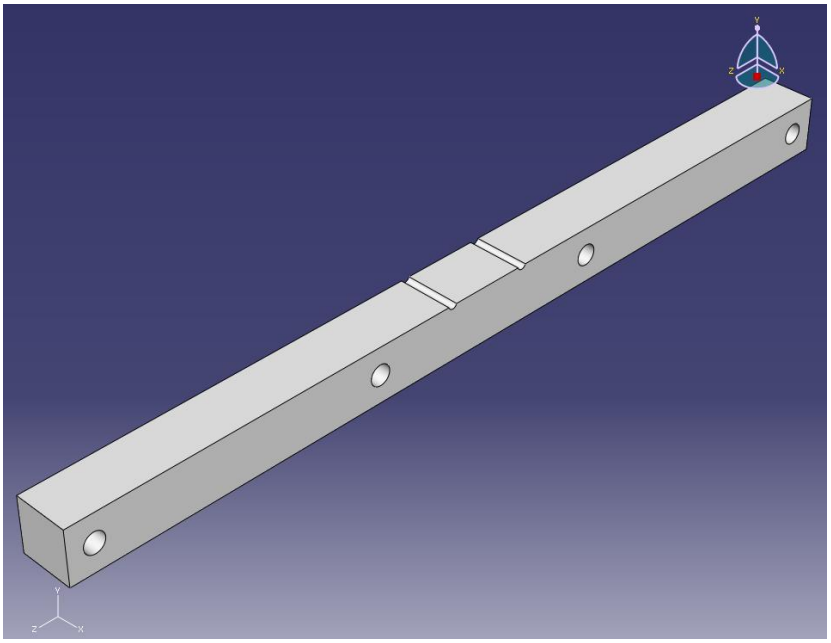

Figure 76. 3D view of the notched bar.

A pictorial example of the depth and radius parameters for a U-notch is shown in Fig. 77.

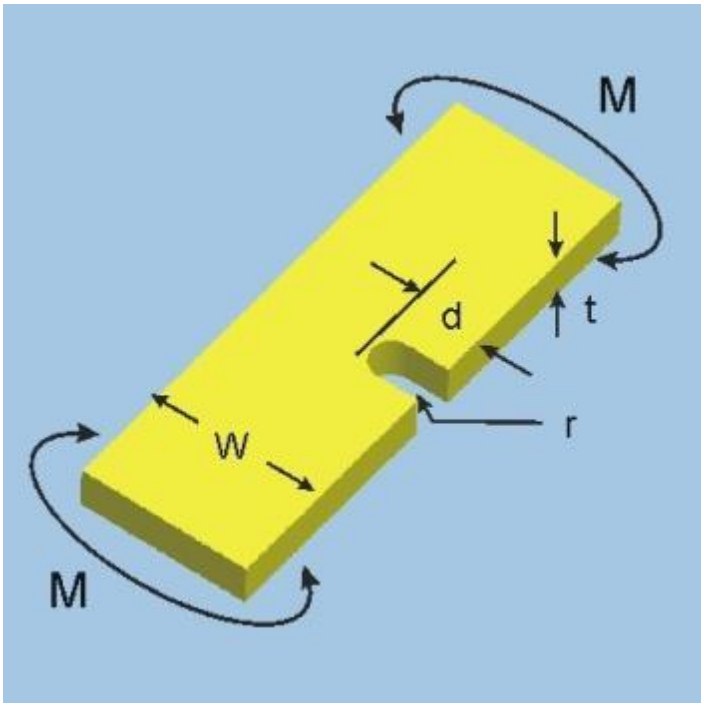

Figure 77. Geometric features of a notched bar.

5.1.2 Weld Geometry

An image of the welded configuration is shown in Fig. 78.

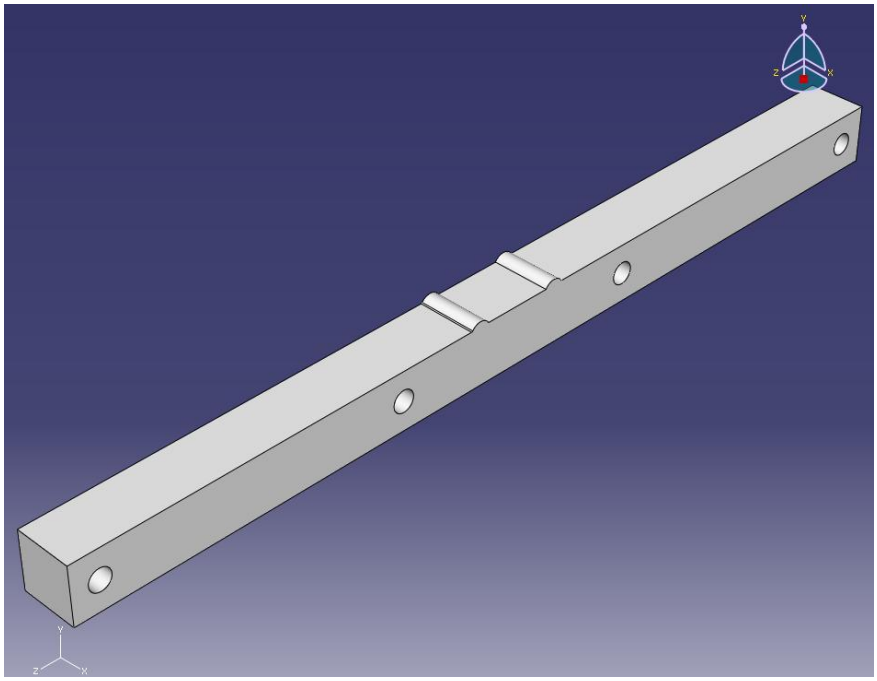

Figure 78. 3D view of the welded bar.

The geometry of the weld is defined using several parameters. These parameters are shown in Fig. 79.

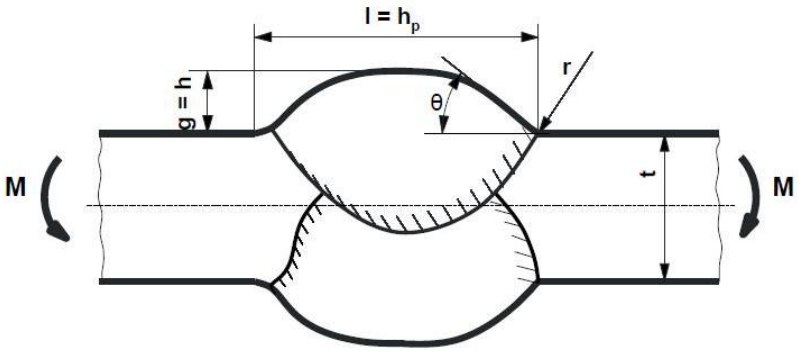

Figure 79. Geometric features of a butt weld.

The parameters indicated above were provided in the data supplied by the Fatigue Design and Evaluation committee in order to determine the effect of the weld on the life of the weldment. The critical dimensions of the weld are included in Table 1.

Table 2. Weld details.

Θ	45°
H	0.14”
h_p	0.47”
R	0.04”
T	1.5”

5.2 Material Properties

The bars were made from A36 steel, which had been stress relieved prior to welding. No specific information was provided concerning the steel’s mechanical properties, however, so the required information was obtained by examining journal articles. For this analysis, an article detailing the failure of an A36 steel strut on the Paseo bridge was used.

The information required to conduct a fatigue life analysis on the welded and notched components fall into three main categories: the Ramberg-Osgood constants, the Manson-Coffin constants, and the Paris equation constants.

The Ramberg-Osgood equation (Eq.2) is used to describe the stress-strain response of a material in both the plastic and elastic regimes. The expression is given below, along with the constants for A36 steel.

Where:

K’ : 194 ksi

n’: 0.226

The Manson-Coffin expression (Eq.4) is used to determine the fatigue life of a component up to crack initiation, given a certain strain amplitude. The values of the constants for A36 steel are given below:

Where:

E: 29000 ksi

σ'_f: 162 ksi

ε'_f: 0.338

b: -0.110

c: -0.480

The Paris equation (Eq.5) is used to determine the rate of crack growth resulting from a given stress intensity factor. The related constants for A36 steel are given below:

Where:

C: 7×10^{-10} ksi*in$^{1/2}$

n: 2.80

It should also be noted that in order to properly use the Paris equation, the R-ratio (Eq.8) at which the Paris equation constants were obtained must be known and accounted for.

K_{min} and K_{max} are the maximum and minimum stress intensities that a weldment is subjected to during loading. The R value that the above Paris equation constants were obtained at was taken as 0.04.

Given this R-ratio, a value for the ratio between the actual and effective stress intensity factors may be estimated by the empirical relationship suggested by Kurihara (Eq.9).

Now that the Paris equation has been adjusted for the R-ratio at which the data was obtained, all that remains to be included into material data are yield and ultimate strengths of the material, as well as the critical stress intensity factor. These values are included below:

Yield Stress: 48 ksi

Ultimate Tensile Stress: 58 ksi

Critical Stress Intensity Factor: 50 ksi*in$^{1/2}$

5.3 Loading and Boundary Conditions

Both the welded and notched configurations were subjected to the same four-point bending loadings. The loading applied was of constant amplitude. There were three load levels at which the life for each configuration had to be determined. These load levels are indicated in the following table.

Table 3. Applied Load Levels.

Load Level	Applied Load
High	6.0 kip
Medium	5.0 kip
Low	3.5 kip

5.4 Notched Specimen Analysis

The analysis may broadly be broken up into two separate cases: analysis of the welded structure and analysis of the notched structure. Each of these cases may then be further broken down into the crack initiation and crack propagation phases. The crack propagation phases, in turn, can be broken down into the propagation from an initial crack to a crack across the width of the part, a crack across the width of the part to an obvious edge crack, and an obvious edge crack to brittle failure.

The notched sample was analyzed using two distinct methods. First, the fatigue life to crack initiation was found using the strain-life technique and the Manson-Coffin expression. This returned the fatigue life from the initiation of load, State 0, to the crack initiation, State 1.

Next, the sample was analyzed via fatigue crack-growth analysis using the Paris equation. This method returns the lives associated with the various stages of crack propagation: Stages 2 through 4.

5.4.1 Notched Specimen GR3 Analysis

The notched sample was analyzed using the GR3 method to determine the peak stress and through-thickness stress distribution acting at the weld toe. In order to model the weld, the geometry shown in Fig. 80 was reduced to a one-quarter model to reduce the computational complexity. The model was cut along lines of symmetry, and is shown in the following figure:

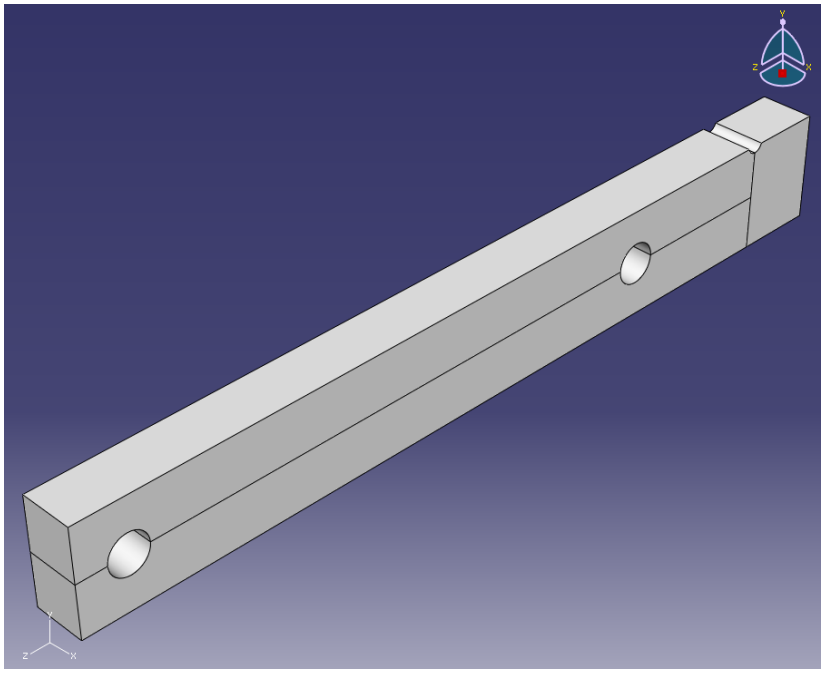

Figure 80. Geometry of notch used for analysis.

The quarter geometry had a symmetry boundary condition applied on the cut face that ran the length of the square rod, and an cantilevered boundary condition applied on the face that was cut in between the two notches. The location of application of the boundary conditions and the type of boundary used is shown in the following figures:

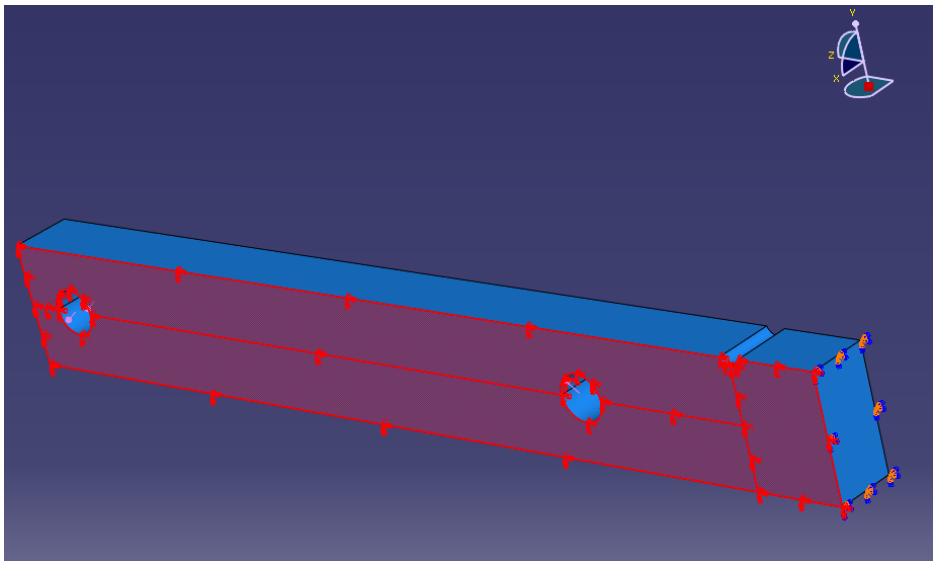

Figure 81. Region of application of the x-symmetry boundary condition to the notched geometry.

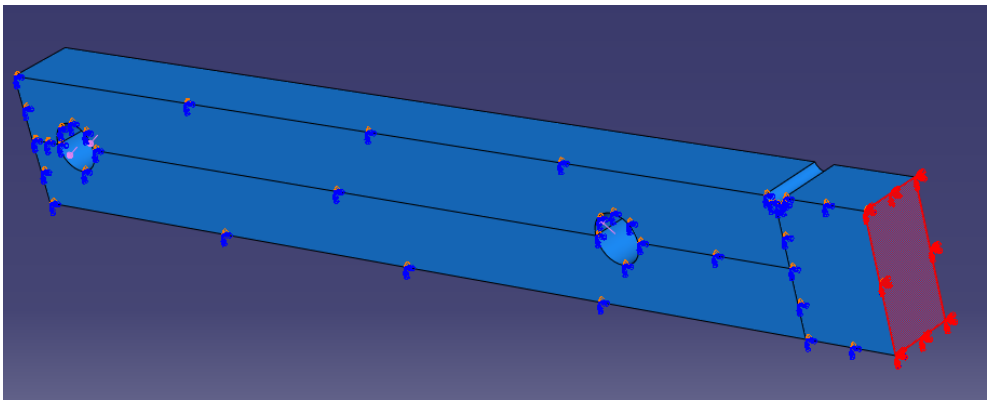

Figure 82. Region of application of the cantilever boundary condition to the notched geometry.

The load was applied in the form of pressures on the interior surfaces of the holes in the part. A pressure along the upper and lower faces was applied to generate the desired load level.

The coarse mesh used for the GR3 analysis was four elements thick in the through-thickness direction. This is shown in Fig. 83:

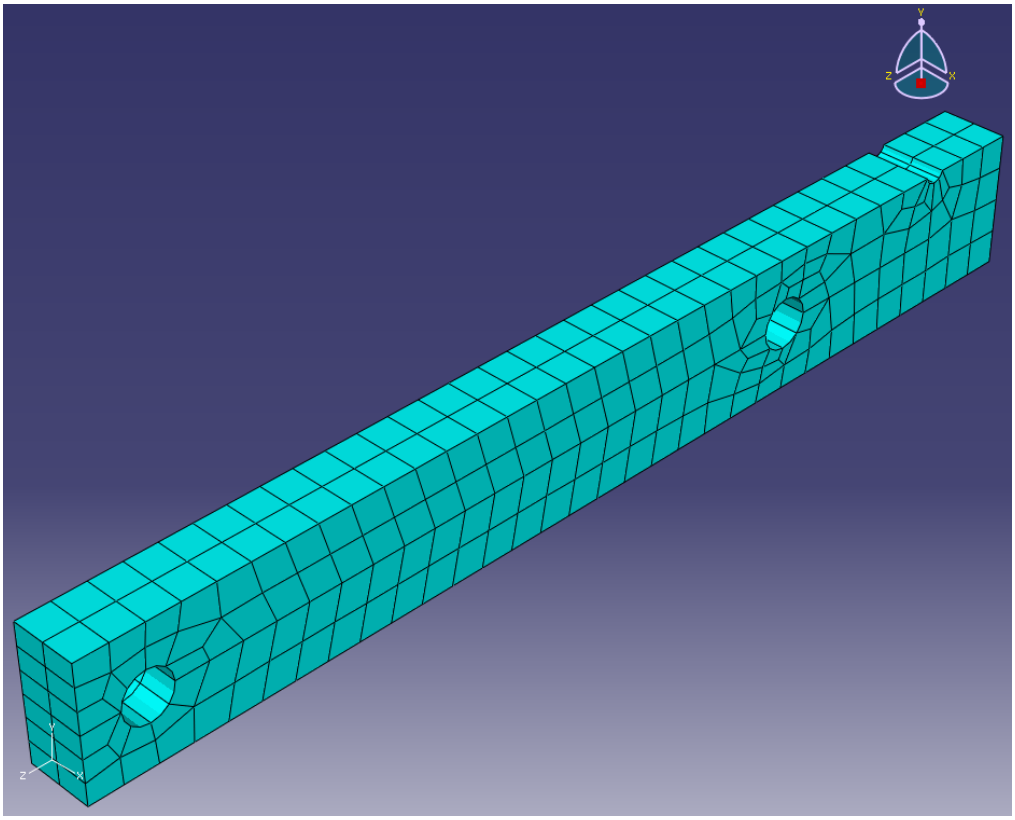

Figure 83. Coarse mesh of the notched geometry.

The coarse-mesh through-thickness stress distribution at the notch tip is given in the following figure:

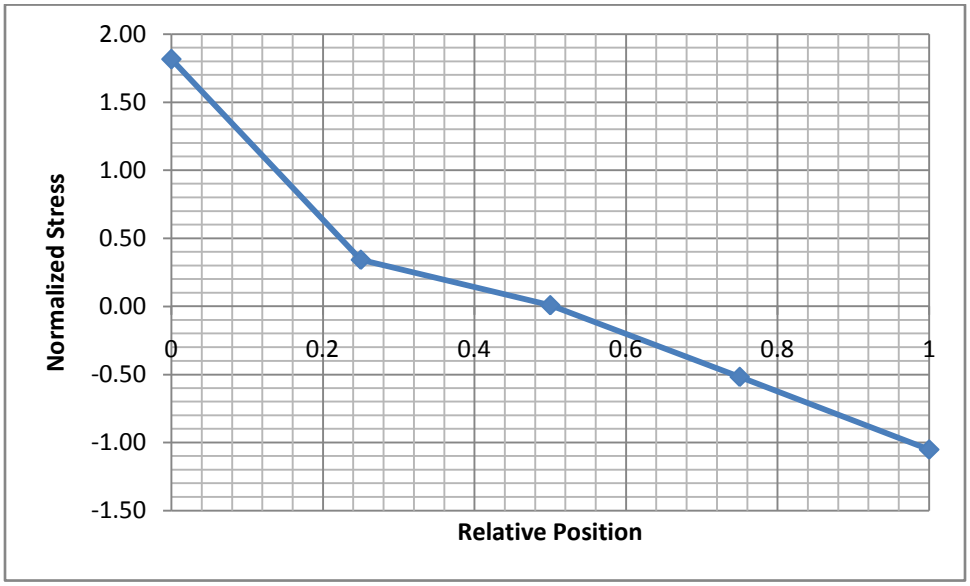

Figure 84. Coarse mesh through-thickness stress distribution below the notch tip

The coarse-mesh stress distribution matches the fine-mesh stress distribution reasonably well over the inboard half of the cross section, as shown in the following figure. The stresses were normalized using the maximum nominal stress value.

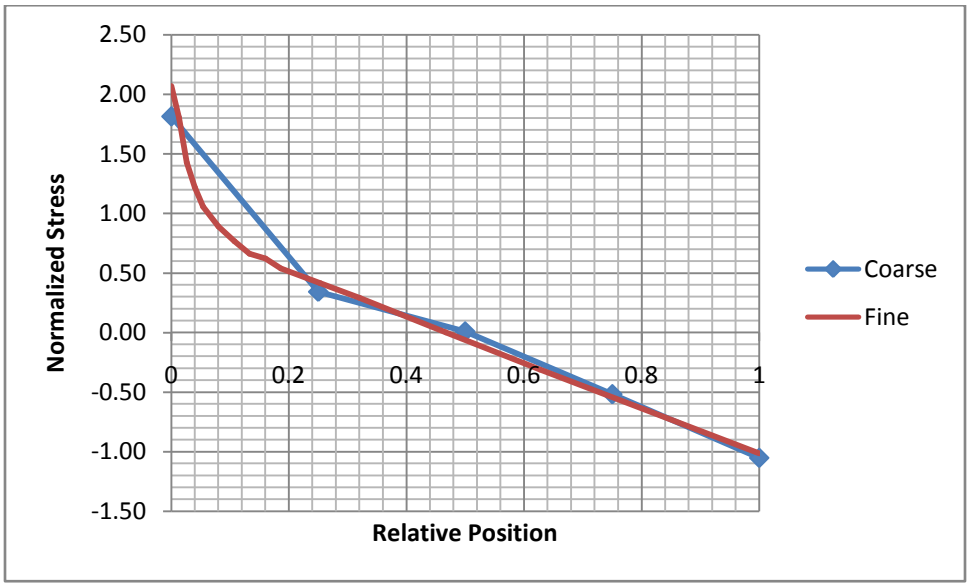

Figure 85. Comparison of the fine and coarse mesh through-thickness stress distributions below the notch tip.

The stress values provided by the coarse mesh were input into Eq.59 to obtain the moment acting and Eq.63 to determine the axial load. These values were then input into Eq.49 and Eq.50 to obtain the nominal membrane and bending stresses. Eq.31, Eq.32, and Eq.33 were then used to determine the peak stress acting at the cross-section. Finally, the stress distribution in the cross-section under the weld toe was found using Eq.48. Eq.48 was used in lieu of Monahan's equation, Eq.47, because Monahan's equation only works reliably for fillet welds.

All three of the distributions are overlaid in Fig. 86.

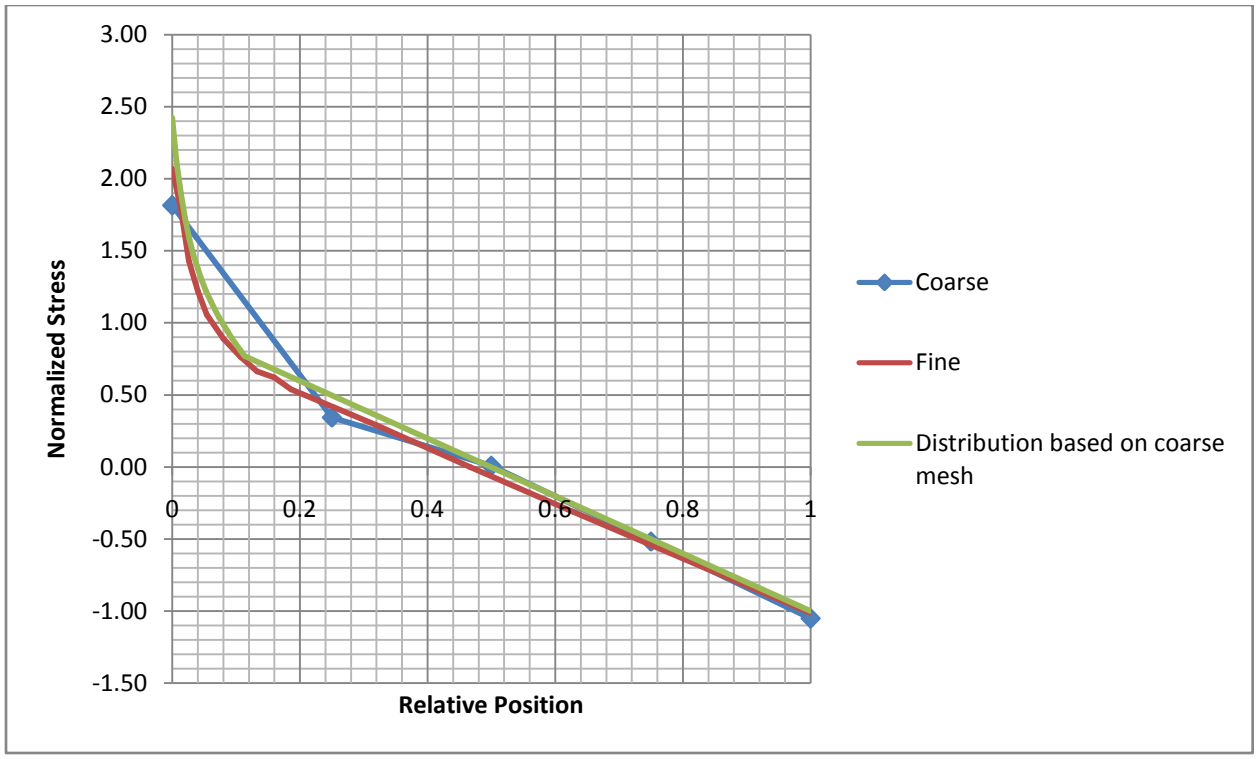

Figure 86. Fine mesh, coarse mesh, and through-thickness stress distribution based on coarse-mesh results.

The through-thickness stress distribution over predicts the intensity of the stress field near the notch slightly, but this is largely due to the intensity of the peak stress near the notch tip being slightly higher than the value predicted using Eq.31, Eq.32, and Eq.33.

5.4.2 Notched Specimen Strain Life Analysis

The number of cycles required to initiate a crack in the notched specimen was determined using the strain-life method. The first step to performing the analysis is to determine the nominal stress acting in the critical cross-section.

Given that the component was subjected to four-point bending, the only load acting on the notched cross-section was the bending moment. The moment was calculated using classical techniques, and the gross nominal bending stress for the cross-section was then determined. The gross nominal stresses were found to have the following values:

Table 4. Nominal Stresses.

Load Level	Nominal Gross Stress
High	42.2 ksi
Medium	35.1 ksi
Low	24.7 ksi

In contrast to this, the nominal stresses found using the GR3 method were slightly more severe:

Table 5. Nominal Stresses found using the GR3 method.

Load Level	Nominal Gross Stress
High	46.4 ksi
Medium	38.6 ksi
Low	27.2 ksi

The stresses are over predicted by roughly 10%, which is the outer range of the error experienced when using the extrapolation from the moment generated by the inboard stress field to the total moment acting on the critical cross-section. However, it is expected that this will lead to a conservative life-estimate for the component, and the analysis will proceed using the value suggested by the GR3 method.

The next step in determining the strain-life of the component would be to find the maximum stress acting on the critical cross-section necessitates. This requires that the stress concentration factor of the notch be found. This value was obtained by entering the notch geometry into the solver on efatigue.com [4]. The solver returned a gross bending stress concentration factor $K_b = 2.37$, resulting in the following local maximum stresses at the notch tip:

Table 6. Local Elastic Stresses for the Notched Specimen

Load Level	Maximum Local Stress
High	111 ksi
Medium	92.2 ksi
Low	64.9 ksi

Note that all of these maximum local stress values are greater than the yield stress of the material, 48 ksi. As a result of this, either Neuber's rule (Eq.1) or the ESED (Eq.2) method must be incorporated to relate the actual strains at the notch tip with the calculated elastic strains.

Neuber's method is conservative, and would return an upper bound on the strain the part experiences. The ESED method, in contrast, is non-conservative, and returns a lower-bound on the associated strain values.

The nominal stresses, gross stress concentration factor, and relevant material constants were at this point entered into the FALIN program, which computed the strain-life of the notched specimen for each of the load levels. Neuber's method was used to generate a lower bound on the life of the part for every given load level, and the ESED method with a bending correction was used to generate the upper bound. An example of the input for the FALIN program is shown in Fig. 87.

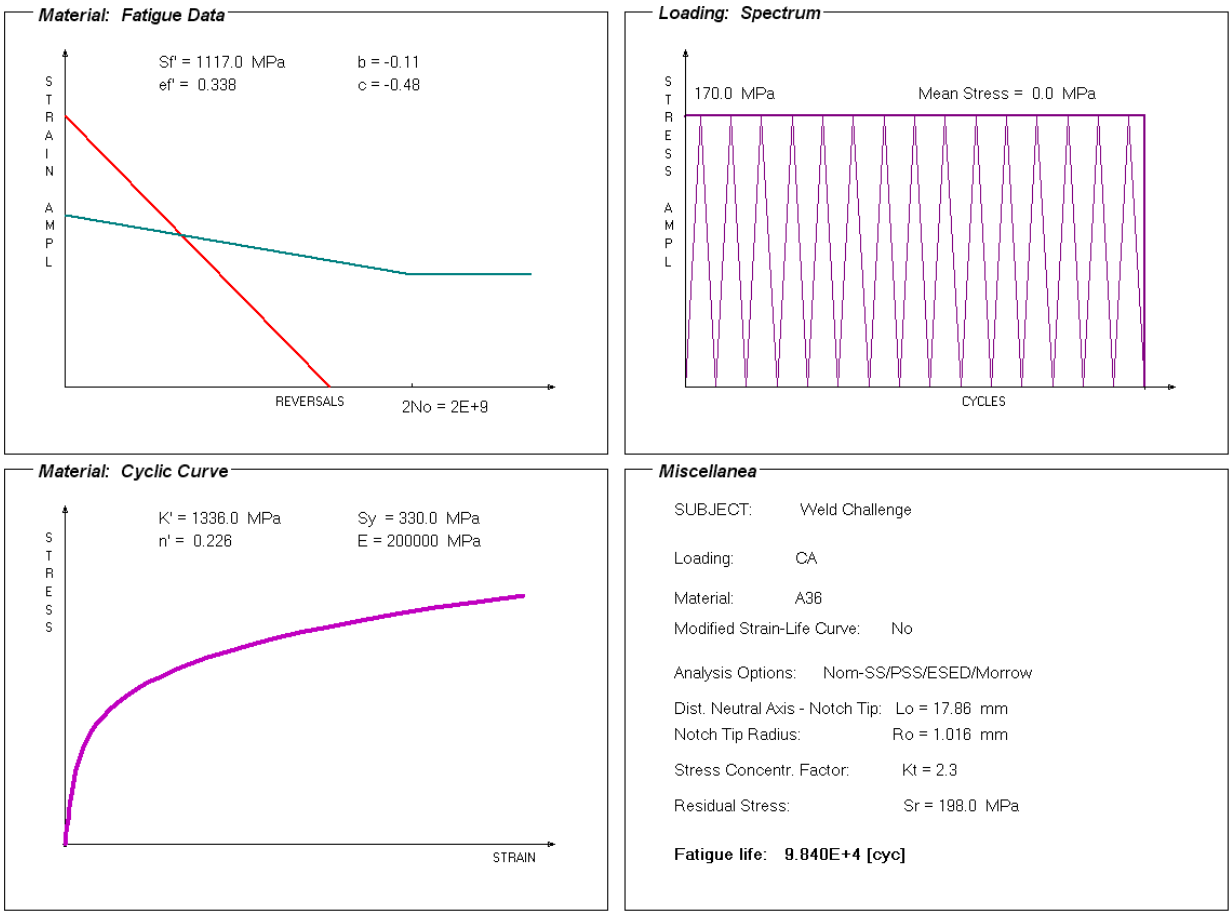

Figure 87. Notched Specimen FALIN Material Data

The FALIN program proceeds with its analysis by calculating the hysteresis loop resulting from the fatigue loading, and outputs the fatigue life for each loading case. A sample output is shown in the Fig. 88.

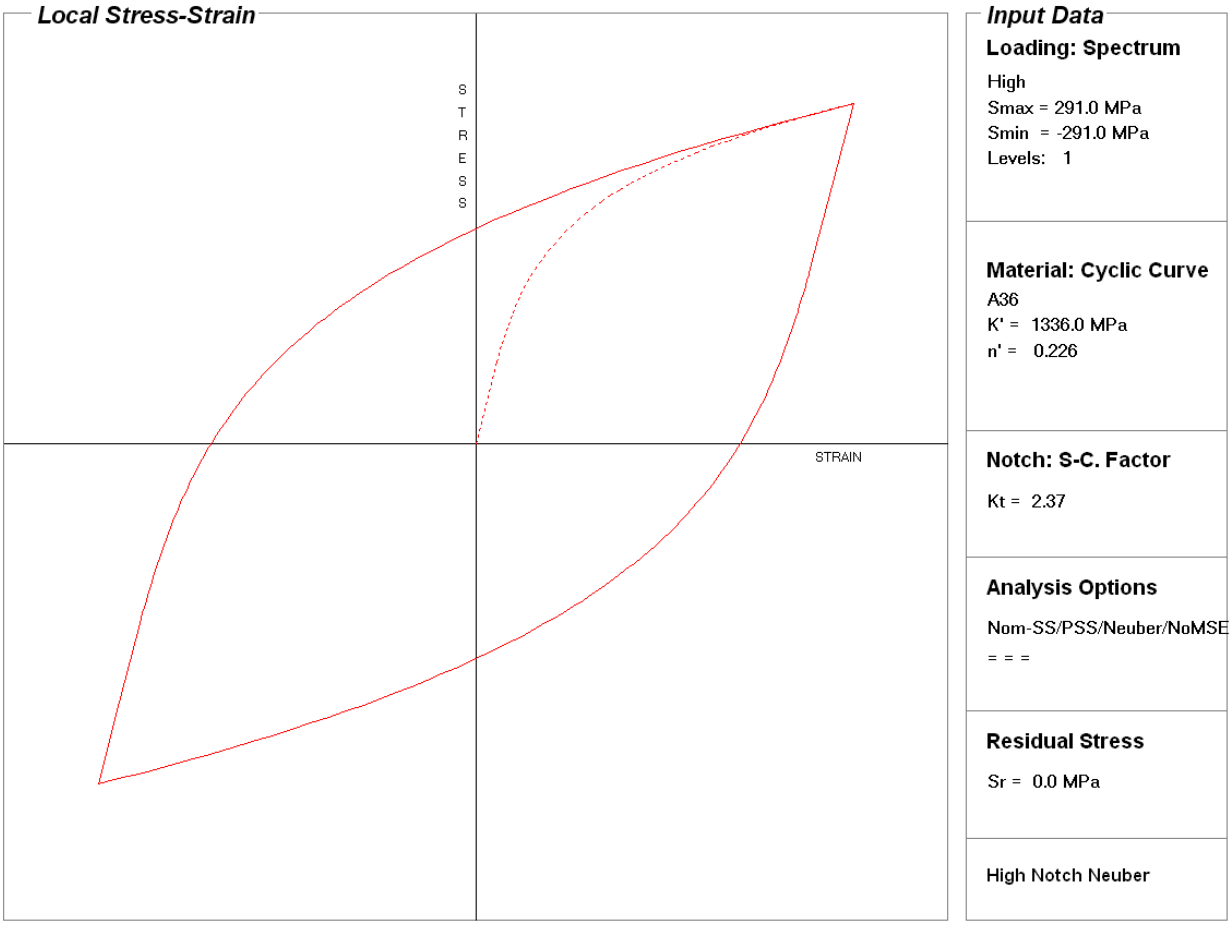

Figure 88. Notched specimen hysteresis loop.

The results of the FALIN fatigue-life calculations are summarized in the following table:

Table 7. Notched specimen strain life predictions

Load Level	Cycles to Failure, Neuber	Cycles to Failure, ESED
High	4955	5130
Medium	12391	13078
Low	77735	89178

This result indicates the life of the notched component to crack initiation, and marks the conclusion of the first stage of the analysis for the notched component. The component will be analyzed further in the following section, which deals with fatigue crack growth.

5.4.3 Notched Specimen Fatigue Crack Growth Analysis

The fatigue crack growth analysis of the notched component was accomplished through use of the Paris equation. In order for the Paris equation to be used, however, the stress intensity factor must be found. The stress intensity factor depends on the stress distribution over that cross-section. This relationship is given in (Eq.10).

In order to proceed with the analysis, the stress distribution in the cross-section, $\sigma(x)$, must be determined. The weight function m(x,a) is handled by the FALPR program. A normalized stress distribution was obtained using the GR3 method and Glinka's Near Notch Tip Stress Distribution, and is shown in the figure below:

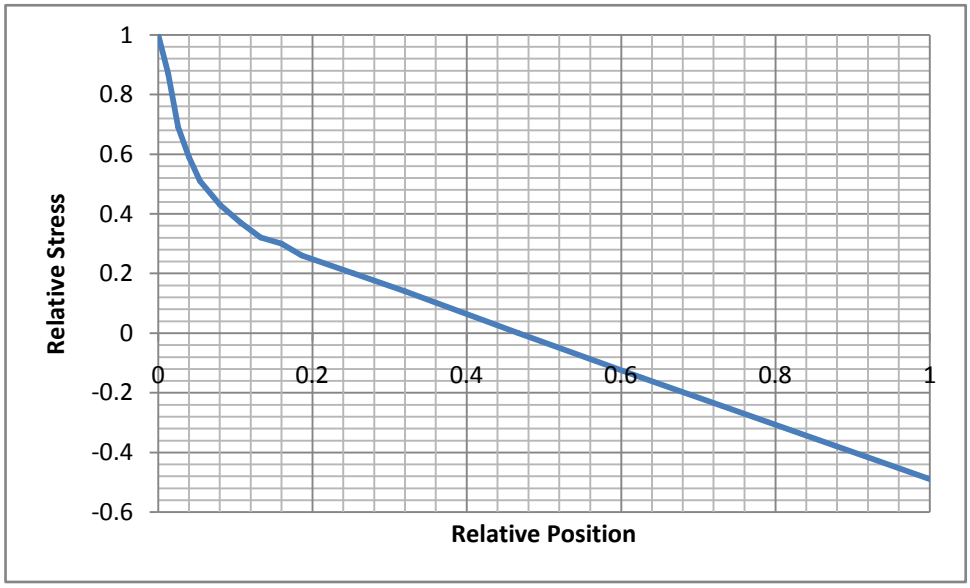

Figure 89. Notched sample through-thickness stress distribution.

Given the stress distribution in the component, the Paris equation constants and the R-ratio at which the constants were obtained, the fatigue crack growth problem now only requires crack size inputs and the type of crack to be set in order to solve the problem.

For the initial crack case, a semi-elliptical crack with an a/c value of 0.3 was assumed. The width of the crack at the surface may be estimated from the images provided in the given data. The image is shown in Fig. 90.

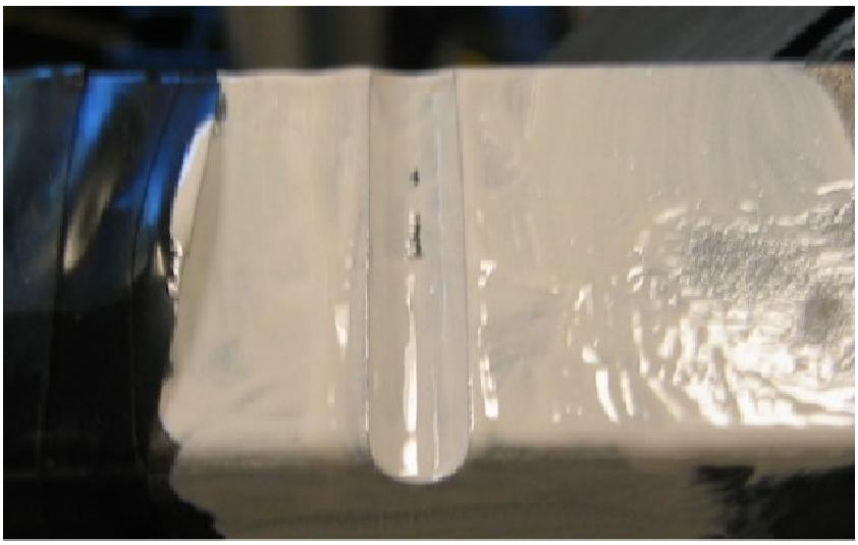

Figure 90. Notched sample crack initiation

By estimating the crack width value from the picture and then using the assumed a/c value of 0.3, an initial crack depth may be estimated. This, however, leaves the final obstacle of determining the final crack depth. This requires examination of the image of the crack spanning the width of the notched part. This image is shown in Fig. 91.

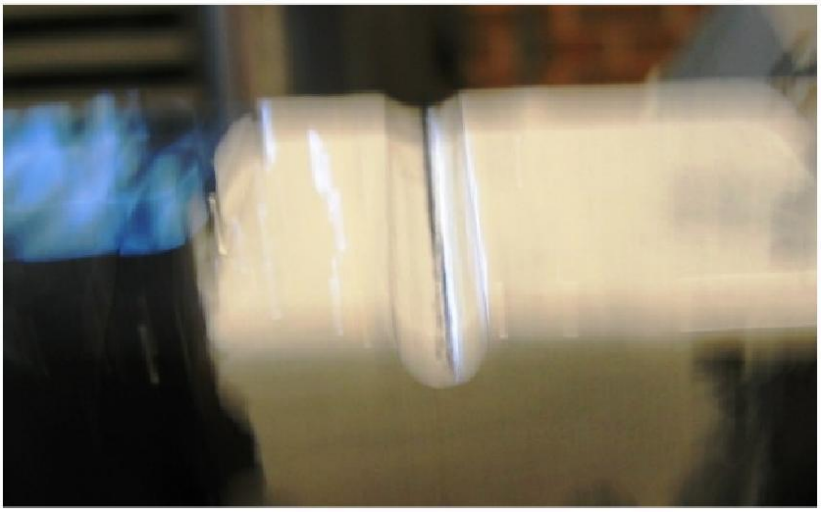

Figure 91. Notched sample with a crack across the width

By examining the image of the crack across the width, there appear to be two cracks spanning the width of the crack. It therefore seems reasonable to assume that the crack should be grown to the point that it spans half of the width of the part. In order to determine at what number of cycles this occurs, the FALPR program was used.

Fatigue crack growth constants, initial crack depth, initial crack a/c ratio, and the geometry of the cross-section were al input into FALPR. The software generated a plot of the growing crack, and

allowed for the number of cycles required for the crack to span half the cross-section to be read off the resulting crack growth chart. A sample of the FALPR output is shown in the figure below.

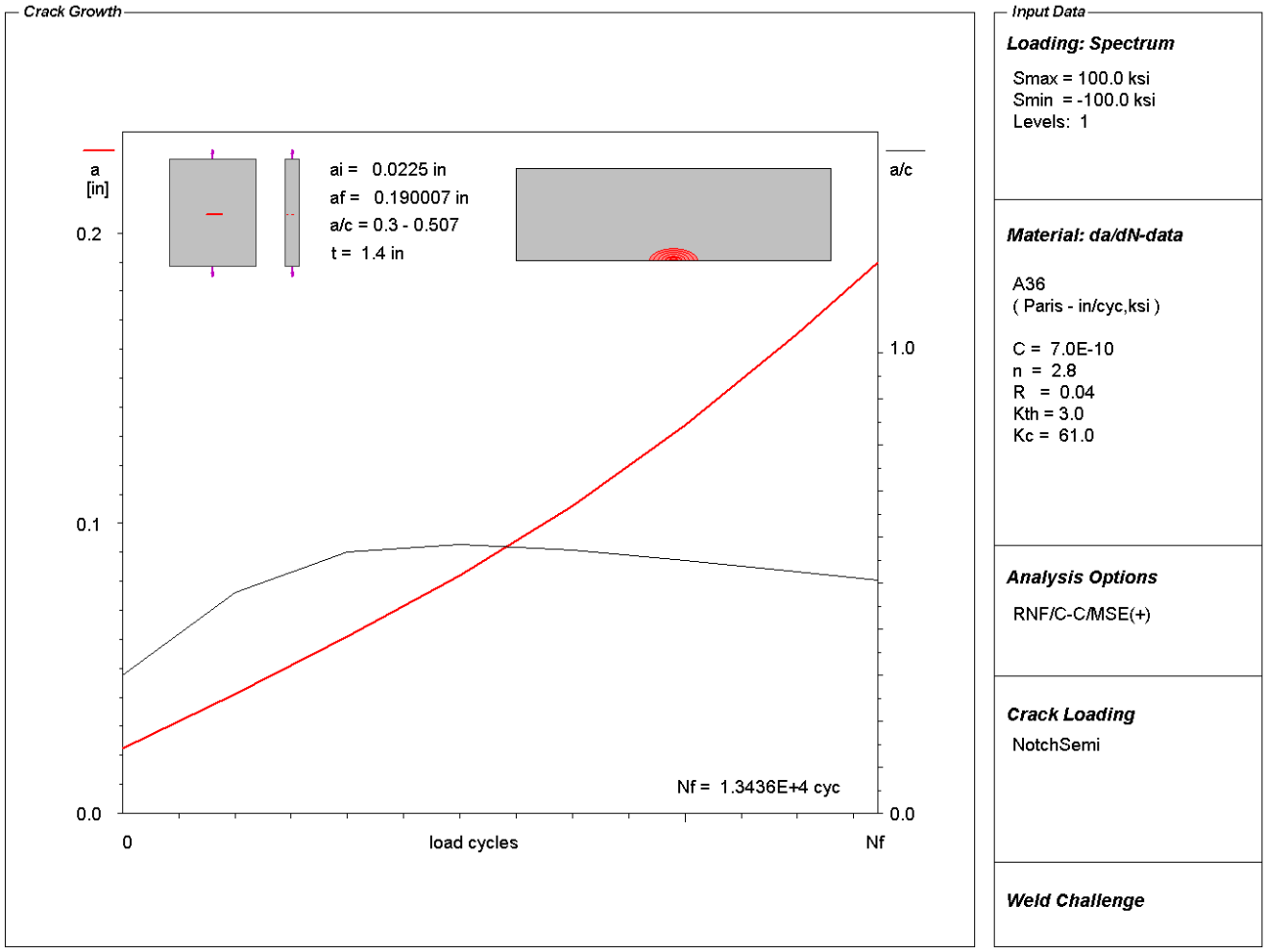

Figure 92. FALPR notched sample semi elliptical crack growth output.

The resulting final crack depth was found to be 0.19". The number of cycles required for this final crack depth to be reached is presented in the following table.

Table 8. Number of cycles required for crack to propagate across the thickness of a part for the notched sample.

Load Level	Cycles
High	10985
Medium	31118
Low	49183

At this point, there were two semi-elliptical cracks assumed to be generating the apparent crack across the width of the part. In order to grow the crack further, the pair of semi-elliptical cracks were

replaced with a single edge crack spanning the width of the part, with a depth equal to the maximum depth of the semi-elliptical cracks. This change is shown pictorially in the following figure.

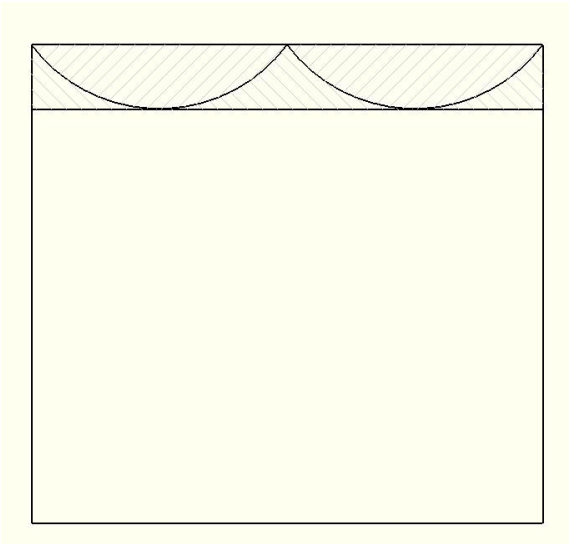

Figure 93. Replacement of the pair of semi-elliptical cracks with a single edge crack.

The edge crack was then grown to the depth of crack shown in state 3, the obvious edge crack. This state is shown in the following figure:

Figure 94. Notched sample with an obvious edge crack.

The depth of the crack was obtained by taking measurements of the image and scaling the value. The final crack depth was found to be 0.24”.

The Paris constants, material properties, and initial and final crack sizes were once again input into FALPR program. Please note that there was no value required for a/c for this trial, as the crack was

reset to be an edge crack. The number of cycles required to grow the crack from a crack across the width to an obvious edge crack is given in the following table:

Table 9. Number of cycles required to go from a crack across the width to an obvious edge crack in the notched sample.

Load Level	Cycles
High	743
Medium	1243
Low	3344

The final number of cycles to be determined is the number of cycles required to grow a crack from the obvious edge crack state to brittle fracture. For this stage, the FALPR program is run again, this time with the final crack size from the obvious edge crack state set as the initial crack size. The final crack size is the crack size that results in brittle fracture, and depends on the load applied. The number of cycles required to grow a crack from the obvious edge crack state to brittle fracture, as well as the final crack length, are given in the following table:

Table 10. Number of cycles required to go from an obvious edge crack to final failure in the notched sample.

Load Level	Cycles	Final Crack Length
High	1359	0.35”
Medium	3635	0.45”
Low	12696	0.62”

An image of the component after brittle fracture is shown below:

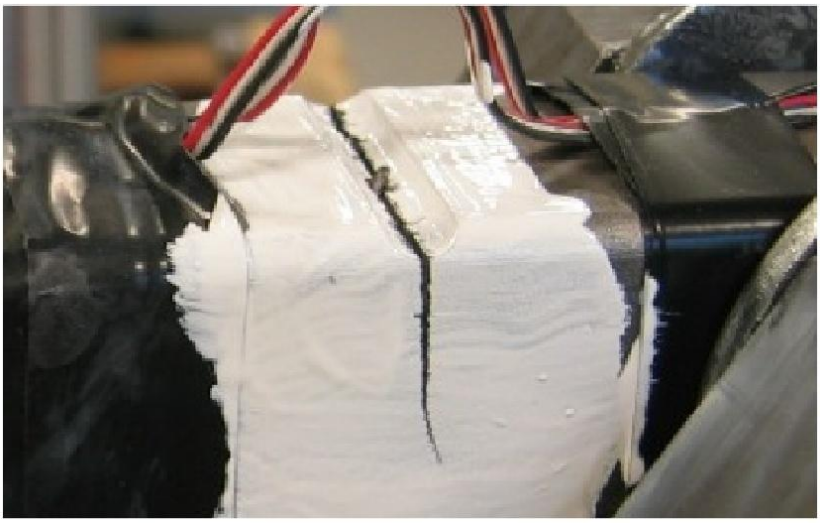

Figure 95. Failure in the notched sample.

5.4.4 Notched Specimen Total Predicted Lives

Now that the number of cycles associated with the crack initiation and growth phases have all been separately determined, the total lives to each stage may be found. The initiation life was taken to be the average of the initiation lives generated by the Neuber and ESED method. All of the following lives were determined by summing the total number of cycles required to reach the given stage. These total life values are summarized in the following table:

Table 11. Predicted lives for the notched sample.

	High Load Level	Medium Load Level	Low Load Level
Initiation	5043	12735	83457
Crack across the width of the part	16028	31118	132640
Obvious edge crack	16636	32135	135373
Failure	17747	35106	145751

5.4.5 Comparison of Total and Predicted Lives for the Notched Specimen

The total predicted number of cycles to failure for the notched sample was plotted against the experimental data obtained by the Fatigue Design and Evaluation committee. The data obtained by the committee is recorded in the following table:

Table 12. Experimental lives for the notched sample.

	High Load Level	Medium Load Level	Low Load Level
Initiation	N/A	5000	62000
Crack across the width of the part	N/A	8000	106000
Obvious edge crack	N/A	14000	115000
Failure	N/A	21975	154494

From the table, it can be seen that the predicted values for the fatigue life are generally longer than the experimental values. This discrepancy is considerably worse at the medium load level compared to the low load level.

The error is especially severe for the initiation and semi-elliptical crack growth regimes for the medium load level, where the part fails three to five times sooner than expected. The best match between the predicted and experimental data occurs for the prediction of life to brittle fracture in the low load level case, where the predicted value is only 6% less than the experimental life. A comparison of the results is included in Fig. 96.

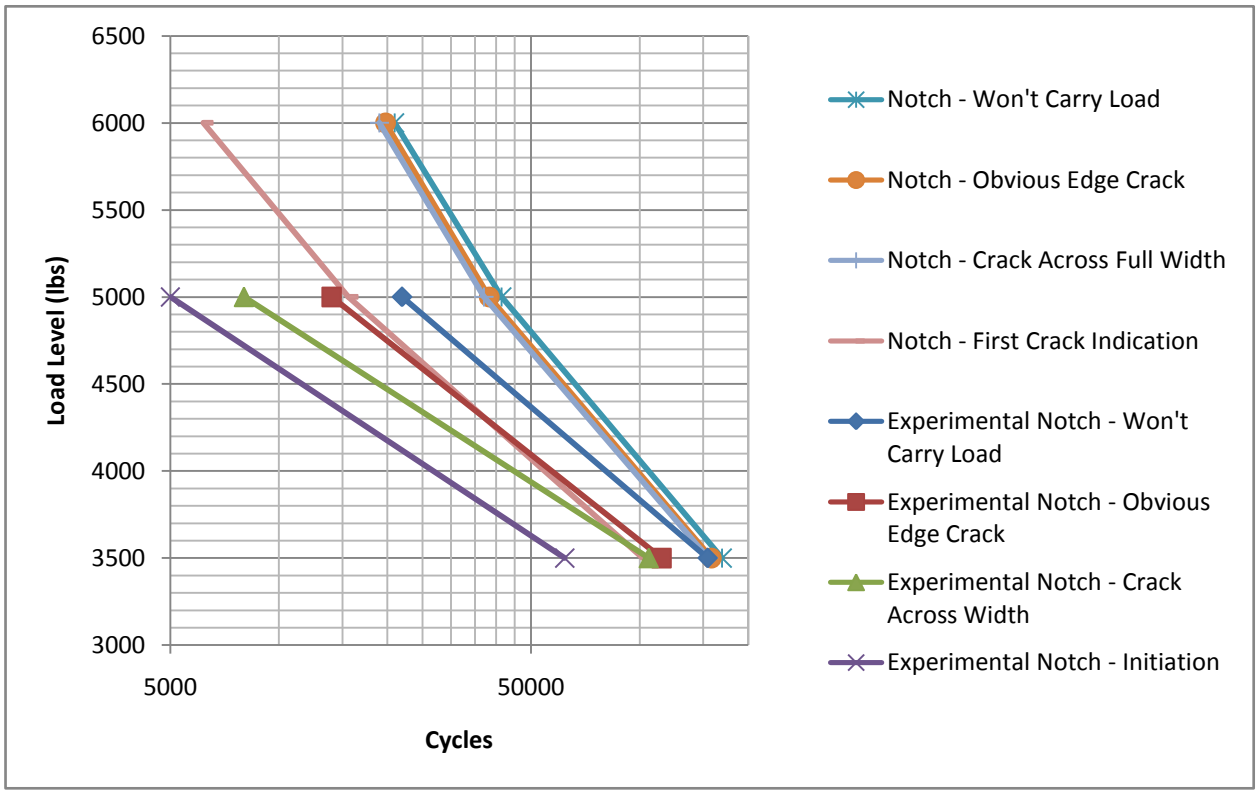

Figure 96. Comparison of experimental and predicted fatigue lives for the notched sample.

5.5 Welded Specimen Analysis

The welded sample was analyzed using a method similar to the one used on the notched sample. First, the fatigue life to crack initiation was found using the strain-life technique and the Manson-Coffin expression. Next, the sample was analyzed using the fatigue crack-growth method and the Paris equation.

5.5.1 Welded Specimen GR3 Analysis

The welded specimen was analyzed using the GR3 method in order to determine the peak stress and through-thickness stress distribution acting at the weld toe.

In order to simplify the analysis, the geometry was cut along the x and y lines of symmetry to generate a one-quarter model of the weld. This model is shown in the following figure:

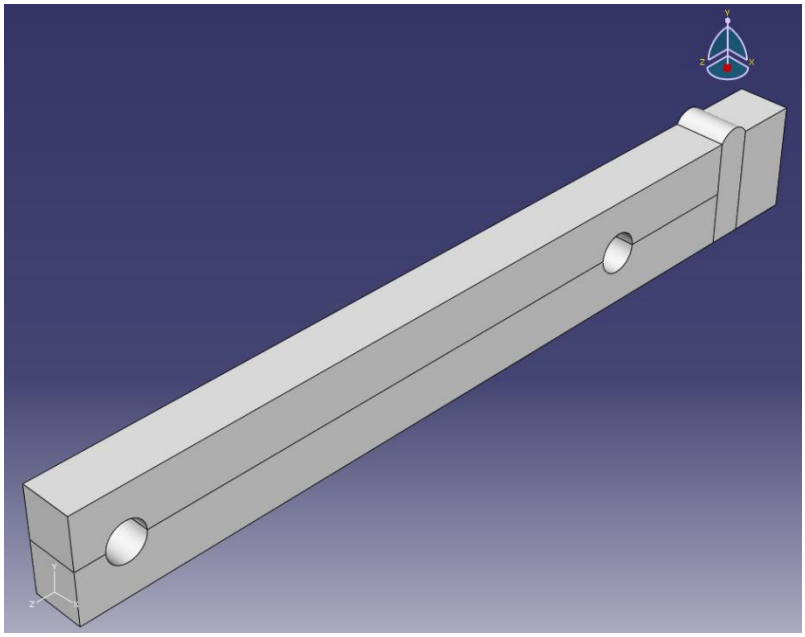

Figure 97. Quarter model of the welded specimen.

The quarter model then had x and z-symmetry boundary conditions applied to it along the cut surfaces. This is shown in the following figures:

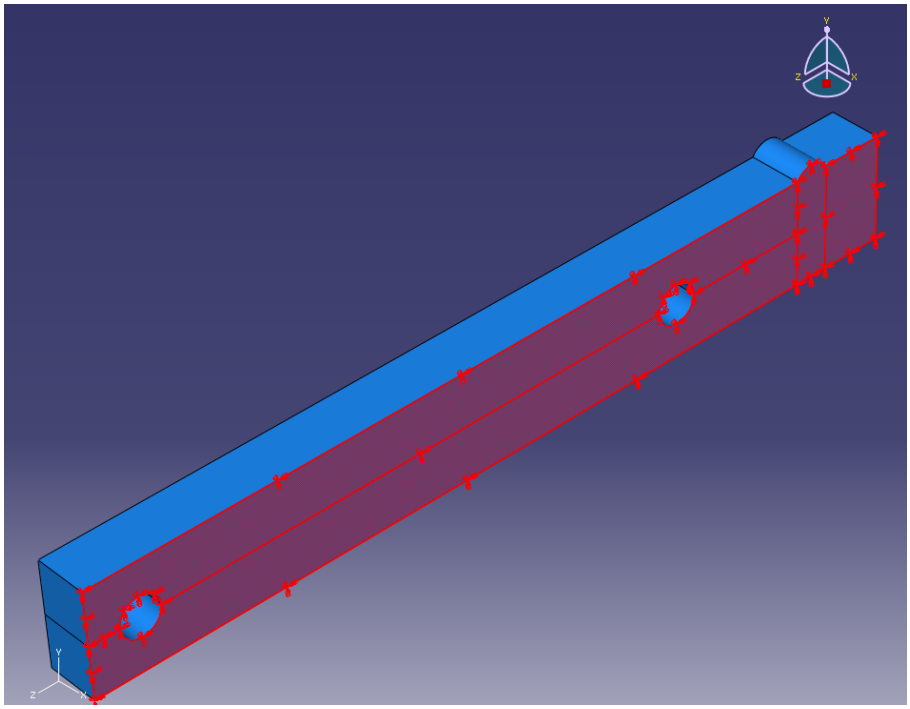

Figure 98. Region of application of the x-symmetry boundary condition.

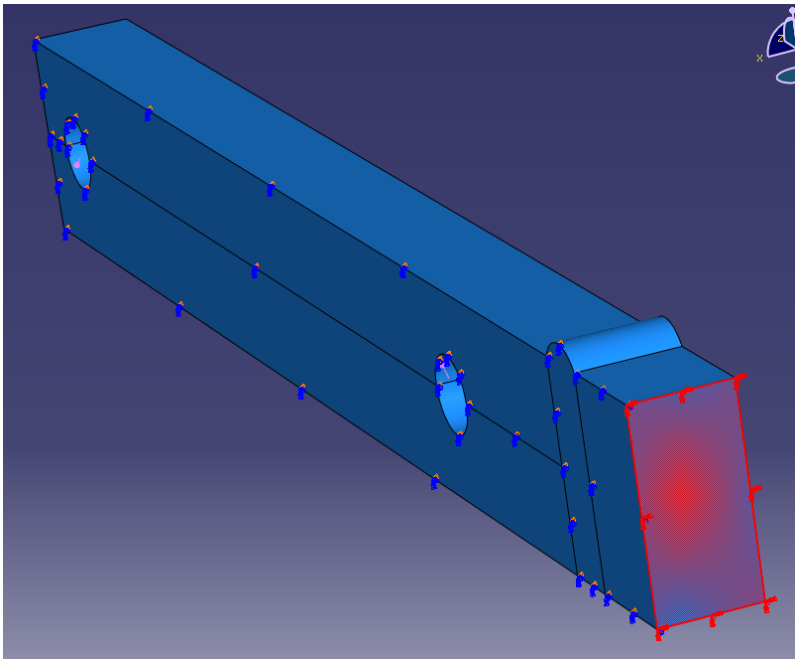

Figure 99. Region of application of the cantilever boundary condition.

Pressures were applied to the holes in the part to generate the required loads in the four-point bending specimens. The part is then meshed as shown in the following figure, with four elements through the thickness:

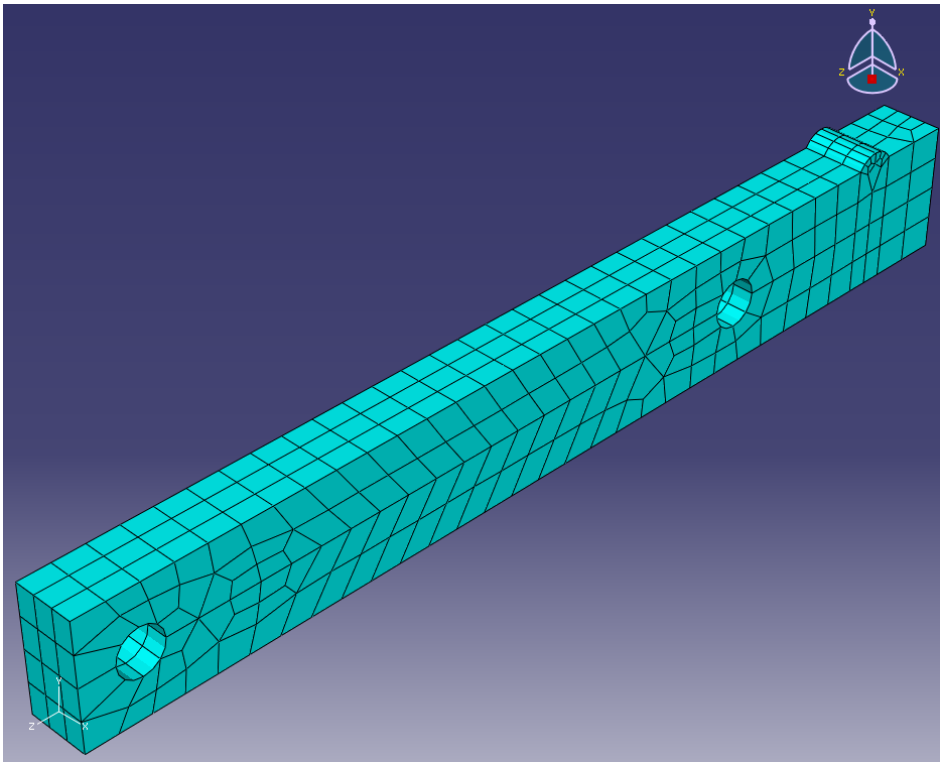

Figure 100. Coarsely-meshed welded model.

The coarsely-meshed model was then run in order to obtain the through-thickness stress distribution under the weld toe. Due to the three load levels used in this analysis, a distribution of the normalized through-thickness stress distribution will be provided. The field was normalized via the linearized surface stress value. The normalized coarse-mesh stress field is shown in the following figure:

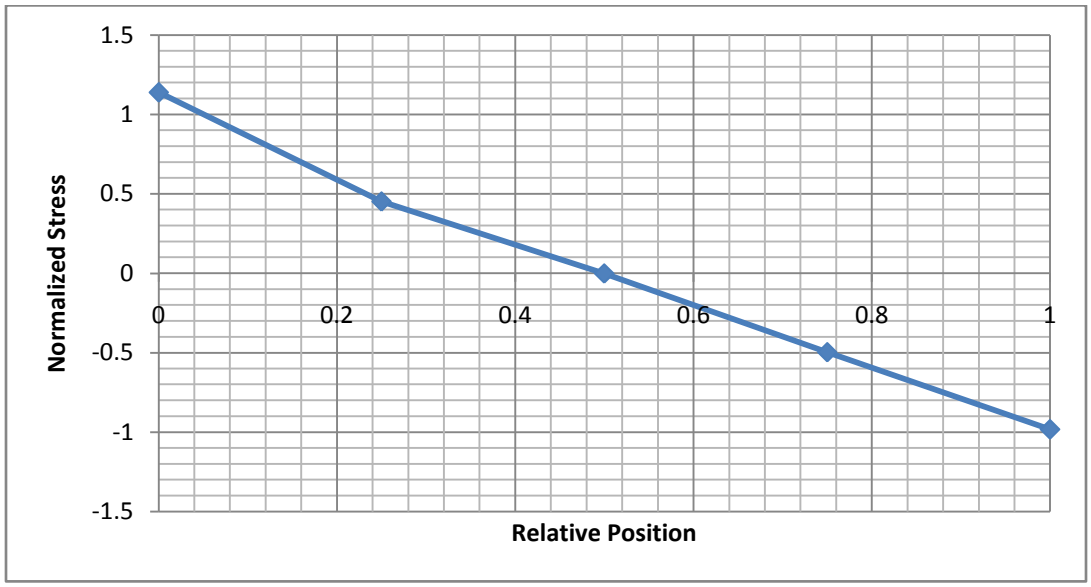

Figure 101. Coarse-mesh stress distribution of the welded specimen.

This distribution was compared with the high load level stress distribution predicted by a finely-meshed model of the same geometry, resulting in the following figure. The two distributions match up well over the inboard half of the cross-section.

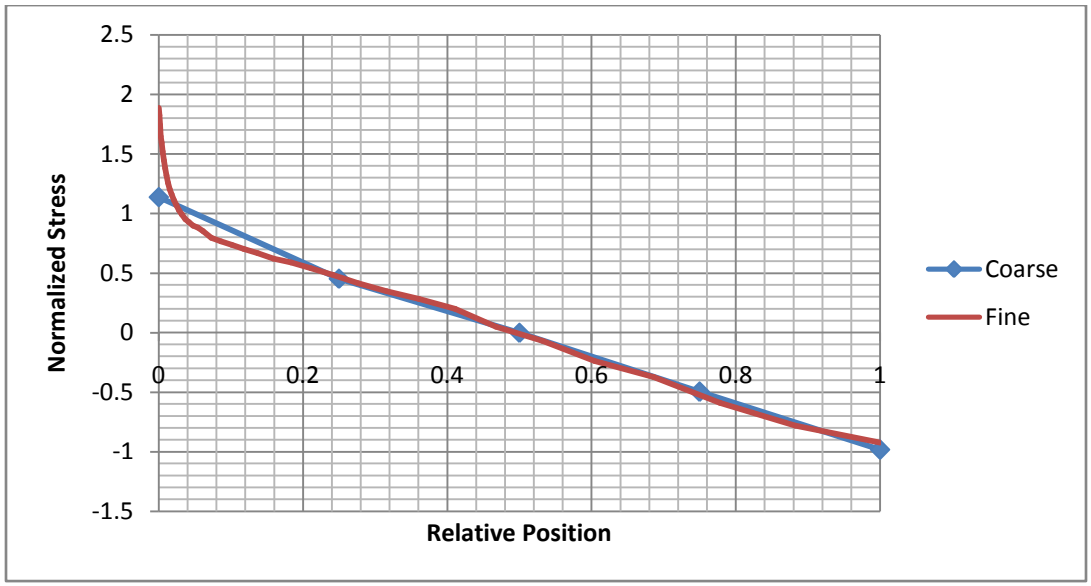

Figure 102. Comparison of coarse and fine finite element mesh distributions.

The stress values provided by the coarse mesh were input into Eq.59 to obtain the moment acting and Eq.63 to determine the axial load. These values were then input into Eq.49 and Eq.50 to obtain the nominal membrane and bending stresses. Eq.31, Eq.32, and Eq.33 were then used to determine the peak stress acting at the cross-section. Finally, the stress distribution in the cross-section under the weld toe was found using Eq.48. Eq.48 was used in lieu of Monahan's equation, Eq.47, because Monahan's equation only works reliably for fillet welds.

All three of the distributions are overlaid in the following figure:

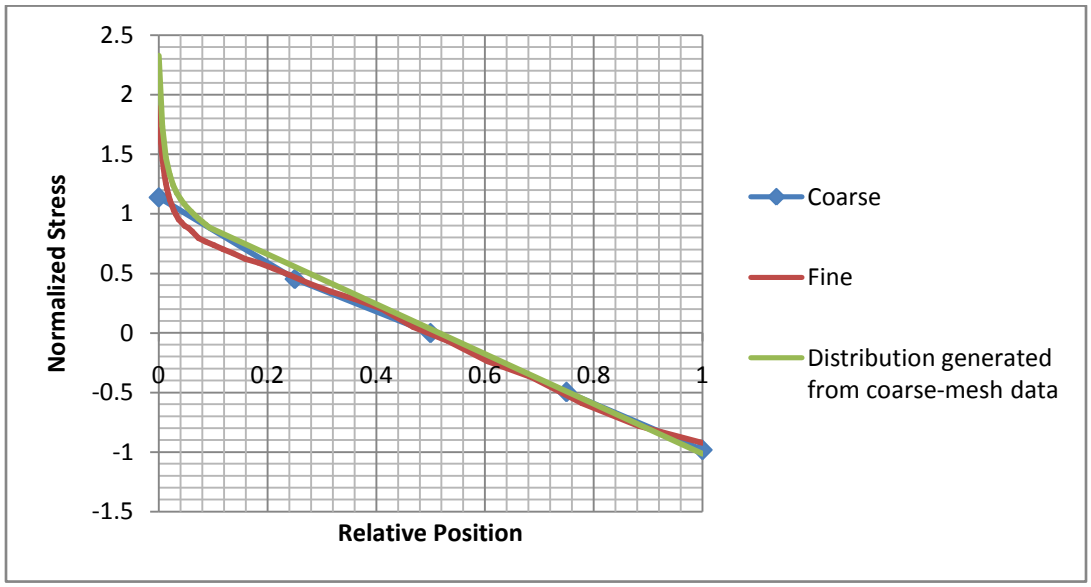

Figure 103. Comparison of coarse and fine finite element distributions, and the stress distribution generated using the coarse finite-element mesh data.

Note that the distribution generated using Eq.48 predicts slightly higher stresses than the fine-mesh, but this is mostly a result of the stress concentration equations suggested by Iida and Uemura (Eq.31, Eq.32, and Eq.33) over predicting the peak stress at the weld toe.

5.5.2 Welded Specimen Strain Life Analysis

The number of cycles required to initiate a crack in the welded specimen was determined using the strain-life method. The first step to performing the analysis is to determine the nominal stress acting in the critical cross-section. The nominal gross stress in the cross-section of the welded specimen was identical to the nominal gross stress in the notched specimen. The values are tabulated in Table 4.

The next step in obtaining the strain-life of the component would be to find the maximum local stress acting on the component. This requires that the stress concentration factor of the notch be found. This value was obtained by entering the notch geometry into the expression proposed by K.Iida and T. Uemura (Eq.33).

The equation returned a gross bending stress concentration factor $K_b = 2.33$, resulting in the following local maximum stresses at the notch tip. Local maximum stresses at the weld toe

Table 13. Maximum local elastic stresses at the weld toe.

Load Level	Maximum Local Stress
High	98.4 ksi
Medium	81.8 ksi
Low	57.6 ksi

Note that all of these maximum local stress values are greater than the yield stress of the material, 48 ksi. As a result of this, either Neuber's rule or the ESED method must be incorporated to relate the actual strains at the notch tip with the calculated elastic strains. The Neuber and ESED expressions are shown in equations 10 and 11.

The nominal stresses, gross stress concentration factor, and relevant material constants were at this point entered into the FALIN program, which computed the strain-life of the notched specimen for each of the load levels. Neuber's method was used to generate a lower bound on the life of the weldment for every given load level, and the ESED method with a bending correction was used to generate the upper bound, exactly as was done for the notched configuration.

At this point, however, an extra piece of data was added to the analysis. A residual stress equal to 60% of the yield stress of A36 steel was incorporated. This was done because the weldment was not stress relieved after the welding process.

The results of the FALIN fatigue-life calculations are summarized in the following table.

Table 14. Strain life estimates for the welded configuration.

Load Level	Cycles to Failure, Neuber	Cycles to Failure, ESED
High	1483	6412
Medium	5100	15900
Low	43260	98400

This result indicates the life of the notched component to crack initiation, and marks the conclusion of the first stage of the analysis for the notched component. The component will be analyzed further in the following section, which deals with fatigue crack growth.

5.5.3 Welded Specimen Fatigue Crack Growth Analysis

The fatigue crack growth analysis of the notched component was accomplished via use of the Paris equation. In order for the Paris equation to be used, however, the stress intensity factor must be found.

The stress intensity factor at any point in a cross-section, however, depends on the stress distribution over that cross-section. This relationship is given in Equation 12.

In order to proceed, the stress distribution in the cross-section, $\sigma_y(x)$, must be determined. The stress distribution was found by taking an expression proposed by Glinka, which describes the stress distribution near a notch tip. This near-notch stress distribution was merged with the nominal stress field at a distance of 3.5 weld toe radii from the surface.

Using Eq.48 and the nominal stress distribution, the following through-thickness stress distribution was derived for the welded component at the weld toe. It should be noted that while the notched component used a stress distribution over a 1.40625" thick net cross section, the stress distribution for the welded component used a stress distribution over the full 1.5" thickness of the weldment.

Given the stress distribution in the component, the Paris equation constants, and the R-ratio at which the constants were obtained, the fatigue crack growth problem now requires crack size inputs and the type of crack for the problem to be solved. In addition to this, however, the welded component also requires a residual stress distribution to be included.

The residual stress distribution used in this analysis was designed to generate 60% of yield stress close to the weld. This was accomplished using a triangular stress distribution, with 60% of yield stress acting at the surface and zero stress at a distance of 3.5 radii from the surface of the weldment. A triangular stress distribution was then applied over the remainder of the cross section to balance out the force generated by the near-weld stresses. The resulting stress distribution is shown in the following Fig.104.

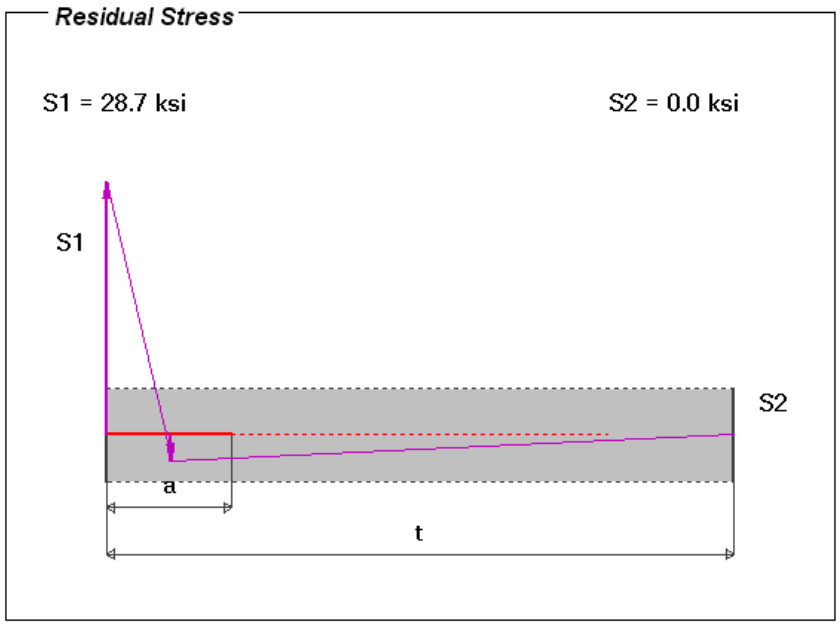

Figure 104. Residual stress distribution in the weld toe cross-section.

For the initial crack case, a semi-elliptical crack with an a/c value of 0.3 was assumed. It was decided to use the same values of initial and final crack size as were used for the notched component, 0.025” and 0.19”. This ensured that both samples would have experienced roughly the same amount of damage at each of the intervals. The image of the crack initiation and crack across the width for the welded component are shown in Fig. 105 and 106.

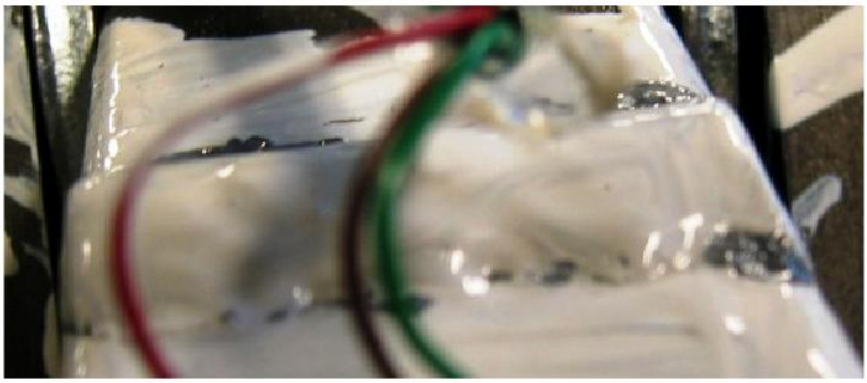

Figure 105. Initiation of cracking in the welded cross-section.

Figure 106. Crack across the width of the weldment.

It should be noted that, in the case of the welded component, it appears as if the several small initiation points had coalesced together into a crack spanning the width. This is quite distinct from the pair of initiations growing into a crack spanning the width that was observed in the notched component. However, in both cases, the crack is considered to be semi-elliptical until the point where the crack actually spanned the width of the weldment.

After inputting the relevant material properties, Paris equation constants, stress distributions, and final and initial crack sizes, the number of cycles required to grow the crack from initiation to a crack across the width was determined. The number of cycles required to go from crack initiation to a crack across the width of the weldment are recorded in table 13.

Table 15. Number of cycles required to go from crack initiation to a crack across the width of a part for the welded geometry.

High	12540
Medium	19120
Low	41280

From this point onwards, the crack was treated as an edge crack. This was done because it was assumed that the multiple initiating semi-elliptical cracks at the weld toe would coalesce and form a unified crack front. The edge crack across the width must then be grown until it reaches the obvious edge crack state. This state is shown in the following figure:

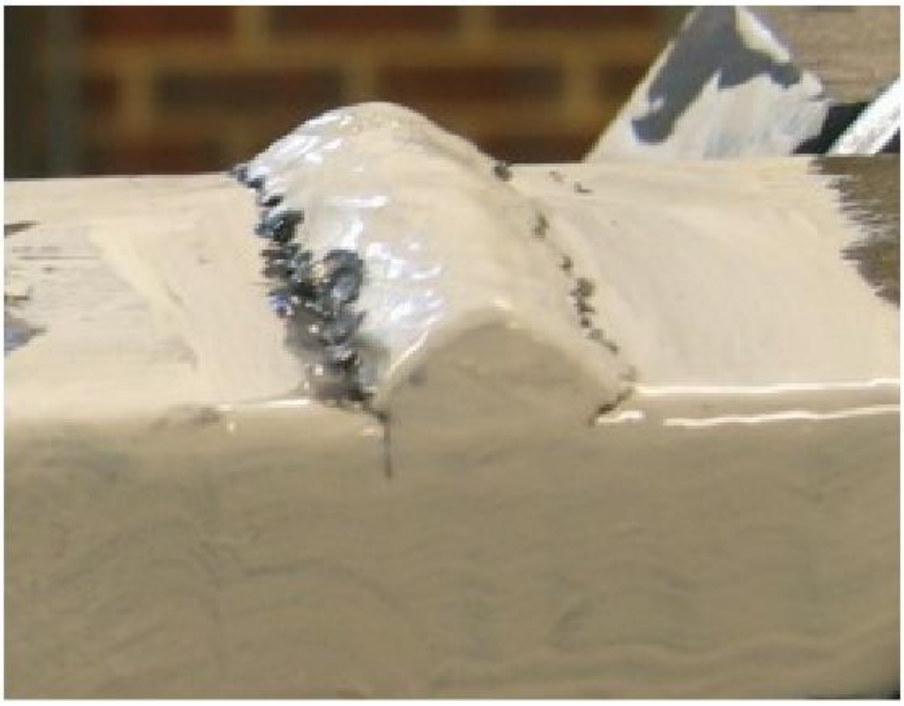

Figure 107. Obvious edge crack in the welded geometry.

In order to obtain comparable results for both the welded and notched components, the depth of obvious edge crack for the notched component was used for the welded component, 0.35”

The Paris constants, material properties, and initial and final crack sizes were once again input into FALPR program. Please note that there was no value required for a/c for this trial, as the crack was reset to be an edge crack. The number of cycles required to grow the crack from a crack across the width to an obvious edge crack is given in table 14:

Table 16. Number of cycles required to go from a crack across the width to an obvious edge crack in the welded configuration.

Load Level	Cycles
High	1900 (B.F. @ 0.33”)
Medium	2206
Low	6792

Please note that brittle failure was predicted to occur for the high load case at 1900 cycles, when the crack had reached a length of 0.33”.

The final number of cycles to be determined is the number of cycles required to grow a crack from the obvious edge crack state to brittle fracture. For this stage, the FALPR program is run again, this time with the final crack size from the obvious edge crack state set as the initial crack size. The final crack size is the crack size that results in brittle fracture, and depends on the load applied. The number

of cycles required to grow a crack from the obvious edge crack state to brittle fracture, as well as the final crack length, are given in the following table:

Table 17. Number of cycles required to go from an obvious edge crack to final failure in the welded geometry.

Load Level	Cycles	Final Crack Length
High	N/A	0.33”
Medium	2206	0.44”
Low	6792	0.63”

An image of the component after brittle fracture is shown below:

Figure 108. Final failure of the welded component.

5.5.4 Welded Specimen Total Predicted Lives

Now that the number of cycles associated with the crack initiation and growth phases have all been separately determined, the total lives to each stage may be found. The initiation life was taken to be the average of the initiation lives generated by the Neuber and ESED method. All of the following lives were determined by summing the total number of cycles required to reach the given stage. These total life values are summarized in the following table:

Table 18. Lives to failure for the welded specimen.

	High Load Level	Medium Load Level	Low Load Level
Initiation	9420	21920	140150
Crack across the width of the part	12154	25887	148514
Obvious edge crack	18226	35473	169801
Failure	18226	36529	175258

5.5.5 Comparison of Total and Predicted Lives for the Welded Specimen

The total predicted number of cycles to failure for the notched sample was plotted against the experimental data obtained by the Fatigue Design and Evaluation committee. The data obtained by the committee is recorded in the following table:

Table 19. Experimental lives to failure for the welded specimen.

	High Load Level	Medium Load Level	Low Load Level
Initiation	18000	55300	N/A
Crack across the width of the part	20700	94000	N/A
Obvious edge crack	23400	168000	N/A
Failure	30964	198282	N/A

From the table, it can be seen that the predicted values for the fatigue life are generally shorter than the experimental values. This discrepancy is considerably worse at the medium load level compared to the high load level.

The error is especially severe for the initiation and semi-elliptical crack growth regimes for the medium load level, where the weldment fails three to five times sooner than expected. The best match between the predicted and experimental data occurs for the prediction of life to brittle fracture in the high load level case. A comparison of the results is included in the following figure.

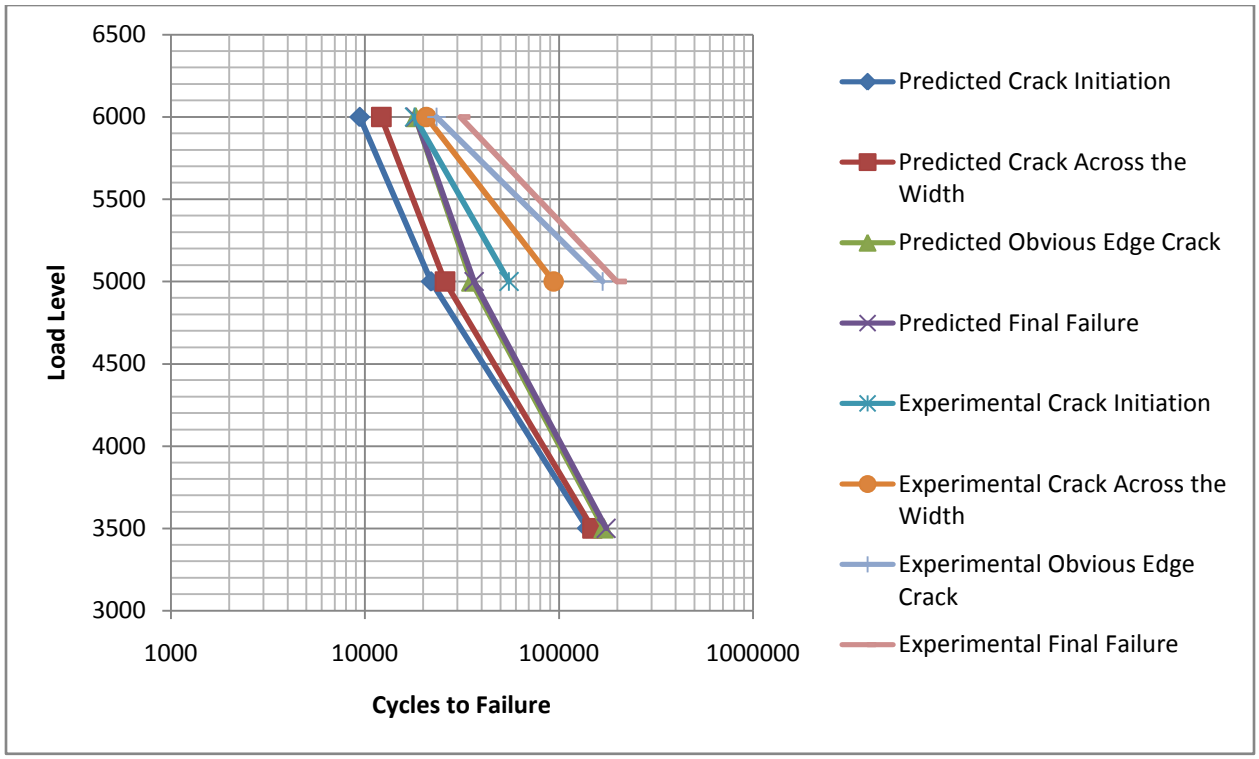

Figure 109. Comparison of experimental and predicted fatigue lives for the welded sample.

6.0 Conclusions

The GR3 modeling method can be used to generate good estimates for the peak stress and through-thickness stress distribution at the weld toe of a weldment using a course finite element mesh. The coarseness of the mesh allows for large, complicated structures to be modeled as a whole, all the while keeping the processing time for such a problem at a minimum.

The peak stress value generated using the GR3 method is useful for performing stress-life and strain-life analyses of a weldment. By coupling the GR3 method with Monahan's Equation or Glinka's Notch-Tip Stress Distribution, the through thickness stress distribution may be obtain and fatigue crack growth analyses may be performed.

Validations of the GR3 model are included for a circular tube on plate geometry subject to both tension and bending loads, and a t-joint geometry subjected to both in-plane and out-of-plane bending loads.

The applicability of the GR3 method to fatigue analyses was then demonstrated by using the GR3 method and Glinka's Notch-Tip Stress Distribution to generate through-thickness stress distributions for the Society of Automotive Engineers Fatigue Design and Evaluation committee challenge. The stress distributions generated using the GR3 method matched those generated using a fine finite-element mesh quite closely, and used a much coarser mesh.

Bibliography

[1] Albert, W.A.J., Uber Treibseile am Harz. *Archive fiir Mineralogie, Geognosie, Bergbau und Hiittenkunde* 10, 215-34, 1838.

[2] Wohler, A., Versuche Uber die festigkeit der Eisenbahnwagenachsen. *Zeitschrift fur Bauwesen* 10; English summary. *Engineering* 4, 160-1, 1867.

[3] Goodman, J., *Mechanics Applied to Engineering.* London: Longmans Green, 8th ed., 1914.

[4] Basquin, O.H., The Experimental Law of Endurance Tests, *Proc. ASTM,* Vol. 10, Part 11, 265-269, 1910.

[5] Griffith, A.A., The Phenomena of Rupture and Flow in Solids, *Philosophical Transactions of Royal Society, London,* Vol. A221, 163-97, 1920.

[6] Miner, M.A., Cumulative Damage in Fatigue, *Trans. ASME, J. Appl. Mech.,* Vol. 67, A159-64, 1945.

[7] Manson, S.S., Hirschberg, M.H., Fatigue behavior in strain cycling in low- and intermediate cycle range, *Sagamore Army Matls Research Conference*, 133-178, 1963.

[8] Topper, T. H., Sandor, B. I., Morrow, J., Cumulative Fatigue Damage Under Cyclic Strain Control, *J. Materials,* Vol. 4, No. 1, 189-9, 1969.

[9]Matsuishi, M., Endo, T., Fatigue of Metals Subjected to Varying Stress, Presented to Japan Society of Mechanical Engineers, Fukuoka, Japan, March 1968.

[10]Irwin, G.R., Analysis of Stresses and Strains Near the End of a Crack Traversing a Plate, *Journal of Applied Mechanics* Vol. 24, 361-4, 1957.

[11]Paris, P.C., *The Growth of crack Due to Variations in Loads*. Ph.D. Thesis. Bethlehem: Lehigh University, 1960.

[12] Fricke, W., Recommended hot spot analysis procedure for structural details of ships and FPSOs based on round-robin FE Analyses. *Int J of Offshore and Polar Engineering,* Vol. 12, No. 1, 40–7, 2002.

[13] Niemi, E., Tanskanen, P., Hot spot stress determination for welded edge gussets. *Welding in the World*, Vol. 44, No. 5, 31–7, 2000.

[14] Neuber, H., Theory of Stress Concentration for Shear-Strained Prismatic Bodies with Arbitrary Nonlinear Stress-Strain Laws, *Trans. ASME, J. Appl. Mech.*, Vol. 28, 544-50, 1961.

[15] Glinka, G., Fractures Mechanics Lecture Notes, *University of Waterloo*, 2008.

[16] Kurihara, M., Katoh, A., Kwaahara, M., Analysis on Fatigue Crack Growth Rates Under a Wide Range of Stress Ratio, *Journal of Pressure Vessel Technology, Transactions of the ASME*, Vol. 108, no. 2, 209-213, May 1986.

[17] Glinka, G., Shen, G., Universal features of weight functions for cracks in mode I, *Engineering Fracture Mechanic*, Vol. 40, no. 6, 1135-1146, 1991.

[18] Glinka, G., Shen, G., Weight functions for a surface semi-elliptical crack in a finite thickness plate, *Theoretical and Applied Fracture Mechanics*, Vol. 15, no. 3, 247-255, 1991.

[19] Marshall, P.W., Design of welded tubular connections, *Elsevier*, Amsterdam, 1992.

[20] Niemi, E., Recommendations concerning stress determination for fatigue analysis of welded components, *International Institute of Welding*. XIII-1458-92/XV-797-92, 1995.

[21] Malik, S.M., Fatigue life assessment of welded joints based on the decomposition of the structural hot spot stress, University of Waterloo, Waterloo, 2006.

[22] Monahan, C.C., *Early Fatigue Cracks Growth at Welds*, Computational Mechanics Publications, Southampton UK, 1995.

[23] Iida, K., Uemura, T., Stress Concentration Factor Formulas Widely Used in Japan, *Fatigue and Fracture of Engineering Materials & Structures*, Vol. 19, no. 6, 779-786, 1996.

[24] Goyal, R. Coarse 3D mesh FE procedure for stress and fatigue analysis of weldments, *Presentation at the University of Waterloo on February 14th*, John Deere, 2009.

[25] Cordes, T., Lingenfelser, D. Total Fatigue Life = Crack Initiation +Crack Propagation: Next Focused Effort?, *SAE FD&E Committee*, 2008.